**Universidade de Aveiro** Departamento de
**2014** Electrónica, Telecomunicações e Informática

**Zhansheng Liu**

# Caracterização de Moduladores RSOA em Ligações de Rádio Sobre Fibra

# Characterization of RSOA Modulators in Radio over Fiber Links

**Universidade de Aveiro** Departamento de
**2014** Electrónica, Telecomunicações e Informática

**Zhansheng Liu**

# Caracterização de Moduladores RSOA em Ligações de Rádio Sobre Fibra

# Characterization of RSOA Modulators in Radio over Fiber Links

Tese apresentada à Universidade de Aveiro para cumprimento dos requesitos necessários à obtenção do grau de Doutor em Engenharia Electrotécnica, realizada sob a orientação científica do Doutor Manuel Alberto Reis de Oliveira Violas, Professor Auxiliar, e co-orientação científica do Doutor Nuno Miguel Gonçalves Borges de Carvalho, Professor Catedrático, do Departamento de Electrónica, Telecomunicações e Informática da Universidade de Aveiro.

Apoio financeiro da Fundação para a Ciência e a Tecnologia – FCT através da bolsa SFRH / BD / 68376 / 2010 e do FSE no âmbito do Programa Operacional Potencial Humano (POPH) do QREN.

**o júri / the jury**

presidente / president

**Prof. Doutor Paulo Jorge de Melo Matias Faria de Vila Real**
Professor Catedrático do Departamento de Engenharia Civil da Universidade de Aveiro

vogais / examiners committee

**Prof. Doutor Henrique José Almeida Silva**
Professor Associado do Departamento de Engenharia Electrotécnica e de Computadores da Faculdade Ciências e Tecnologia da Universidade de Coimbra

**Prof. Doutor Henrique Manuel de Castro Faria Salgado**
Professor Associado do Departamento de Engenharia Eletrotécnica e de Computadores da Faculdade de Engenharia da Universidade do Porto

**Prof. Doutor Paulo Sérgio de Brito André**
Professor Associado do Departamento de Engenharia Electrotécnica e de Computadores, Instituto Superior Tecnico da Universidade de Lisboa

**Prof. Doutor Pedro Miguel da Silva Cabral**
Professor Auxiliar do Departamento Electrónica Telecomunicações e Informática da Universidade de Aveiro

**Prof. Doutor Manuel Alberto Reis de Oliveira Violas**
Professor Auxiliar do Departamento Electrónica Telecomunicações e Informática da Universidade de Aveiro (Orientador)

**agradecimentos / acknowledgments**

First and foremost, I would like to express my deepest gratitude and appreciation to my advisor Professor Dr. Manuel Alberto Violas for giving me an opportunity to work on this challenging topic and for providing support and guidance throughout my PhD research. My deepest gratitude also goes to my co-advisor Professor Dr. Nuno Borges Carvalho for his insightful discussions and suggestions. This work would never have been completed without them.

I would also like to thank Dr. Guilhem de Valicourt and Dr. Romain Brenot for their designing a novel RSOA device.

Moreover, I also need to thank my colleagues Mostardinha and Prata for their support in both optical and RF labs.

I also gratefully acknowledge financial assistance from PHOTON project and Fundação para a Ciência e a Tecnologia during my study.

Finally, I would like to thank my parents, Zhenjiang and Sumin, for their unconditional love, guidance and support. Next I would like to thank my wife, Yanfang, for her encouragement, support, patience and unwavering love. I would like to express my thanks to my daughter, Jiayang, for being a good girl and giving me unlimited happiness and pleasure.

**Palavras-chave**

Comunicações ópticas, rádio sobre fibra, amplificador óptico semicondutor reflectivo, não-linearidade, distorção, linearização, multiplexação por sub-portadora, modelagem.

**Resumo**

Nesta tese são propostos modelos físicos e comportamentais para o amplificador óptico semicondutor reflectivo (RSOA), tendo como objectivo a avaliação do seu desempenho quando utilizado como modulador em ligações de rádio sobre fibra (RoF). Os modelos propostos são capazes de prever o comportamento do dispositivo quando utilizado com sinais de banda larga bem como quando estimulado por sinais de elevada potência.

Inicialmente propõe-se um modelo físico simplificado para o RSOA baseado nas equações de taxa e nas equações de propagação electromagnética. A implementação do modelo utiliza o ADS (Advanced Design Systems) e o bloco designado por dispositivo definido simbolicamente (SDD) para descrever as equações de taxa, assim como a propagação de fotões ao longo da cavidade. O modelo permite uma análise detalhada do ganho óptico, distorções harmônicas, intermodulação e seu desempenho de transmissão com portadoras RF modeladas.

Foram também considerados modelos comportamentais. Um modelo baseado em rede neural artificial (ANN) e um modelo polinomial generalizado para banda base foram considerados tendo os parâmetros respectivos sido extraídos utilizando, para o efeito, dados obtidos experimentalmente. São demonstradas a característica da distorção resultante da conversão amplitude - amplitude (AM-AM) e conversão da fase - amplitude (AM-PM) no modulador RSOA. Um modelo baseado em parametros X, obtidos a partir do modelo físico, foi também analisado.

Compensação da não-linearidade do modulador RSOA é realizada com base num modelo polinomial com memória. Demonstra-se que a distorção não linear do modulador RSOA pode ser compensada com sucesso. Com a compensação obtem-se uma redução de 17 dB da distorção introduzida pelos produtos de intermodulação de terceira ordem. O EVM (Error Vector Magnitude) apresenta uma melhoria de 6,1% para 2,0%.

Na última parte deste trabalho considera-se uma configuração que representa a ligação ascendente por fibra de um sistema de antenas remoto a uma estação central de processamento. Com esta configuração pretende-se demonstrar a possibilidade de implementação de uma tecnologia MIMO, suportada num sistema RoF. Baseado numa técnica de multiplexação subportadora (SCM), os sinais de quatro canais com largura de banda de 100 MHz por canal são multiplexados e utilizados para modelar o ganho do RSOA. O desempenho deste link óptico é caracterizado para modulações OFDM considerando diferentes números de sub-portadoras por símbolo (64, 512 , 1024 e 2048) assim como o formato QAM imposto sobre cada sub-portadora.

**Keywords**

Optical communications, radio over fiber, reflective semiconductor optical amplifier, nonlinearity, distortion, linearization, subcarrier multiplexing, modeling.

**Abstract**

In this work physical and behavioral models for a bulk Reflective Semiconductor Optical Amplifier (RSOA) modulator in Radio over Fiber (RoF) links are proposed. The transmission performance of the RSOA modulator is predicted under broadband signal drive.

At first, the simplified physical model for the RSOA modulator in RoF links is proposed, which is based on the rate equation and traveling-wave equations with several assumptions. The model is implemented with the Symbolically Defined Devices (SDD) in Advanced Design System (ADS) and validated with experimental results. Detailed analysis regarding optical gain, harmonic and intermodulation distortions, and transmission performance is performed. The distribution of the carrier and Amplified Spontaneous Emission (ASE) is also demonstrated.

Behavioral modeling of the RSOA modulator is to enable us to investigate the nonlinear distortion of the RSOA modulator from another perspective in system level. The Amplitude-to-Amplitude Conversion (AM-AM) and Amplitude-to-Phase Conversion (AM-PM) distortions of the RSOA modulator are demonstrated based on an Artificial Neural Network (ANN) and a generalized polynomial model. Another behavioral model based on X-parameters was obtained from the physical model.

Compensation of the nonlinearity of the RSOA modulator is carried out based on a memory polynomial model. The nonlinear distortion of the RSOA modulator is reduced successfully. The improvement of the 3rd order intermodulation distortion is up to 17 dB. The Error Vector Magnitude (EVM) is improved from 6.1% to 2.0%.

In the last part of this work, the performance of Fibre Optic Networks for Distributed and Extendible Heterogeneous Radio Architectures and Service Provisioning (FUTON) systems, which is the four-channel virtual Multiple Input Multiple Output (MIMO), is predicted by using the developed physical model. Based on Subcarrier Multiplexing (SCM) techniques, four-channel signals with 100 MHz bandwidth per channel are generated and used to drive the RSOA modulator. The transmission performance of the RSOA modulator under the broadband multi channels is depicted with the figure of merit, EVM under different Quadrature Amplitude Modulation (QAM) level of 64 and 254 for various number of Orthogonal Frequency Division Multiplexing (OFDM) subcarriers of 64, 512, 1024 and 2048.

# Contents

**Contents** i

**List of Abbreviations** iii

**List of Figures** vii

**List of Tables** xi

**1 Introduction** 1
- 1.1 RoF Links 1
- 1.2 Distributed Antenna System (DAS) 3
- 1.3 Reflective Semiconductor Optical Amplifier 4
- 1.4 Motivation and Objectives 4
- 1.5 Thesis Overview 8
- 1.6 Research Contribution 9

**2 Physical Modeling and Simulation of RSOA** 11
- 2.1 Introduction 11
- 2.2 Physical Modeling 12
  - 2.2.1 Rate Equation 12
  - 2.2.2 Traveling-Wave Equations for Optical Signal 14
  - 2.2.3 Traveling-Wave Equations for ASE 15
  - 2.2.4 Model Implementation 16
  - 2.2.5 Parameter Extraction 17
- 2.3 Results and Discussion 19
  - 2.3.1 Static Characteristics 19
  - 2.3.2 Nonlinearity 20
  - 2.3.3 Transmission Performance 22
- 2.4 Distribution of Carrier Density and Photon Density 26
- 2.5 Link Gain Improvement 27
- 2.6 Summary 29

**3 Behavioral Modeling and Simulation of RSOA** 31
- 3.1 Introduction 31
  - 3.1.1 Parameter Extraction Procedure 32
  - 3.1.2 Experimental Setup 33
  - 3.1.3 Time Alignment and Compensation 34

3.1.4 Model Accuracy Evaluation . . . . . 35
3.2 Tapped-Delay Multilayer Perceptron (TDMLP) . . . . . 36
3.2.1 TDMLP Model . . . . . 36
3.2.2 Overfitting . . . . . 37
3.2.3 Activation Function . . . . . 38
3.2.4 Back Propagation Learning Algorithm (BPLA) . . . . . 38
3.2.5 TDMLP Training . . . . . 39
3.2.6 TDMLP Validation . . . . . 40
3.3 Generalized Memory Polynomial (GMP) . . . . . 45
3.3.1 GMP Based Modeling . . . . . 45
3.3.2 Extraction Methodology . . . . . 45
3.3.3 Validation and Results . . . . . 48
3.4 X-parameters . . . . . 51
3.4.1 Polyharmonic Distortion (PHD) Model and X-parameters . . . . . 51
3.4.2 Extraction Procedure and Simulation Configures of X-parameters . . . . . 54
3.5 Summary . . . . . 56

**4 Nonlinear Distortions and Compensation** **61**
4.1 Introduction . . . . . 61
4.2 Distortion Compensation Techniques . . . . . 62
4.2.1 Optical Distortion Compensation . . . . . 62
4.2.2 Electrical Distortion Compensation . . . . . 62
4.3 GMP Predistorter . . . . . 64
4.4 Results and Discussion . . . . . 67
4.5 Summary . . . . . 68

**5 Transmission Performance of Multi-Channel Systems** **71**
5.1 Introduction . . . . . 71
5.2 Overview of FUTON Project . . . . . 72
5.3 Optical Subcarrier Multiplexing . . . . . 73
5.4 Predicted Performance of the Multi-Channel System . . . . . 75
5.5 Experimental Demonstration of Four Channels . . . . . 79
5.6 Summary . . . . . 83

**6 Conclusions & Future Work** **85**
6.1 Conclusions . . . . . 85
6.2 Future Work . . . . . 86

**References** **87**

# List of Abbreviations

| | | |
|---|---|---|
| **3G** | Third Generation | 71 |
| **3GPP** | Third Generation Partnership Project | 3 |
| **4G** | Fourth Generation | 71 |
| **64QAM** | 64-ary Quadrature Amplitude Modulation | 24 |
| **ADS** | Advanced Design System | 8 |
| **AM-AM** | Amplitude-to-Amplitude Conversion | 8 |
| **AM-PM** | Amplitude-to-Phase Conversion | 8 |
| **AMP** | Amplifier | 19 |
| **ANN** | Artificial Neural Network | 6 |
| **AR** | Anti reflective | 4 |
| **ASE** | Amplified Spontaneous Emission | 11 |
| **BPLA** | Back Propagation Learning Algorithm | 38 |
| **CU** | Central Unit | 1 |
| **CW** | Continuous Wave | 12 |
| **DAC** | Data Access Component | 17 |
| **DAS** | Distributed Antenna System | 3 |
| **DBWS** | Distributed Broadband Wireless System | 72 |
| **DC** | Direct Current | 17 |
| **DFB** | Distributed Feedback | 7 |
| **DL** | Downlink | 73 |
| **DML** | Directly Modulated Laser | 2 |
| **DPD** | Digital Predistortion | 8 |
| **DUT** | Device Under Test | 19 |
| **DWDM** | Dense Wavelength Division Multiplexing | 2 |
| **EDFA** | Erbium-Doped Fiber Amplifier | 6 |
| **E/O** | Electrical-to-Optical Conversion | 1 |
| **EVM** | Error Vector Magnitude | 22 |
| **FP7** | Seventh Framework Programme | 72 |

| | | |
|---|---|---|
| **FPGA** | Field Programmable Gate Arrays | 86 |
| **FWM** | Four-Wave Mixing | 7 |
| **FUTON** | Fibre Optic Networks for Distributed and Extendible Heterogeneous Radio Architectures and Service Provisioning | 4 |
| **GMP** | Generalized Memory Polynomial | 8 |
| **GPIB** | General Purpose Interface Bus | 34 |
| **HB** | Harmonic Balance | 16 |
| **HR** | High Reflective | 4 |
| **IF** | Intermediate Frequency | 8 |
| **IFFT** | Inverse Fast Fourier Transform | 77 |
| **IMD** | Intermodulation Distortion | 22 |
| **IMD3** | 3rd-Order IMD | 21 |
| **IMDD** | Intensity-Modulation Direct-Detection | 1 |
| **IIP3** | Input 3rd-Order Intercept Point | 21 |
| **IP** | Intellectual Property | 55 |
| **LM** | Levenberg-Marquardt | 38 |
| **LS** | Least Square | 45 |
| **LTE** | Long Term Evolution | 3 |
| **MLP** | Multilayer Perceptron | 36 |
| **MIMO** | Multiple Input Multiple Output | 4 |
| **MZM** | Mach-Zehnder Modulator | 2 |
| **NMSE** | Normalized Mean Square Error | 35 |
| **NVNA** | Nonlinear Vector Network Analyzer | 32 |
| **O/E** | Optical-to-Electrical Conversion | 1 |
| **OFDM** | Orthogonal Frequency Division Multiplexing | 24 |
| **P1dB** | 1 dB Compression Point | 21 |
| **PAPR** | Peak-to-Average Power Ratio | 39 |
| **PD** | Photodetector | 19 |
| **PHD** | Polyharmonic Distortion | 32 |
| **PSD** | Power Spectral Density | 40 |
| **QAM** | Quadrature Amplitude Modulation | 1 |
| **QD-SOA** | Quantum-Dot SOA | 6 |
| **RAU** | Remote Access Unit | 1 |
| **RF** | Radio Frequency | 1 |
| **RMS** | Root Mean Square | 24 |
| **RoF** | Radio over Fiber | 1 |

| | | |
|---|---|---|
| **RSOA** | Reflective Semiconductor Optical Amplifier | 1 |
| **SCM** | Subcarrier Multiplexing | 1 |
| **SDM** | Space Division Multiplexing | 73 |
| **SDD** | Symbolically Defined Devices | 8 |
| **SFDR** | Spurious Free Dynamic Range | 21 |
| **SOA** | Semiconductor Optical Amplifier | 1 |
| **SRRC** | Square Root Raised Cosine | 39 |
| **TDMLP** | Tapped-Delay Multilayer Perceptron | 8 |
| **UL** | Uplink | 73 |
| **VPI** | Virtual Photonics Inc. (simulation software manufacturer) | 76 |
| **VSA** | Vector Signal Analyzer | 19 |
| **VSG** | Vector Signal Generator | 19 |
| **WDM** | Wavelength Division Multiplexing | 1 |
| **WLAN** | Wireless Local Area Network | 24 |

*This page is intentionally left blank.*

# List of Figures

1.1 A general RoF link using a simple IMDD scheme. main components include E/O conversion, optical fiber and O/E conversion. . . . . . . . . . . . . . . . . . . . . . . . 2
1.2 Schematic of radio over fiber links [1]. . . . . . . . . . . . . . . . . . . . . . . . . . . 3
1.3 RSOA spectrum with low optical confinement. . . . . . . . . . . . . . . . . . . . . . 5

2.1 RSOA elementary section for numerical modeling. (a) multi-section schematic, (b) implementation using a SDD built-in component in ADS. . . . . . . . . . . . . . . . . 16
2.2 Optical power versus bias currents for 3, 4, 6, 12 and 14 sections. . . . . . . . . . . 17
2.3 Simulation layout for the multi-section based RSOA model. . . . . . . . . . . . . . . 18
2.4 Experimental test bench . . . . . . . . . . . . . . . . . . . . . . . . . . . . . . . . . 20
2.5 Measured and simulated optical powers versus bias currents. . . . . . . . . . . . . . 21
2.6 Measured and simulated optical gain as a function of optical input power under the different biases of 60 mA, 90 mA, and 120 mA . . . . . . . . . . . . . . . . . . . . . 22
2.7 Measured and modeled fundamental and harmonic distortions under one-tone test with frequency of 1 GHz. . . . . . . . . . . . . . . . . . . . . . . . . . . . . . . . . 23
2.8 Measured and simulated fundamental and IMD3 distortions under two-tone test with frequencies of 995 MHz and 1005 MHz. . . . . . . . . . . . . . . . . . . . . . . . . . 23
2.9 Illustration of EVM. . . . . . . . . . . . . . . . . . . . . . . . . . . . . . . . . . . . 24
2.10 Simulation diagram of the transmission performance by using ADS. . . . . . . . . . 25
2.11 Measured and simulated EVMs versus RF input powers under the different optical inputs (a) at -5 dBm, (b) at -10 dBm, (c) at -15 dBm. . . . . . . . . . . . . . . . . . . 26
2.12 Spatial distribution of carrier density, signal photon density and ASE photon density as a function of position along the length of the active region at the input optical powers of -50 dBm (left)and 0 dBm (right). The bias currents range from 20 mA to 100 mA. . . . . . . . . . . . . . . . . . . . . . . . . . . . . . . . . . . . . . . . . 28
2.13 Schematic diagram of two electrodes: (a) Case I: input&output modulation, (b) Case II: mirror modulation. . . . . . . . . . . . . . . . . . . . . . . . . . . . . . . . . . 29
2.14 Link gain versus RF input power under different bias configuration for input-output modulation schematic (Case I). . . . . . . . . . . . . . . . . . . . . . . . . . . . . . 30
2.15 Link gain versus RF input power under different bias configuration for mirror modulation schematic (Case II). . . . . . . . . . . . . . . . . . . . . . . . . . . . . . . 30

3.1 Behavioral model parameter extraction procedure: main steps from measurements to model validation. . . . . . . . . . . . . . . . . . . . . . . . . . . . . . . . . . . 33
3.2 Experimental setup. . . . . . . . . . . . . . . . . . . . . . . . . . . . . . . . . . . . 34

3.3 TDMLP based model with $2 \times (m+1)$ input nodes, $m$ is the number of memory depth, $z^{-1}$ is for unit delay operation, $M$ hidden nodes and two output nodes. . . . 37
3.4 The training performance of the TDMLP based model for the RSOA modulator with memory depth of 3 and hidden nodes of 20. . . . . . . . . . . . . . . . . . . . . . . . . 41
3.5 Measured and modeled outputs in-phase (a) and quadrature (b) parts in time domain. 42
3.6 Normalized power spectral density of measured and modeled outputs. . . . . . . . . 43
3.7 Normalized constellation (red '+' for the transmitted symbol, blue '·' for the measured output, and green 'x' for the TDMLP model output). . . . . . . . . . . . . . . 43
3.8 Dynamic AM-AM (a) and AM-PM (b) characteristics of the RSOA modulator. . . . . 44
3.9 Measured and modeled in-phase waveform (a) and quadrature waveform (b) in time domain. . . . . . . . . . . . . . . . . . . . . . . . . . . . . . . . . . . . . . . . . 49
3.10 Normalized power spectral density of measured and modeled outputs. . . . . . . . . 50
3.11 Normalized constellation (red '+' for the transmitted symbol, blue '·' for the measured output, and green 'x' for the GMP model output). . . . . . . . . . . . . . . . . 51
3.12 Dynamic AM-AM (a) and dynamic AM-PM (b) characteristics of the RSOA modulator. 52
3.13 The concept of harmonic superposition [2]. . . . . . . . . . . . . . . . . . . . . . . . 53
3.14 NVNA based X-parameter extraction setup [3]. . . . . . . . . . . . . . . . . . . . . . 54
3.15 Extraction of X-parameters based on the physical model of RSOA. . . . . . . . . . . 55
3.16 Plots of various types of X-paramters as a function of large signal amplitude ($|A_{11}|$). 56
3.17 Schematic diagram of simulation with X-parameters data. . . . . . . . . . . . . . . 57
3.18 Fundamental magnitude (left) and phase (right) as a function of the input power under different carrier frequencies of 0.7 GHz, 1.2 GHz, 1.7 GHz and 2.0 GHz. . . . . 58
3.19 Third harmonic magnitude (left) and phase (right) as a function of the input power under different carrier frequencies of 0.7 GHz, 1.2 GHz, 1.7 GHz and 2.0 GHz. . . . . 58
3.20 Fundamental and IMD3 as a function of the RF input power under two-tone test at different bias currents of 60 mA, 90 mA and 120 mA. . . . . . . . . . . . . . . . . 59

4.1 Response spectral of a nonlinear device to a two-tone excitation with frequencies $\omega_1$ and $\omega_2$. . . . . . . . . . . . . . . . . . . . . . . . . . . . . . . . . . . . . . . . 62
4.2 Schematic diagrams of electrical compensation. (a): feedforward and (b): predistortion. 63
4.3 Schematic diagram of predistortion characterization by using indirect learning architecture. . . . . . . . . . . . . . . . . . . . . . . . . . . . . . . . . . . . . . . . 65
4.4 *P*th order inverse: (a) pre-inverse and (b) post-inverse. . . . . . . . . . . . . . . . . 65
4.5 Dynamic AM-AM characteristics of the RSOA modulator without DPD, with DPD and predistorted signal. . . . . . . . . . . . . . . . . . . . . . . . . . . . . . . . . 68
4.6 Dynamic AM-PM characteristics of the RSOA modulator without DPD, with DPD and predistorted signal. . . . . . . . . . . . . . . . . . . . . . . . . . . . . . . . . 69
4.7 Normalized output power spectra of the RSOA modulator without DPD, with DPD and spectrum of the transmitted signal. . . . . . . . . . . . . . . . . . . . . . . . . 69
4.8 Normalized constellation. (blue 'x' for without DPD, green '·' for with DPD, and red '+' for the transmitted symbols). . . . . . . . . . . . . . . . . . . . . . . . . . . . . 70

5.1 FUTON architecture [4]. . . . . . . . . . . . . . . . . . . . . . . . . . . . . . . . . 72
5.2 Detailed uplink system power budget for RSOA-based links [4]. . . . . . . . . . . . 74
5.3 IF frequency plan for a 2×4-channel RoF link architecture in the FUTON project. (CMS: control/monitor/synchronization) . . . . . . . . . . . . . . . . . . . . . . . 75
5.4 Basic schematic diagram of the optical SCM. . . . . . . . . . . . . . . . . . . . . . 76

5.5 Simulation diagram for 4-channel uplink transmission in the FUTON system. . . . 76
5.6 Generated wideband SCM signal for Case IV. . . . . . . . . . . . . . . . . . . . . . . 77
5.7 Received wideband SCM signal for Case IV. . . . . . . . . . . . . . . . . . . . . . . . 78
5.8 Simulation results for IFFT size of 64 and 64QAM. single channel at 900 MHz. . . . 80
5.9 Simulation results for IFFT size of 512 and 64QAM. single channel at 900 MHz. . . . 80
5.10 Simulation results for IFFT size of 1024 and 256QAM. single channel at 900 MHz. . 81
5.11 Simulation results for IFFT size of 2048 and 256QAM. single channel at 900 MHz. . 81
5.12 Constellations of the SCM signal for Case IV at RF input powers of -5 dBm (right) and 4 dBm (left). (a) and (b): channel 1; (c) and (d): channel 2; (e) and (f): channel 3; (g) and (h): channel 4. . . . . . . . . . . . . . . . . . . . . . . . . . . . . . . . . . . . 82
5.13 Measurement setup. . . . . . . . . . . . . . . . . . . . . . . . . . . . . . . . . . . . 83
5.14 Spectrum of the SCM. . . . . . . . . . . . . . . . . . . . . . . . . . . . . . . . . . . 84
5.15 Measured EVM for single channel and four-channel signals versus RF input power. 84

*This page is intentionally left blank.*

# List of Tables

2.1 RSOA physical dimension and extracted parameters . . . . . . . . . . . . . . . . . . . 19

3.1 TDMLP model performance versus memory depth and the number of hidden nodes. 40
3.2 Performance of the GMP model versus nonlinear orders and memory depths. . . . . 50

*This page is intentionally left blank.*

# Chapter 1

# Introduction

*The main focus of this thesis lies on the investigation of the dynamical properties of Semiconductor Optical Amplifier (SOA) or specifically Reflective Semiconductor Optical Amplifier (RSOA). The various contributions during my PhD research are presented.*

## 1.1 Radio over Fiber (RoF) Links

The integration of optical fiber and wireless communication has been the development trend of the future communication systems [5–9]. The fundamental principle of RoF is that Radio Frequency (RF) (analog) radio signals are transmitted through an optical fiber link [10]. The use of radio signals means that the link is analog in nature and its performance must be characterized.

RoF is an essential technology for broadband wireless communications in a range of applications including last mile solutions, extension of existing radio coverage and capacity and backhaul. The well known advantages of deploying optical fiber as transmission medium such as low cost, low attenuation, large bandwidth, and immunity to electromagnetic interference make it the most flexible solution for transporting radio signals from/to Central Unit (CU) to/from Remote Access Units (RAUs). RoF also enables us to integrate multiple services over a single fiber with Subcarrier Multiplexing (SCM) and Wavelength Division Multiplexing (WDM) techniques.

Due to its simplicity, a RoF link based on the most popular Intensity-Modulation Direct-Detection (IMDD) scheme [11] is shown in Fig. 1.1. The main components in the RoF link include an Electrical-to-Optical Conversion (E/O) converter at the transmitter side, optical fiber, and Optical-to-Electrical Conversion (O/E) converter at the receiver side. The E/O converter plays a role of modulating an optical carrier intensity with an electrical signal, for instance,RF signal. The optical fiber with transparency property delivers the modulated optical signal from the transmitter to the receiver. The O/E performs an inverse operation of the E/O to convert the optical signal to the electrical signal. In the IMDD communication system the O/E is usually implemented by a photodetector.

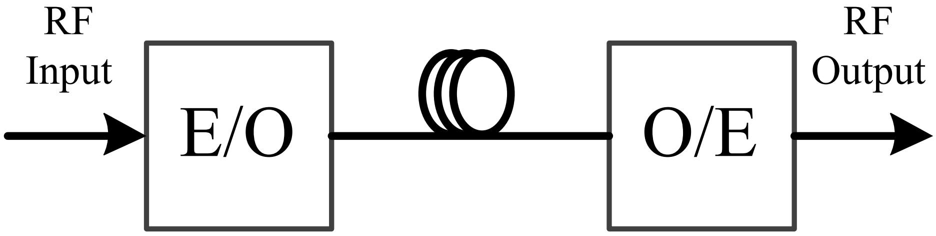

**Figure 1.1: A general RoF link using a simple IMDD scheme. main components include E/O conversion, optical fiber and O/E conversion.**

There are three types of RoF links presented in [1] (shown in Fig. 1.2).

- Directly Modulated Laser (DML)

  A DFB laser is typically considered to act as DML due to its narrow spectral linewidth, low noise and high linearity. The electrical signal is directly injected at the bias of the laser to modulate its intensity.

- Mach-Zehnder Modulator (MZM)

  This is a more complex and more expensive option than DML because it requires two optical components; an unmodulated laser and a MZM. However, the MZM approach may possibly offer improved performance in terms of noise and distortion compared to the DML, especially if distortion compensation techniques are considered. The MZM link type is not constrained by the availability of analog lasers at preferred wavelengths; this flexibility means that MZM links could be used with Dense Wavelength Division Multiplexing (DWDM) wavelengths to provide greater capacity. MZM links can be used for both uplink and downlink directions, although temperature stability may cause concern for the uplink direction. Bias drifting is an issue as the gain is dependent on the MZM bias point.

- RSOA modulator

  Unlike the DML and MZM approaches, the RSOA modulator is used only for the uplink direction, replacing the laser diode in the RAUs by a RSOA due to the limit of the modulation bandwidth, conferring flexibility to the optical network design, through the centralization of the optical sources. It uses the seed light from an optical source in the CU and therefore does not require an extra optical source in RAU. In WDM systems, this allows to manage the wavelength plan from the CU, without modifications in the optical terminal equipments and reduce the network cost. The RSOA link can provide more flexible and dynamically reconfigurable optical network architecture due to its colorless property [1].

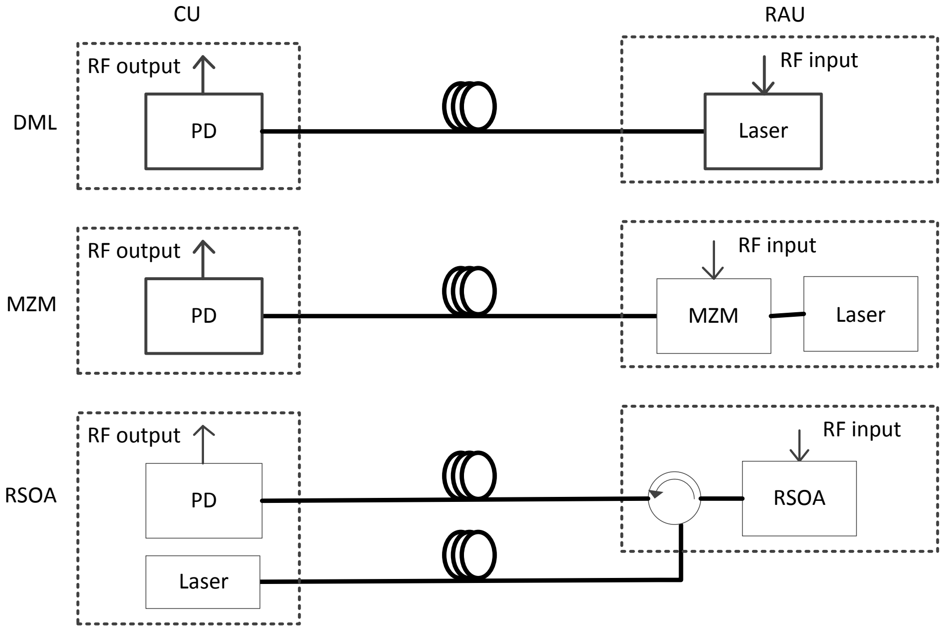

Figure 1.2: Schematic of radio over fiber links [1].

## 1.2 Distributed Antenna System (DAS)

One of the main applications of RoF is a DAS. The concept of the DAS was originally proposed to improve the coverage performance of indoor wireless communication systems [12, 13]. In recent years the DAS has drawn much attention in cellular communications for supporting outdoor coverage and capacity [14, 15]. As mobile wireless applications become increasingly popular, the next-generation wireless communication systems will need to provide higher data transmission rate, higher RF transmission bandwidth and higher mobility connection when compared with current networks. For instance, the Third Generation Partnership Project (3GPP) Long Term Evolution (LTE) is a highly flexible radio interface. Bandwidth extension in LTE-Advanced is supported via carrier aggregation [16]. Carrier aggregation allows an overall transmission bandwidths of up to 100 MHz, enabling peak target data rates in excess of 1 Gbps for downlink and 500 Mbps for uplink to be achieved [17, 18]. In this context, the most effective way to improve the throughput per user is to deploy networks with a small cell size to reduce the number of users per cell [19]. The small cell architectures such as Picocell, Femtocell and DAS have attracted the attention of standardization bodies, such as 3GPP.

In EU Fibre Optic Networks for Distributed and Extendible Heterogeneous Radio Architectures and Service Provisioning (FUTON) project [4], a large number of RAUs, where the RAU antennas act as elements of a virtual Multiple Input Multiple Output (MIMO) architecture proposed, are geographically distributed over a large area and connected to a CU via optical fiber [20], in order to provide enhanced cellular coverage and capacity.

## 1.3 Reflective Semiconductor Optical Amplifier

RSOAs have recently attracted much interest of many researchers because of their nonlinear function [21], noise reduction [22], amplification [23], and modulation properties [24–28].

A RSOA is similar to a SOA. For the RSOA, however, the High Reflective (HR) coating is about 95 % at rear facet. The Anti reflective (AR) coating is added at the input fact and reflectivity is around $1 \times 10^{-3}\%$. SOAs and RSOAs are typically made from groiup III-V compound direct band gap semiconductors (e.g. InP/InGaAsP, GaAs/AlGaAs, InP/InGaAs, and InP/InAlGaAs). Comparing devices with the same characteristics SOA and RSOA (physical dimensions and design), the RSOA has more optical and E/O gain. The SOA requires higher biasing currents to reach the same gain. For the same current and input optical power the RSOA reaches a higher level of saturation. The large biasing currents can raise an issue of power dissipation in a unit placed remotely. The RSOA used in this study and designed at Alcatel-Thales III-V Laboratory in France has a wide optical bandwidth, which is around 50 nm as depicted in Fig. 1.3. Therefore, it can be used over a wide range of wavelengths.

## 1.4 Motivation and Objectives

An accurate physical model will contribute to optimally designing of devices and predicting the characteristics of devices. Connelly [29–31] presented a wideband physical model of a bulk InP-InGaAsP SOA. In the model, the relationship between spontaneous and stimulated emission is clarified. Spontaneous emission within the amplifier is modeled by traveling wave power equation. The

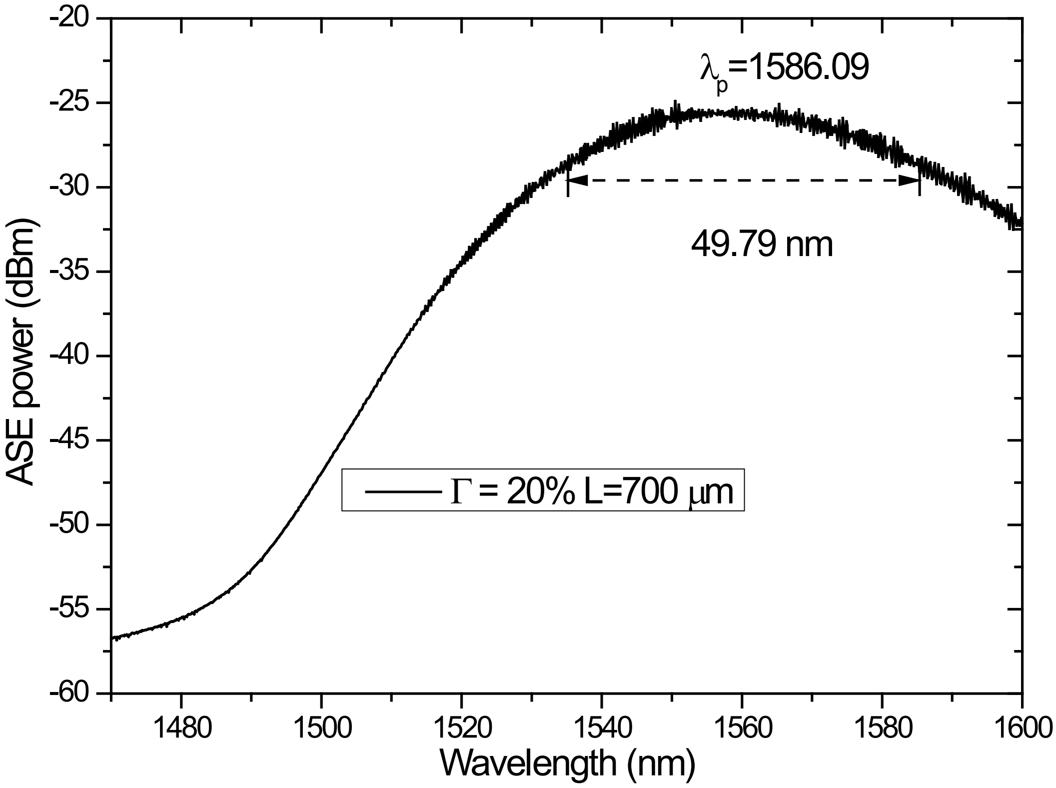

**Figure 1.3: RSOA spectrum with low optical confinement.**

model can be applied to determine the steady-state properties of an SOA. A parameter extraction algorithm is required to obtain the accurate intrinsic parameters. In 2008, Kuntze *et al.* [32] proposed an analytical state-space model for SOA dynamics with nonlinear gain compression. The model was possible with polynomial gain compression and position-independent carrier density. This compressed model showed more accurate than existing non-compressed models. Runge *et al.* [33] proposed a time domain model for ultralong SOAs, which can be regarded as being divided into an amplifying section and a saturated section. Based on the model, a simulation to generate a widely tunable short pulse (less than 2 ps) was performed [34]. More recently, Connelly proposed a physical model for pulse (39.6 ps pulse width) propagation in RSOA in order to predict the gain dynamics, spatial dependence of the pulse shape, and dynamic chirp [23].

Nielsen *et al.* [35] presented a transfer function to explain the resonant behavior of the small-signal frequency response in a SOA used as a wavelength converter. Morel and Sharaiha [36] derived a time-domain transfer matrix model for short pulse (picosecond) propagation in SOAs. Razaghi *et al.* [37] proposed a modified nonlinear Schrödinger equation based model for pulse propagation in the counter-propagation regime. In the model, group velocity dispersion, two-photon absorption[1], and ultrafast nonlinear refraction are included, which are more important for pulse propagation.

All models of SOAs and RSOAs discussed above are applied for pulse amplification and propagation, wavelength converter. Therefore, these models are significantly more complicated and consequently require more advanced numerical techniques to solve, which sometimes require significantly more computation time. To the best of our knowledge, there is no physical model of the RSOA modulator for analog RoF applications.

Unlike physical model, a behavioral model, also called a black box, focuses on the relation between the input and output signals of devices or systems. The behavioral model can avoid the intrinsic parameters extraction of a device. The key advantage of the behavioral model is that it does not require deep knowledge of the physics and functionality of the device. Currently behavioral modeling techniques have been considered to characterize RF power amplifiers [38], predistorters [39,40], and even laser [41], Erbium-Doped Fiber Amplifier (EDFA) [42] and SOA [43,44]. In [43], a black-box model, which does not use any intrinsic device parameters, has presented to characterize the spectral gain and noise in SOAs. In [44], An Artificial Neural Network (ANN) based behavioral model for Quantum-Dot SOAs (QD-SOAs) has been characterized by accuracy and validity for wide range of input parameters such as pulse width, energy, normalized injection rate, and frequency shift.

Volterra series was first developed in 1887 by Vito Volterra. It is a model for nonlinear behavior, similar to the Taylor series. It differs from the Taylor series in its ability to capture memory effects of devices. It is a general nonlinear model with memory [45] and has been successfully used to model PAs with memory effect [46], which is limited to mild nonlinearities due to the highly expensive computational task and complicated algorithm involved [47]. However, a serious drawback of the Volterra model is the large number of coefficients that must be extracted even though some contributions to reduce the complexity of Volterra series [38, 48].

Ku and Kenney [49] proposed a new behavioral model which treats memory effects in nonlinear power amplifiers. The model is based on a memory polynomial, and a sparse delay tap structure was used to reduce the parameter space required for accurate model identification. A baseband behavior of PA was described using a complex polynomial by Kim et al. [50]. Ding et al. [51] proposed a behavioral model based on memory polynomials for a digital baseband predistorter and implemented it using indirect learning architecture. However, the conventional polynomial model exhibits nu-

---

[1] It is a process involving the simultaneous absorption of two photons whose combined energy is sufficient to induce a molecule transition to an excited electronic state.

merical instabilities when higher order terms are included [52]. Raich et al. [52] presented a set of orthogonal polynomials, which can be used for PA as well as predistorter modeling. The orthogonal polynomials can alleviate the numerical instability problem associated with the conventional polynomials. Vieira et al. [53] presented a model for directly modulated laser using memory polynomials which basically based on the predistorter model in [50, 51]. The measured baseband signal was used to extract the parameters of the model.

Analog RoF links suffer from nonlinear distortions[2] induced mainly by the modulating device [54], specifically RSOA modulator in our case. The nonlinear distortions generated by the modulator such as harmonic and intermodulation distortions significantly limit the overall dynamic range and performance of the RoF links. Therefore, linearization techniques should be considered to improve the performance of the links. The compensation can be done in both the optical and electrical domains [54]. In [55, 56], cascaded MZMs architectures have been proposed to eliminate both the third and fifth distortions in the optical domain. Dual parallel MZMs method has been proposed to linearize the transfer function of the MZMs [57]. In [58, 59], a Distributed Feedback (DFB) laser has been linearized by using external light-injected cross-gain modulation. Tabatabai *et al.* [60] have proposed a feedforward linearization technique in the optical domain to improve the linearity and suppressing the Four-Wave Mixing (FWM) of a SOA. The operation of the feedforward scheme is based on the subtraction of two equal signals with subsequent cancellation of the error signal in the output spectrum of the devices. All these approaches have complicated architectures, and high expenses due to the requirement of additional optical devices.

In the electrical domain, most popular linearization techniques are feedforward and predistortion, which have been widely applied to the RF power amplifiers [40, 50, 51, 61–63]. A feedforward linearization scheme has been presented in [64, 65]. Additional photodetector and laser are also required. Urick *et al.* [66] have proposed a wideband predistortion linearization for an electro-optic MZM in analog fiber optic links. Based on a pair of antiparallel diodes, an analog broadband predistortion circuit has been designed to linearize electro-absorption modulators [67].

The objective of this thesis is to modeling of the RSOA modulator used in the RoF links. Our research efforts focus on the following areas:

---

[2] The nonlinearity and dispersion of an optical fiber are beyond the scope of this thesis.

- Develop a simple physical model for the RSOA modulator for RoF applications. Detailed analysis regarding harmonic and intermodualtion distortions, transmission performance, distribution of the carriers is performed.
- Develop black-box models in system level enabling to investigate the RSOA modulator from another perspective.
- Attempt to compensate the nonlinear distortion caused by the RSOA modulator due to its nonlinearity.
- Predict the transmission performance of the wideband SCM based systems based on the developed physical model.

## 1.5 Thesis Overview

The rest of this thesis is organized as follows. Chapter 2 proposes a simplified physical model for a RSOA modulator in RoF link based on rate equation and traveling-wave equations under some approximations. The model is implemented using Symbolically Defined Devices (SDD) in Advanced Design System (ADS). The model parameters are extracted using optimization tool in ADS. The static and dynamic characteristics of the RSOA modulator are presented.

Chapter 3 discusses behavioral modeling of the RSOA modulator using three methods such as Generalized Memory Polynomial (GMP), Tapped-Delay Multilayer Perceptron (TDMLP) and X-parameters[3]. A comparison between the methods are made. Nonlinear distortion and memory effect are described by plotting the dynamic Amplitude-to-Amplitude Conversion (AM-AM) and dynamic Amplitude-to-Phase Conversion (AM-PM) characteristics of the RSOA modulator. For the X-parameters based model the one-tone and two-tone tests are used in order to characterize the nonlinearity of the RSOA modulator.

A Digital Predistortion (DPD) based compensation technique is investigated in Chapter 4. Memory effects are considered in the DPD model in order to improve the linearization performance. The dynamic AM-AM and AM-PM characteristics of the RSOA modulator without and with DPD are demonstrated. The improvement for linearity of the RSOA is obtained.

Chapter 5 describes the prediction of the transmission performance of FUTON system. The optical transport system uses the SCM, where the transmission over the optical fiber is at an Interme-

---

[3] X-parameters is a registered trademark of Agilent Technologies.

diate Frequency (IF). The performance of four channels is demonstrated with different modulation schemes and data rates, which keep the channel bandwidth of 100 MHz as proposed in the FUTON project.

Finally, the thesis ends with Chapter 6, where conclusions are drawn and recommendations for future work are also made.

## 1.6 Research Contribution

Main publications during my PhD study are listed as follows:

***Papers in Journals:***

1. Z. Liu, M. A. Violas, and N. B. Carvalho, “Modeling and simulation of a reflective semiconductor optical Amplifier modulator using X-parameters,” IEEE Photon. Technol. Lett., vol. 25, no. 3, pp. 272-274, Feb. 2013.

2. Z. Liu, M. A. Violas, and N. B. Carvalho, “Wideband dynamic behavioral modeling of reflective semiconductor optical amplifiers using a tapped-delay multilayer perceptron,” Opt. Express, vol. 21, no. 3, pp. 3354-3362, Feb. 2013.

3. Z. Liu, M. A. Violas, and N. B. Carvalho, “Analysis on dynamic characteristics of reflective semiconductor optical amplifier based on a memory polynomial model,” Microw. Opt. Technol. Lett., vol. 54, no. 3, pp. 805-808, March, 2012.

4. Z. Liu, M. A. Violas, and N. B. Carvalho, “Digital predistortion for RSOAs as external modulators in radio over fiber systems,” Opt. Express, vol. 19, no. 18, pp. 17641-17646, Aug. 2011.

5. Z. Liu, M. Sadeghi, G. de Valicourt, R. Brenot, and M. Violas, “Experimental validation of a reflective semiconductor optical amplifier model used as a modulator in radio over fiber systems,” IEEE Photon. Technol. Lett., vol. 23, no. 9, pp. 576-578, May 2011.

6. G. de Valicourt, M. A. Violas, D. Wake, F. van Dijk, C. Ware, A. Enard, D. Maké, Z. Liu, M. Lamponi, G. H. Duan, and R. Brenot, “Radio over fiber access network architecture based on new optimized RSOA devices with large modulation bandwidth and high linearity,” IEEE Trans. Microw. Theory Tech., vol. 58, no. 11, pp. 3248-3258, Nov. 2010.

7. D. Wake, A. Nkansah, N. J. Gomes, G. de Valicourt, R. Brenot, M. Violas, Z. Liu, F. Ferreira, and S. Pato, “A comparison of radio over fiber link types for the support of wideband radio channels,” J. Lightw. Technol., vol.28, no. 16, pp.2416-2422, Aug. 2010.

***Papers in Conferences and Workshops:***

1. Z. Liu, M. A. Violas, and N. B. Carvalho, “Transmission of Four Channels SCM over Fiber and Nonlinear Compensation for RSOA External Modulators,” in IEEE Globecom, First Workshop on Distributed Antenna Systems for Broadband Mobile Communications, Houston USA, Dec. 2011.

2. Z. Liu, M. Violas, M. Sadeghi, and G. de Valicourt, “4 channels subcarrier multiplexing optical link using an RSOA modulator,” in IEEE Topical Meeting on Microwave Photonics (MWP’10), Montreal, Canada, Oct. 5-9, 2010.

3. D. Wake, A. Nkansah, P. Assimakopolous, N. Gomes, M. Violas, Z. Liu, S. Pato, F. Ferreira, G. de Valicourt, R. Brenot, and F. van Dijk, “Design and performance of radio over fiber links for next generation wireless systems using distributed antennas,” in Proc. ICT Future Network & Mobile Summit 2010, Florence, Italy, 16-18 June, 2010.

# Chapter 2

# Physical Modeling and Simulation of RSOA

*A simplified time domain physical model for a bulk RSOA modulator is proposed. The light wave propagation can be modeled with traveling wave equations, and carrier rate equation can be used to describe the interaction between the light and the gain medium. In order to solve these equations the multi-section model is implemented by using SDD in ADS. The static and dynamic characteristics are demonstrated with measurement and simulation. The spatial distribution of carrier density, signal photon density and Amplified Spontaneous Emission (ASE) photon density inside RSOA are also simulated by using the proposed model in this chapter. The model has potential applications in aiding design and optimization of the RSOA, and can also be used to predict the behavior of optical systems incorporating RSOA, such as SCM based multi-channel transmission systems, which will be addressed in chapter 5.*

## 2.1 Introduction

As mentioned previously, the goal of this chapter is not to propose a complex model and consider all physical parameters in a RSOA device but to investigate the static and dynamic characteristics of the RSOA used in RoF links with simplification under some assumptions.

The effect of the physical parameters in the context of SOA and RSOA has not been thoroughly studied so far. The device modeling task has become an outstanding research area [23,31,32,36,68]. In this chapter we focus on the physical modeling of a bulk RSOA modulator based on the rate equation and the traveling-wave equations. Previous works have addressed the nonlinear compression gain [69] and ASE [30]. However they have not been considered and implemented simultaneously in a current-injected RSOA modulator model. In our model both nonlinear gain saturation effect and the ASE on the carrier density have been considered.

To make the model suitable to analog RoF applications, some approximations have been made.

- Since, as a modulator, the RSOA will be mainly illuminated by a Continuous Wave (CW) optical source such as a DFB laser, the material gain is assumed to vary linearly with the carrier density but with wavelength independence.
- The ASE power noise is assumed to be Gaussian white noise with an equivalent optical noise bandwidth.
- For the sake of simplicity the effect of carrier diffusion is ignored. It is valid when the length of active region is longer than carrier diffusion length, which is typically in order of micrometer [70, 71].
- In order to further simplify the model, the non-radiative Auger recombination is approximately proportional to the cube of carrier density.
- The effects of linear radiative and non-radiative recombination, bimolecular radiative and non-radiative recombination are not distinguished.

## 2.2 Physical Modeling

### 2.2.1 Rate Equation

Generally, the carrier density is increased by the bias current and decreased by several recombination mechanisms. As mentioned previously, the carrier rate equation, representing the active region interaction between photons and carriers, can be described as

$$\frac{\partial N(z,t)}{\partial t} = \frac{I}{edwL} - R(N) - g_{net}\nu_g S(z,t) - g_{net}\nu_g S_{ASE}(z,t) \tag{2.1}$$

where $N$ is the active region's carrier density, $I$ is the injected current of RSOA, $L$, $w$ and $d$ are length, width and thickness of the active region of RSOA, respectively. $e$ is the electron charge. The second term to fourth term on the right hand in (2.1) represents the spontaneous recombination rate, stimulated emission recombination rate and ASE optical field, respectively. $g_{net}$ is the net gain.

$\nu_g$ is the group velocity. $S(z)$ and $S_{ASE}(z)$ are the signal photon density and ASE photon density, respectively.

$R(N)$ in (2.1) is expressed by a polynomial [72]

$$R(N) = AN + BN^2 + C_{aug}N^3 \tag{2.2}$$

where $A$, $B$ and $C_{aug}$ are linear radiative and non-radiative recombination coefficient, bimolecular radiative and non-radiative recombination coefficient, and Auger recombination coefficient, respectively. The carrier lifetime $\tau(N)$ dependent on the carrier density is equal to $1/(A+BN+C_{aug}N^2)$. The modulation bandwidth of the RSOA modulator is mainly limited by the carrier lifetime.

In general the material gain as a function of carrier density for a bulk SOA or RSOA is approximated using a linear expression [73]. In our model the effect of gain saturation is considered by introducing a gain saturation factor. Thus, the net gain $g_{net}$ in (2.1) is presented as

$$g_{net} = \Gamma g_c - \alpha_{\text{int}} \tag{2.3}$$

where $\alpha_{\text{int}}$ and $g_c$ are the internal waveguide loss and the gain compression, respectively, and given by

$$a_{\text{int}} = K_0 + \Gamma K_1 N \tag{2.4}$$

$$g_c = \frac{g_m}{1 + \varepsilon S_{tot}} \tag{2.5}$$

where $K_0$ and $K_1$ are the carrier independent absorption loss coefficient and carrier dependent absorption loss coefficient, respectively. $K_0$ represents the intrinsic material loss and $K_1$ is mainly due to intervalence band absorption. $\varepsilon$ represents the gain saturation fact, $S_{tot}$ is the total photon density, $g_m$ is the material gain coefficient given by

$$g_m = g_d(N - N_0) \tag{2.6}$$

where $g_d$ is the differential gain, $N_0$ is the carrier density at transparency, $\Gamma$ is the optical confinement factor.

The signal photon density $S(z)$ of each section in the model has a relation with optical power and can be described as [68]

$$S(z) = \frac{P^{+}(z) + P^{-}(z)}{\nu_g \hbar \omega A_{eff}} \tag{2.7}$$

where $P^{+}$ and $P^{-}$ are the signal powers of the forward and reverse optical signals, respectively, and will be defined in the next subsection. $\hbar$ is the reduced Planck's constant. $\omega$ is the optical angular frequency. $A_{eff} = wd/\Gamma$ is the effective area of the active layer.

$S_{ASE}(z)$ in (2.1) can be depicted by

$$S_{ASE}(z) = \frac{N^{+}_{ASE}(z) + N^{-}_{ASE}(z)}{\nu_g \hbar \omega A_{eff}} \tag{2.8}$$

where $N^{+}_{ASE}$ and $N^{-}_{ASE}$ are the forward and backward ASE powers, respectively, and will be defined in Subsection 2.2.3

### 2.2.2 Traveling-Wave Equations for Optical Signal

The optical signal enters the input facet travels along the device been amplified and reflected at the other facet and amplified again while traveling in the reverse direction. The forward and reverse propagating optical fields at z are described by the equations as follow

$$\frac{\partial P^{\pm}(z,t)}{\partial z} = \pm g_{net} P^{\pm}(z,t) \tag{2.9}$$

By solving (2.9) for each section[1], we obtain the relation between the input optical power and the output optical power for each section of the RSOA model as follows

$$P^{\pm}(z \pm \Delta z) = P^{\pm}(z) e^{g_{net} \Delta z} \tag{2.10}$$

These equations are obeyed to the following boundary conditions at the input and output facets of the RSOA.

$$\begin{aligned} P^{+}(0) &= (1 - R_1) P_{in} + R_1 P^{-}(0) \\ P^{-}(L) &= R_2 P^{+}(L) \end{aligned} \tag{2.11}$$

---

[1] The active region will be divided into multiple smaller sections to solve the traveling-wave equations for optical signal and ASE noise.

where $R_1$ and $R_2$ are the reflection coefficients at the front facet and rear facet of RSOA, respectively.

### 2.2.3 Traveling-Wave Equations for ASE

ASE is the main noise source in a RSOA and determines the RSOA static and dynamic performance under the low input optical power. The modeling of ASE is an important issue but quite complex and difficult one. In the model proposed we made some assumptions in order to simplify modeling. ASE spectrum covers a very large range of wavelength spectrum and shows parabolic shape. We simplified this approach by assuming a constant average ASE spectrum density and defining noise bandwidth $B_0$, which is estimated at $10 \times 10^{12}$ Hz. Assuming that the carrier density is constant in the length of each RSOA section, the power of ASE generated by the section active region is given by

$$P_{ASE} = (e^{g_{net}} - 1) n_{sp} h v B_0 \tag{2.12}$$

where $n_{sp}$ is the spontaneous emission factor given by

$$n_{sp} = \frac{N}{N - N_0} \tag{2.13}$$

The ASE noise traveling-wave modeling implementation follows a similar procedure with the optical signal traveling wave. The spontaneous emission output power for each forward and reverse propagating signal has two contributions: the amplified input noise and the generated spontaneous emission component from the section. The forward and reverse propagating ASEs can be depicted by

$$\begin{aligned} N^{+}_{ASE}(z + \Delta z) &= P_{ASE}(1 - R_2) + N^{+}_{ASE}(z) e^{g_{net}} \\ N^{-}_{ASE}(z - \Delta z) &= P_{ASE} + N^{+}_{ASE}(z) e^{2 g_{net}} R_2 + N^{-}_{ASE}(z) e^{g_{net}} \end{aligned} \tag{2.14}$$

The boundary conditions above equations are as follows

$$\begin{aligned} N^{+}_{ASE}(0) &= R_1 N^{-}_{ASE}(0) \\ N^{-}_{ASE}(L) &= R_2 N^{+}_{ASE}(L) \end{aligned} \tag{2.15}$$

### 2.2.4 Model Implementation

As described previously, the active region of the RSOA is divided into multi smaller sections along the length as shown in Fig. 2.1(a). For each section the carrier density is considered to be a constant along the longitudinal direction. The rate equation and the traveling-wave equations are solved in each section. Fig. 2.1(b) represents the implementation of our model by means of a SDD built-in component under a commercially available software, ADS from Agilent Technologies. The SDD is a multi-port device which is defined by specifying algebraic relationships that relate the port voltages, currents, and even their derivatives, plus currents from certain other devices. Derivatives can be implemented by using a set of implicit equations in this component. The SDD component also permits ADS users to easily add custom behavioral, nonlinear system models. An advantage of using ADS is that several types of analysis, both linear and nonlinear in the frequency domain and time domain can be implemented. For instance, Harmonic Balance (HB) analysis is a popular frequency domain analysis technique for simulating harmonic and intermodulation distortions in nonlinear circuits and systems.

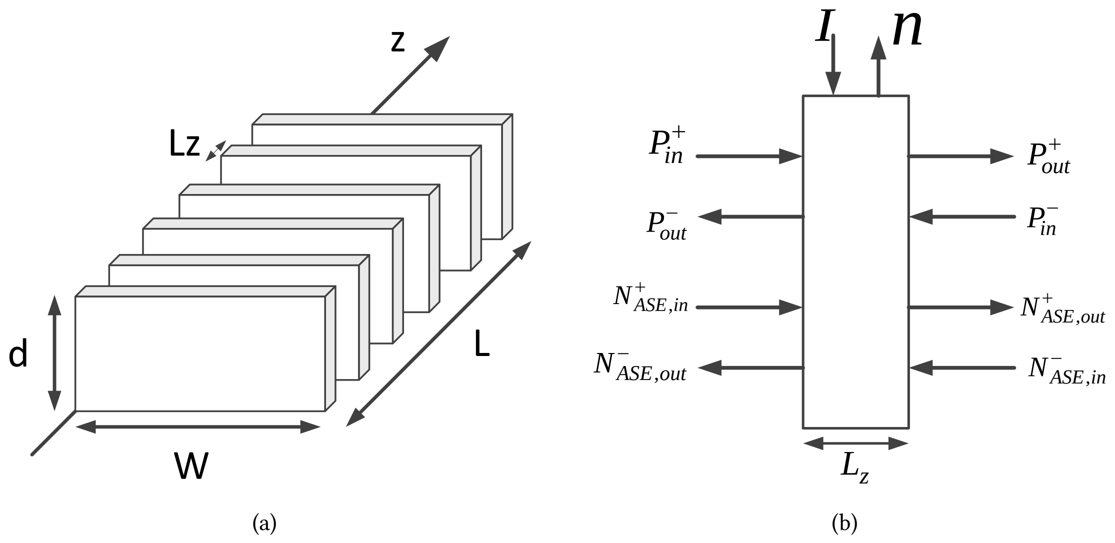

(a) (b)

**Figure 2.1: RSOA elementary section for numerical modeling. (a) multi-section schematic, (b) implementation using a SDD built-in component in ADS.**

To determine the number of the split sections in the active region, we observe the curve of the optical power versus bias current by sweeping the section number. The simulation result is depicted in Fig. 2.2. It is shown clearly that the curve of the optical power versus bias current are more stable with increasing the number of the sections. For instance, the curves for 12 sections and 14 sections are almost overlapped. Therefore, we use the 12-section model for further analysis. The full simulation schematic is shown in Fig. 2.3.

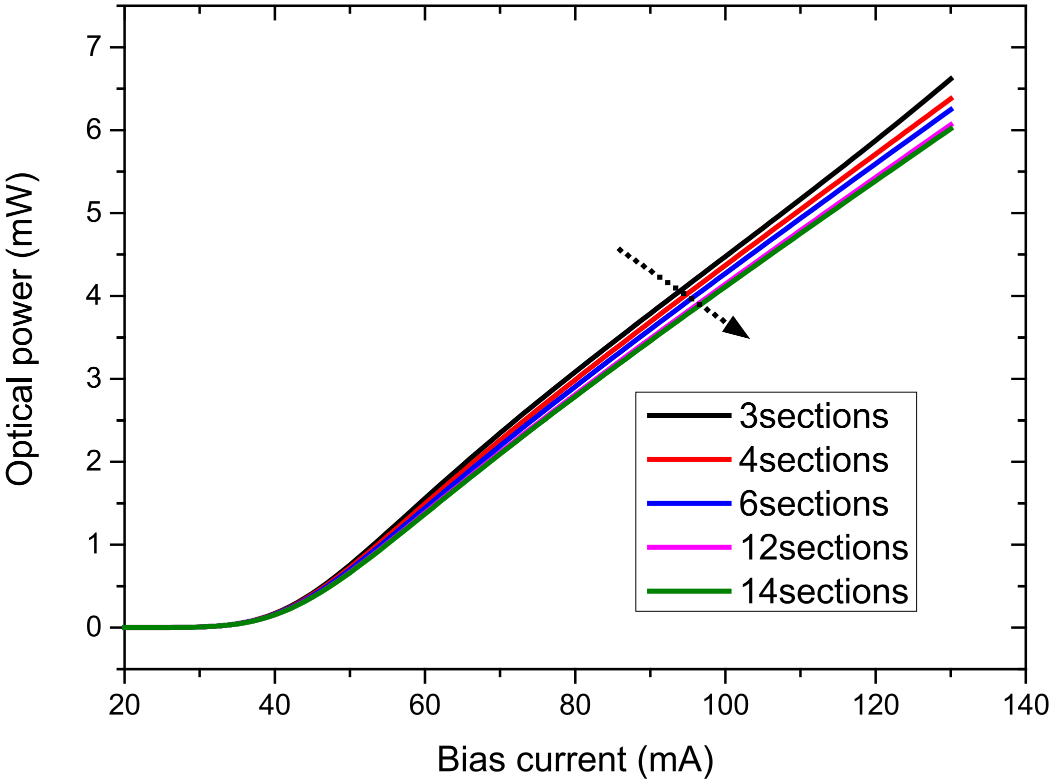

**Figure 2.2: Optical power versus bias currents for 3, 4, 6, 12 and 14 sections.**

### 2.2.5 Parameter Extraction

The reliability of models depends crucially on the validity of the parameters which appear in the models. The best values for the model parameters are found by fitting the simulated data as closely as possible to the measured data. A Data Access Component (DAC), which links the measurement data in ADS, enables us to carry out the extraction of the model parameters from real measurement data with a built-in optimization tool. The measured data, output powers versus bias currents, can be loaded into ADS simulator by the DAC. The optimization controller based on gradient algorithm is applied. The goal of optimization is to minimize the difference between the measured and simulated output powers. The extraction procedure is as following. A Direct Current (DC) simulator enables us to perform DC simulation to sweep all bias currents in order to extract the parameters of the RSOA model. The parameters of the RSOA can be updated after simulation finished. The simulation

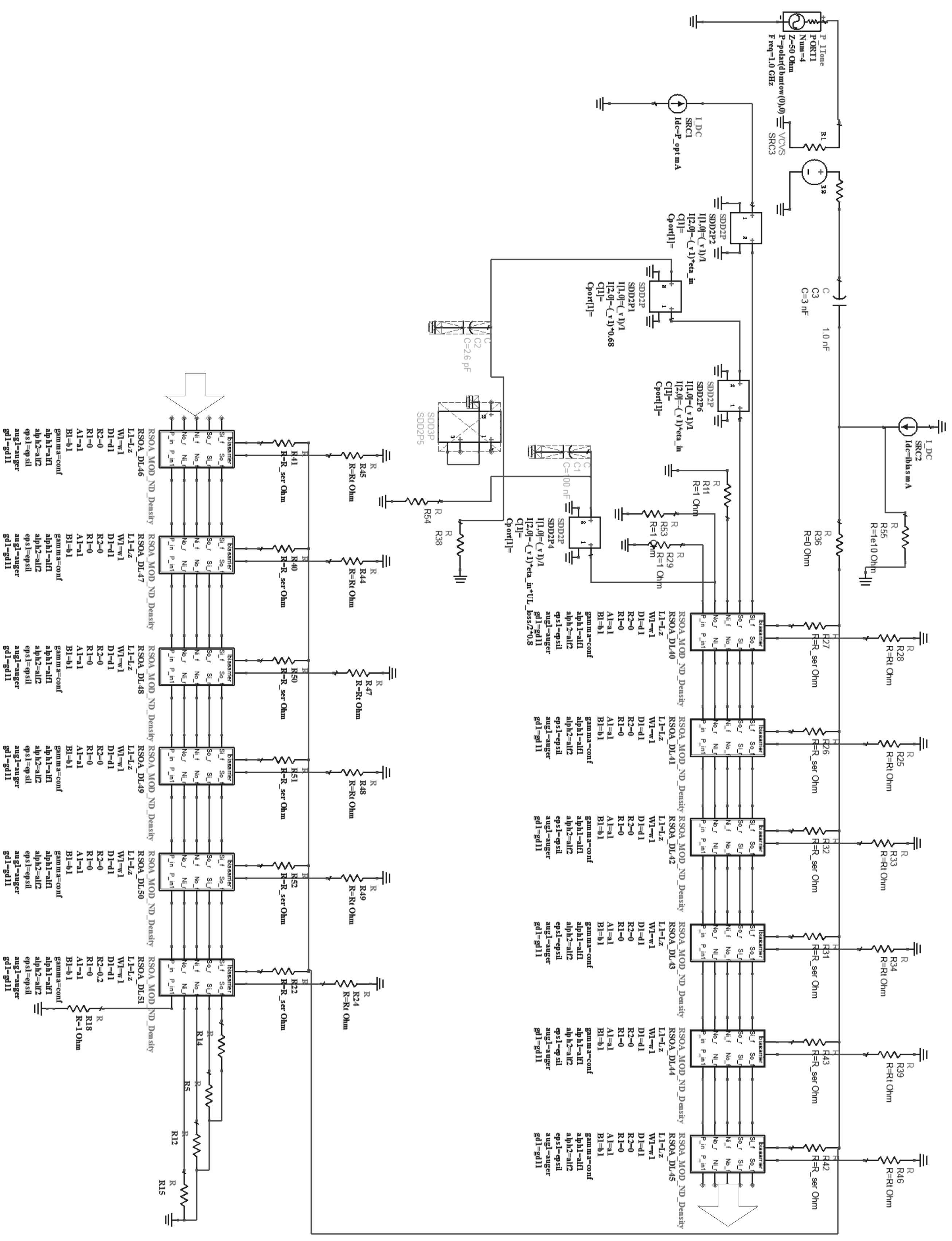

Figure 2.3: Simulation layout for the multi-section based RSOA model.

starts again based on the new parameters. After several periods above, the stable model parameters would be obtained. The extracted parameters of the RSOA modulator are shown in Table 2.1.

**Table 2.1: RSOA physical dimension and extracted parameters**

| Symbol | Parameters | Value | Unit |
|---|---|---|---|
| L | Active region length | 700 | µm |
| d | Active region thickness | 0.12 | µm |
| Γ | Optical confinement factor | 0.2 | – |
| $g_d$ | Differential gain | $4.0 \times 10^{-20}$ | $\mathrm{m}^{-2}$ |
| $\varepsilon$ | Gain saturation factor | $1.1 \times 10^{-22}$ | $\mathrm{m}^{3}$ |
| $A$ | Linear radiative and non-radiative recombination coefficient | $2.0 \times 10^{8}$ | $\mathrm{s}^{-1}$ |
| $B$ | Bimolecular radiative and non-radiative recombination coefficient | $1.9 \times 10^{-16}$ | $\mathrm{m}^{3}\mathrm{s}^{-1}$ |
| $C_{aug}$ | Auger recombination coefficient | $2.0 \times 10^{-41}$ | $\mathrm{m}^{6}\mathrm{s}^{-1}$ |
| $K_0$ | Carrier independent absorption loss coefficient | 9000 | $\mathrm{m}^{-1}$ |
| $K_1$ | Carrier dependent absorption loss coefficient | 2960 | $\mathrm{m}^{2}$ |

## 2.3 Results and Discussion

The experimental setup is shown in Fig. 2.4. The desired signal can be generated by Vector Signal Generator (VSG). A commercial broadband Amplifier (AMP), ZHL-42W, was used to drive the Device Under Test (DUT).A tunable RF attenuator was added to tune the RF input power of the DUT. A Vector Signal Analyzer (VSA) was used to obtain the output signals of the DUT. The seeding light of the RSOA designed by Alcatel-Thales III-V Labs is from a commercial DFB laser with the wavelength of 1550 nm, which is biased at 30 mA. The RSOA with the reflectivity of 20% at the rear facet. The optical input power of RSOA is set to -7 dBm by adjusting the optical tunable attenuator. An optical circulator is used to separate the forward and reverse optical signals. A Photodetector (PD) with the reflectivity of 0.8 A/W is used as a detector. A commercial RF amplifier, ZHL-42W, is used to drive the RSOA.

### 2.3.1 Static Characteristics

The optical powers versus bias current measurements were carried out. Only the DUT block in Fig. 2.4 is need with the PD removed. An optical power meter was used to measure the optical power

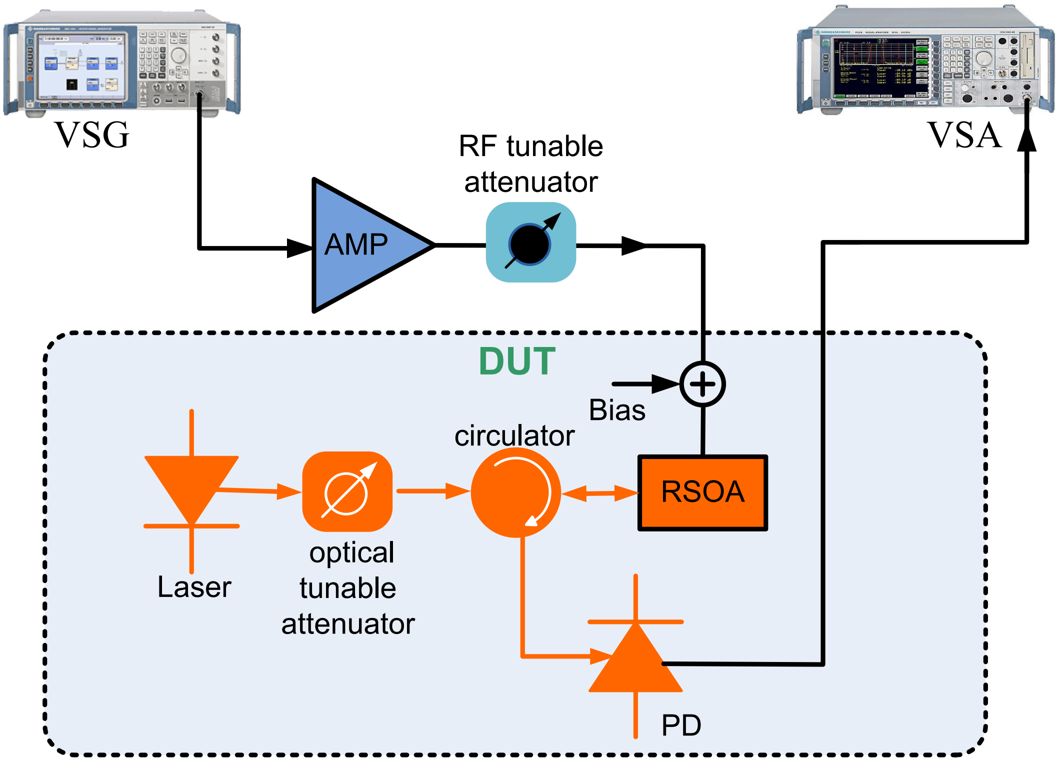

**Figure 2.4: Experimental test bench**

at the circulator output. By tuning the bias currents a set of optical output powers can be recorded and used for the parameter extraction process as we described previous section 2.2.5.

The measured and modeled the output optical powers versus bias currents are shown in Fig. 2.5. From the measured data, the threshold current is at 39 mA while the slope efficiency is at 0.06805 W/A. The modeled characteristic matches both threshold current and slope efficiency. Fig. 2.6 is a plot of the measured and modeled optical gain versus optical input powers at the different bias currents of 60 mA, 90 mA and 120 mA. A good agreement is achieved between the measurement and simulation. From the measurement data, the saturation power of the RSOA modulator at the bias currents of 90 mA is around -18 dBm.

### 2.3.2 Nonlinearity

It is common to use single-tone and two-tone measurements [74] in order to characterize the nonlinearity of the RSOA modulator using the test bench shown in Fig. 2.4. The first test is to use one tone signal in order to analyze the harmonic distortions. The RSOA was biased at 90 mA. Gain compression point and harmonic distortions can be demonstrated by using a single tone RF signal (1

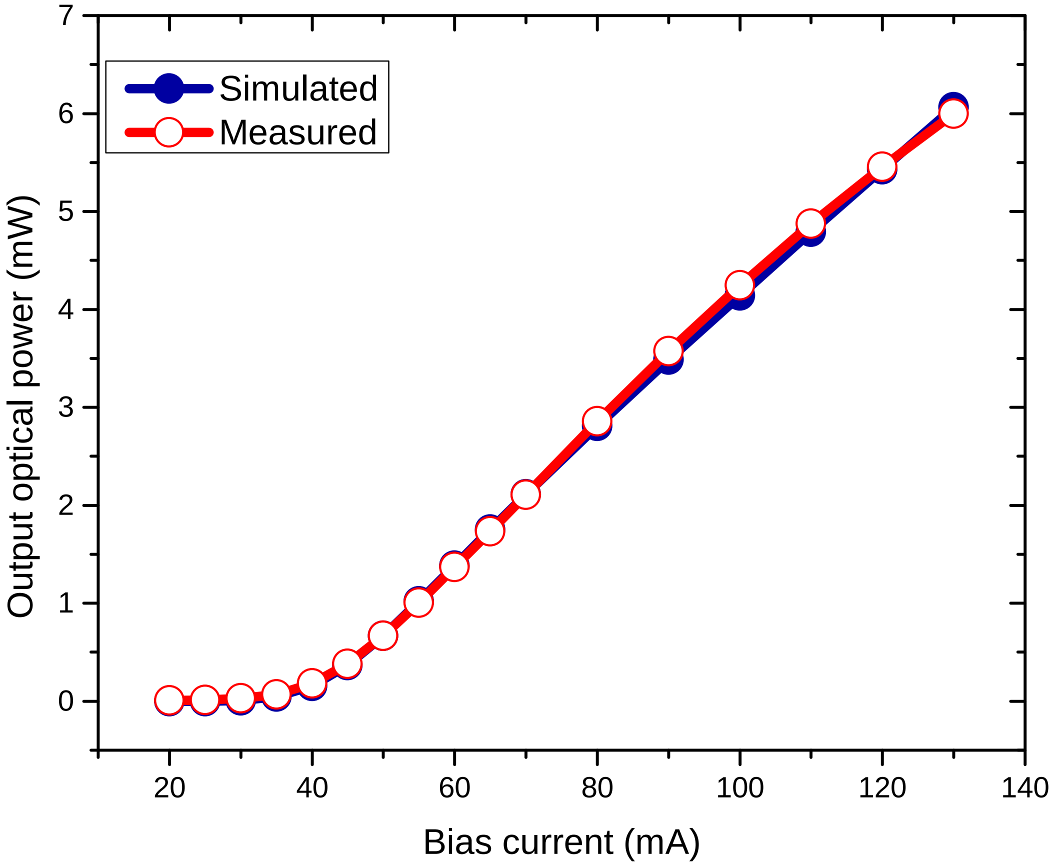

**Figure 2.5: Measured and simulated optical powers versus bias currents.**

GHz) generated by the VSG. The RF signal can be recovered by the PD. The RF output fundamental, 2nd- and 3rd-order harmonic distortion powers of the DUT were gathered by the VSA. The measured and modeled harmonic distortions are shown in Fig. 2.7. These enable us to evaluate an important figure of merit called the input 1 dB Compression Point (P1dB), which is defined as the input power level at which the signal output is already compressed by 1 dB as compared to the output that would be obtained by simply extrapolating the linear system's small signal characteristic. The measured and modeled input P1dB powers are 12.7 dBm and 15.1 dBm, respectively.

The performance of the RSOA based the RoF link can also be evaluate by another two figures of merit, in terms of Input 3rd-Order Intercept Point (IIP3) and Spurious Free Dynamic Range (SFDR) [54]. For this purpose, generally, two-tone signals are the most widely used. The two-tone signals were generated by VSG with carrier frequencies at 995 MHz and 1005 MHz. Fig. 2.8 presents the experimental and simulated results obtained for the output power of the fundamental and the 3rd-Order IMD (IMD3) products, as a function of the RF input powers. The IMD3 results are quite well

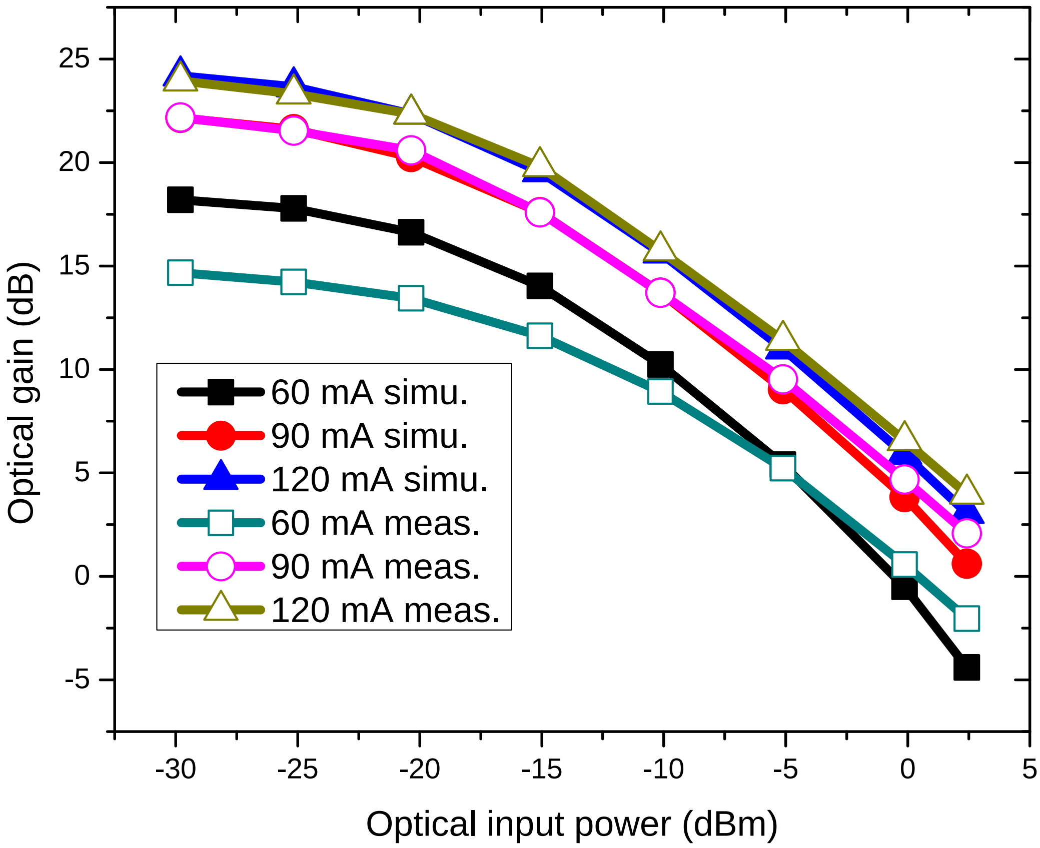

**Figure 2.6: Measured and simulated optical gain as a function of optical input power under the different biases of 60 mA, 90 mA, and 120 mA**

matched. The noise floor was -158.2 dBm/Hz at the bias current of 90 mA. The SFDR, which can be used to characterize the dynamic performance of the DUT, is determined by the fundamental, IMD3 and the noise floor. The SFDRs for measurement and simulation are 114.3 dB and 112.6 dB, respectively. The intersection between the linear approximations for the fundamental and the Intermodulation Distortion (IMD) curves for both measurement and simulation results in an IIP3. The IIP3 powers for measurement and simulation are 19.8 dBm and 20.9 dBm, respectively.

### 2.3.3 Transmission Performance

Error Vector Magnitude (EVM) is a common figure of merit for evaluating the quality of digitally modulated signals. The EVM defines the difference between the ideal reference symbol and the

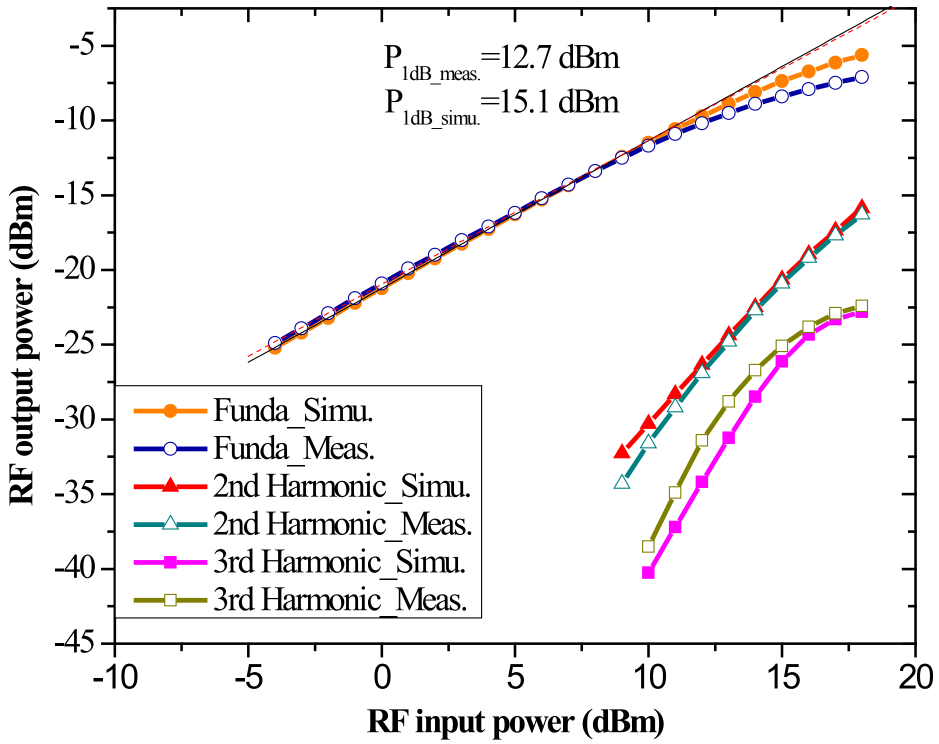

Figure 2.7: Measured and modeled fundamental and harmonic distortions under one-tone test with frequency of 1 GHz.

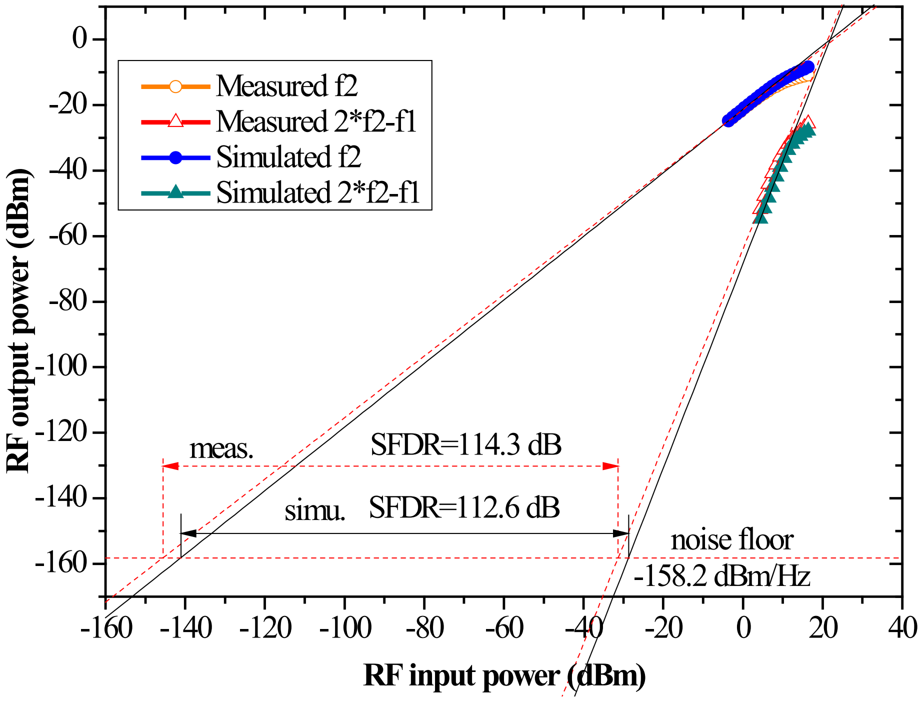

Figure 2.8: Measured and simulated fundamental and IMD3 distortions under two-tone test with frequencies of 995 MHz and 1005 MHz.

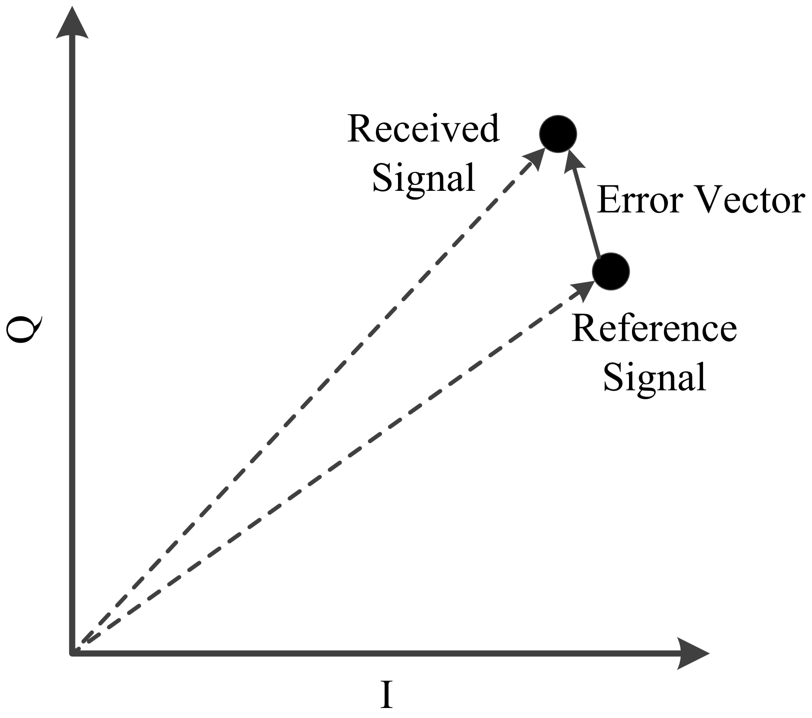

**Figure 2.9: Illustration of EVM.**

received symbols, as illustrated in Fig. 2.9. The Root Mean Square (RMS) EVM can be employed by the following equation

$$rmsEVM = \sqrt{\frac{\frac{1}{N}\sum_{n=1}^{N}|s(n)-r(n)|^2}{\frac{1}{N}\sum_{n=1}^{N}|r(n)|^2}} \times 100\% \tag{2.16}$$

where $r(n)$ is the reference transmitted symbol, $s(n)$ is the measured or modeled output symbol, $N$ is the number of symbols.

To simulate the transmission performance of the proposed physical model with Orthogonal Frequency Division Multiplexing (OFDM) signal, a simulation setup is shown in Fig. 2.10. A Wireless Local Area Network (WLAN) signal source generates the desired signal. Two components named "AddNDensity" are added to simulate the noise floors of the RoF link and spectrum analyzer.

An IEEE 802.11g signal at frequency of 1 GHz was generated in the VSG and used as the input signal, which is a 54 Mbit/s OFDM signal with 64-ary Quadrature Amplitude Modulation (64QAM) modulation and 52 active subcarriers. Fig. 2.11 is a comparison of measured and simulated RMS EVMs under different optical input powers of -5 dBm, -10 dBm and -15 dBm and bias currents of 60

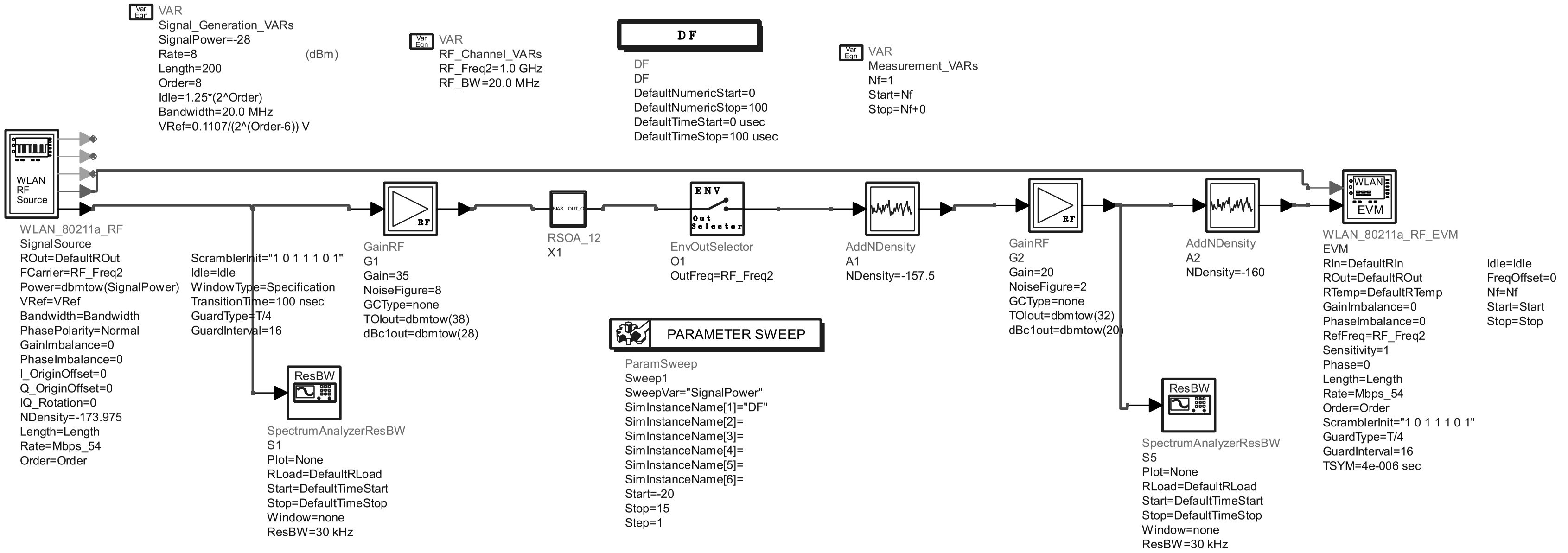

Figure 2.10: Simulation diagram of the transmission performance by using ADS.

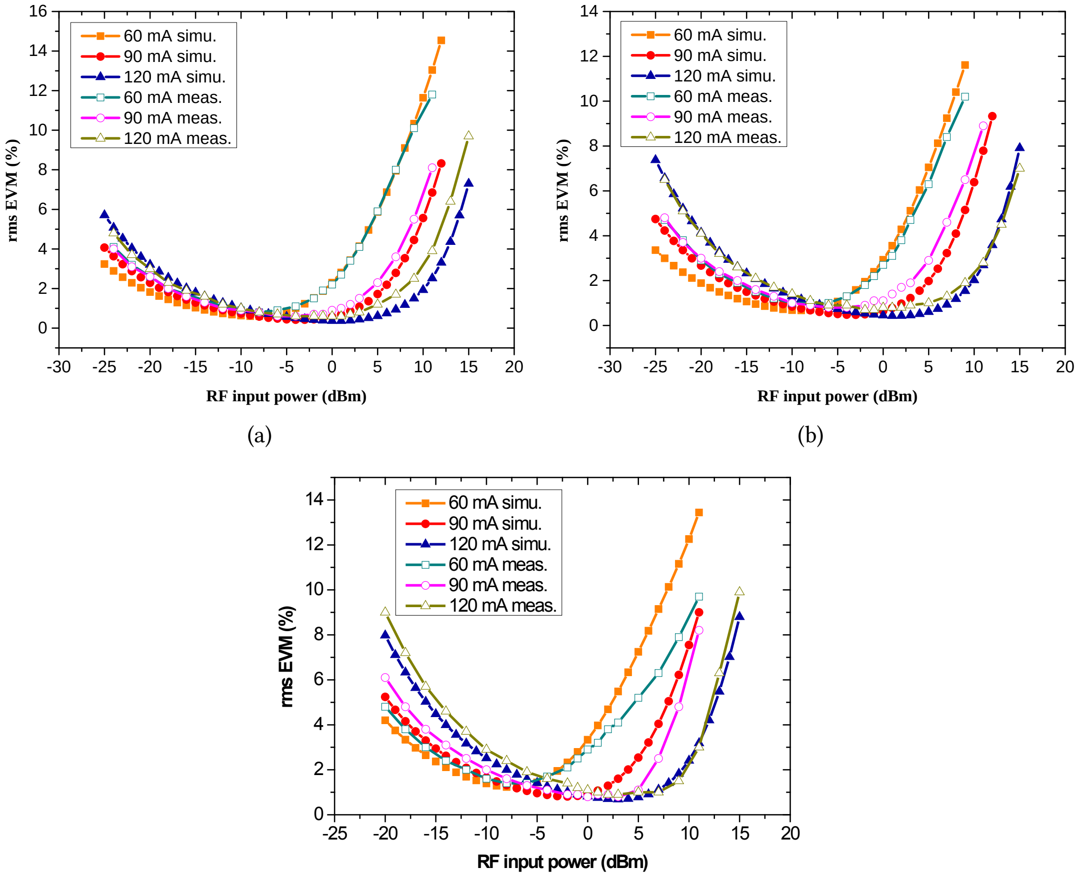

(a)

(b)

(c)

**Figure 2.11: Measured and simulated EVMs versus RF input powers under the different optical inputs (a) at -5 dBm, (b) at -10 dBm, (c) at -15 dBm.**

mA, 90 mA and 120 mA. The figures show "U" curves. The transmission performance is limited for low powers by the noise, and for high powers by the nonlinearity of the RSOA modulator. At low RF input power the EVMs are worse at 120 mA than one at 60 mA. The reason is that a stronger ASE noise is generated at higher bias current.

## 2.4 Distribution of Carrier Density and Photon Density

In this section, the model is used to simulate the spatial distributions of the carrier and photon. Fundamentally, spatial distributions of the carrier density and photon density of the RSOA modulator are functions of the position $z$ along the active layer length, input optical power and bias current due to the propagation of the optical wave along the device and the interaction between carriers and photons. Analysis of these spatial distributions can be used to aid the design and optimization of the RSOA.

Fig. 2.12 shows that the effect of increasing the bias current is to increase the RSOA carrier density, signal and ASE photon densities. This is mainly because of the increase of the concentration of the injected electrons into the active region with the bias current increasing. The signal photon density increases with increasing the optical input power. The ASE photon density decreases when the optical input power increased. Unlike SOA [29,75], the carrier density at low optical input power is asymmetrical due to the high reflection of the rear facet of the RSOA. For the low optical input power the ASE noise dominates the signal power.

## 2.5 Link Gain Improvement

As mentioned earlier, the model can be used to aid design and optimization of the RSOA. One of main limits of the RSOA modulator is the low link gain when compared with DFB laser modulator. In this section, we address two-electrode schematics [76, 77] to improve the link gain of the RSOA modulator in the RoF links.

We split the electrode of the RSOA modulator into two parts, one for the bias current and RF signal injection and the other only for the bias current injection. Therefore, there are two kinds of modulation schematics as depicted in Fig. 2.13:

- Case I: input&output modulation configuration.
- Case II: mirror modulation configuration.

In Case I, the RF modulating signal is injected at the input and output side of the RSOA as shown in Fig. 2.13(a), and in Case II, the RF modulating signal is injected at the mirror side of the RSOA as shown in Fig. 2.13(b). We define $I_{RF}$ as the bias current at the section where the RF signal is also injected and $I_{DC}$ as only bias current injection at the section.

A RF signal with a single carrier frequency of 1 GHz is used to demonstrate the effect of the bias configuration on the link gain. The link gains under different bias current configuration for Case I and Case II are shown in Fig. 2.14 and Fig. 2.15, respectively. To be compared, the link gain for a single electrode configuration is also depicted. From both figures we can see clearly that the link gain degrades when the low bias current is configured at the input&output side. This is because the lower injected current density causes lower carrier to be recombined, however, higher photon density is

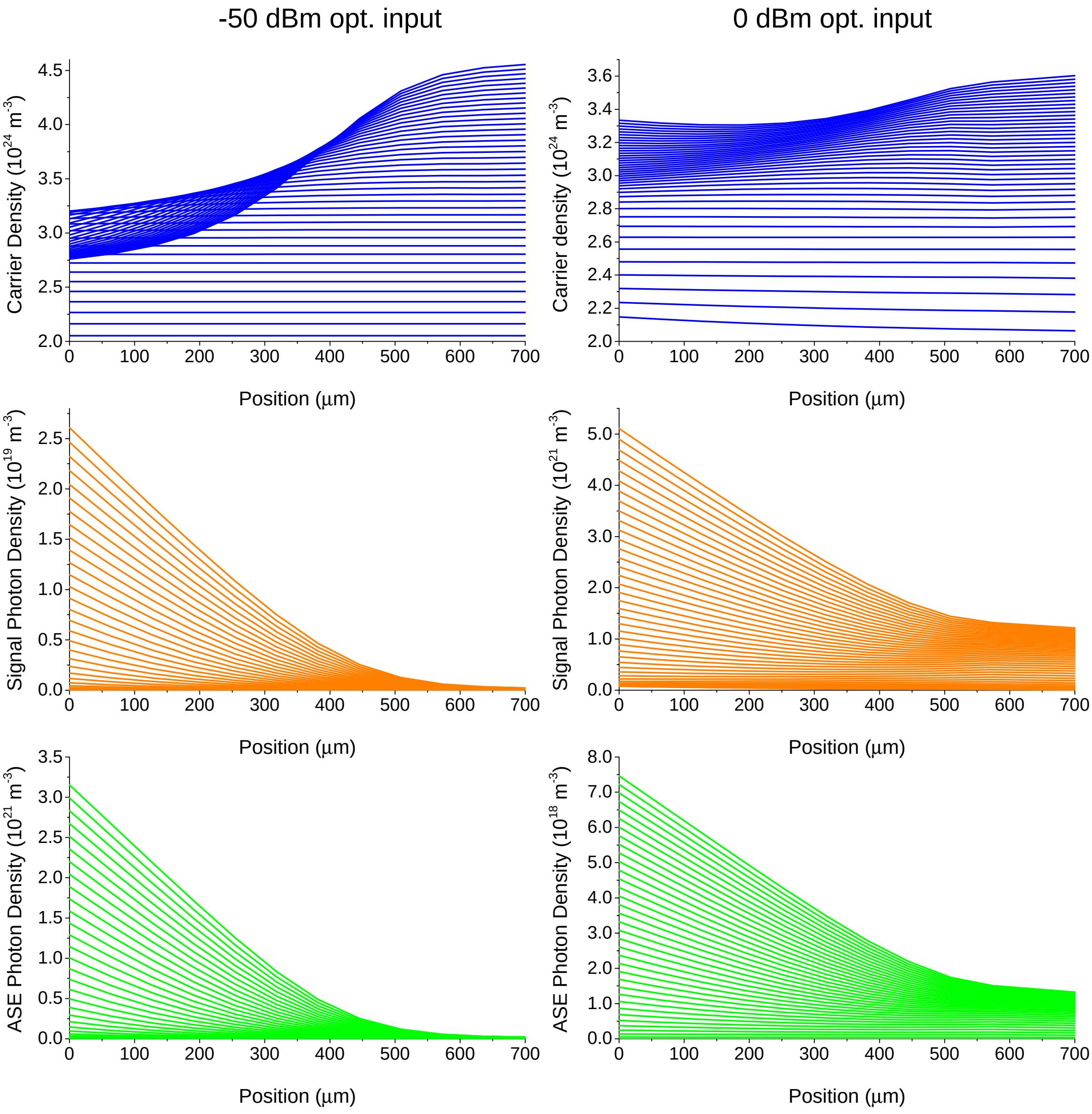

**Figure 2.12: Spatial distribution of carrier density, signal photon density and ASE photon density as a function of position along the length of the active region at the input optical powers of -50 dBm (left)and 0 dBm (right). The bias currents range from 20 mA to 100 mA.**

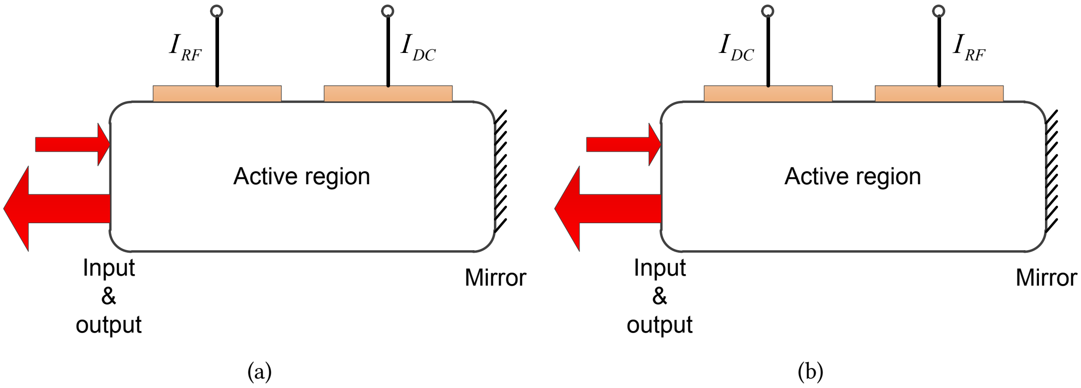

**Figure 2.13: Schematic diagram of two electrodes: (a) Case I: input&output modulation, (b) Case II: mirror modulation.**

necessary at the input&output side as shown in Fig. 2.12. Therefore the higher bias current should be injected at the input&output side. Fig. 2.15 shows that the link gain can be improved up to 6 dB under the $I_{DC}$ and $I_{RF}$ of 70 mA and 20 mA, respectively for case II since the RF signal is injected at the mirror side and can be amplified along the active region. Note that the higher link gain means the lower input P1dB power. Therefore, a tradeoff should be made in real applications.

## 2.6 Summary

In this chapter, based on the rate equation and traveling wave equations, a simple time domain physical model for a bulk RSOA modulator used in the RoF links has been proposed and validated.

The physical parameters defined in the model were extracted with fitting the measurement data with the optimization tool in ADS. Good agreement is achieved between measurement and simulation. The static and dynamic characteristics of the RSOA modulator have been demonstrated. The transmission performance between measurement and simulation are evaluated with 54 Mbit/s OFDM signal with 64QAM modulation and 52 active subcarriers. The distribution of carrier and photon densities gives us an overview how they distribute in the active region of the device. It can aid the design and optimization of the RSOA. The link gain in the RoF can be improved up to 6 dB by using multi-electrode configuration for case II.

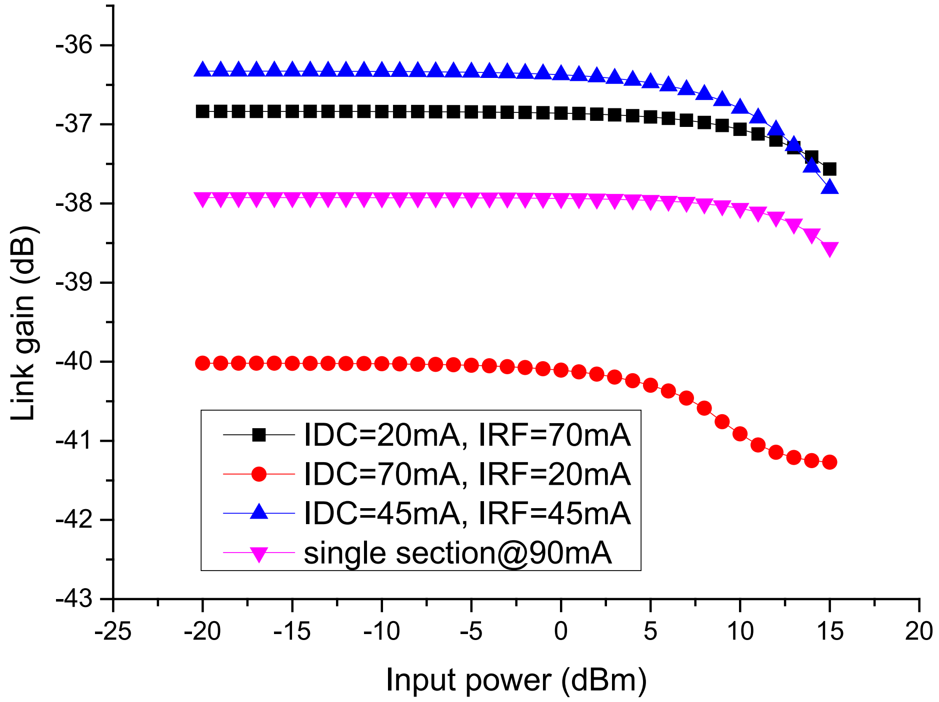

Figure 2.14: Link gain versus RF input power under different bias configuration for input-output modulation schematic (Case I).

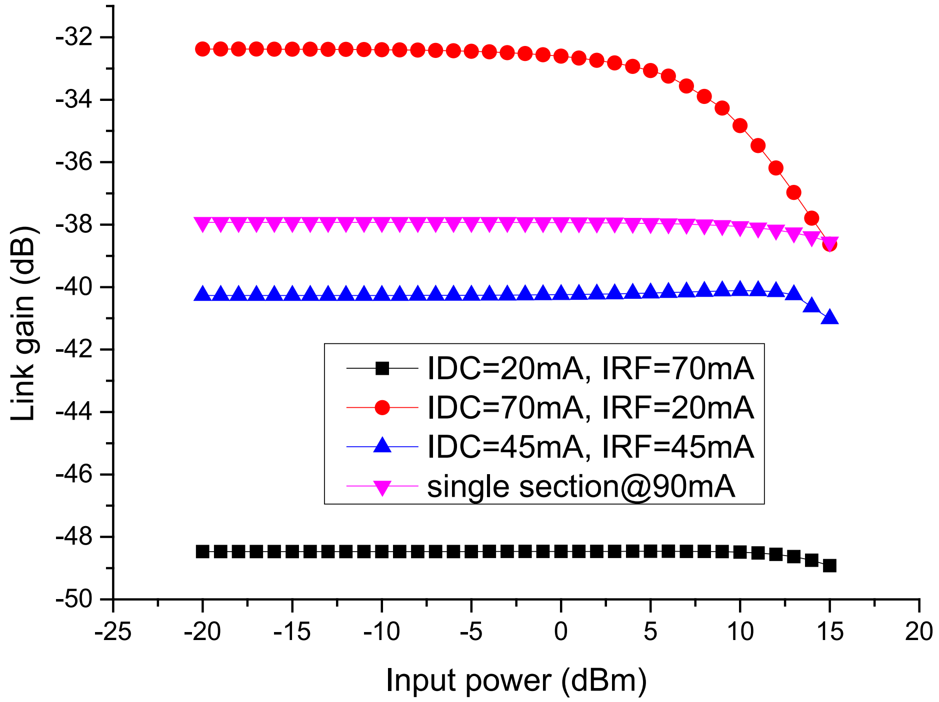

Figure 2.15: Link gain versus RF input power under different bias configuration for mirror modulation schematic (Case II).

# Chapter 3

# Behavioral Modeling and Simulation of RSOA

*This chapter discusses the behavioral modeling of the RSOA modulator. Three popular methods of the behavioral modeling such as ANN, memory polynomial and X-parameters are presented and compared. The dynamic AM-AM and AM-PM characteristics of the RSOA modulator are demonstrated for the memory polynomial and ANN based models. Harmonic distortion and intermodulation distortion are considered for the X-parameters based model from another point of view.*

## 3.1 Introduction

As discussed in chapter 2, the physical model is mainly derived from the rate equation and traveling-wave equations. However, many of the physical parameters are often unknown and difficult to be measured. In contrast, The key advantage of the behavioral modeling is that it does not require deep knowledge of the RSOA physics and functionality. A behavioral modeling technique offers a system method by which the composite effect of nonlinearity of the RSOA modulator can be modeled by relating the input/output characteristics of the RSOA modulator.

As mentioned earlier, the behavioral approach does not require the prior knowledge of the devices. Its coefficients rely only on the input and output measurement signals of the DUT. The performance of behavioral modeling is influenced by two key aspects, the observation and the formulation. The observation refers to the accurate acquisition of the signals at the input and output of the DUT while exciting the appropriate behavior. The formulation corresponds to the choice of a suitable mathematical relation that describes all the significant interaction between the DUT's input and output signals.

As stated in chapter 1, Volterra series is the most comprehensive modeling method for dynamic nonlinear devices and systems. It has been used for modeling and predistortion of RF power amplifiers [48, 62] and lasers [41]. However, the identification process of its parameters, also called Volterra kernels, is very complex and the number of parameters increases drastically with the nonlinearity order and the memory depth. To reduce the complexity of the Volterra series, a memory polynomial model has been proposed [51]. It corresponds to a truncation of the Volterra series, in which only diagonal terms in the Volterra kernels are kept. Thus, the number of parameters is significantly reduced when compared to the conventional Volterra series. A variation of the memory polynomial model has been proposed by introducing the cross-terms referred to as the Generalized Memory Polynomial (GMP) [61].

Under large-signal drive conditions, nonlinear devices distort waveforms (in time domain) or generate harmonics, intermodulation and spectral regrowth (in frequency domain). Recently, the X-parameter model has been announced as a large signal modeling method, where the model can be extracted directly from data measured using a Nonlinear Vector Network Analyzer (NVNA) or from circuit level design. Then the extracted X-parameters can be loaded into ADS and simulated with circuit simulator. Verspecht and Root [2] first proposed a Polyharmonic Distortion (PHD) modeling. The PHD model is identified from the responses of a DUT stimulated by a set of harmonically related discrete tones, where the fundamental tone is dominant and the harmonically related tones are relatively small. The basic idea is that the PHD modeling approach can be used as a natural extension of S-parameters under large-signal conditions. The X-parameters are based on the PHD modeling [2, 3, 78].

This chapter will focus on the behavioral modeling based on ANN (see section 3.2), memory polynomial (see section 3.3) and X-parameters (addressed in section 3.4) for the RSOA modulator in the RoF uplink. Before addressing modeling a parameter extraction, signal pre-processing (time alignment) and evaluation of model accuracy are introduced.

### 3.1.1 Parameter Extraction Procedure

The main parameter extraction procedure is illustrated in Fig. 3.1. The complex data streams are first captured from the input and output of the RSOA modulator. The gathered signals need to be aligned first before being used to identify the behavioral model. The details of time alignment algorithm will be addressed in Section 3.1.3. After time alignment and preprocessing, the data can finally be used to extract the parameter of the behavioral model.

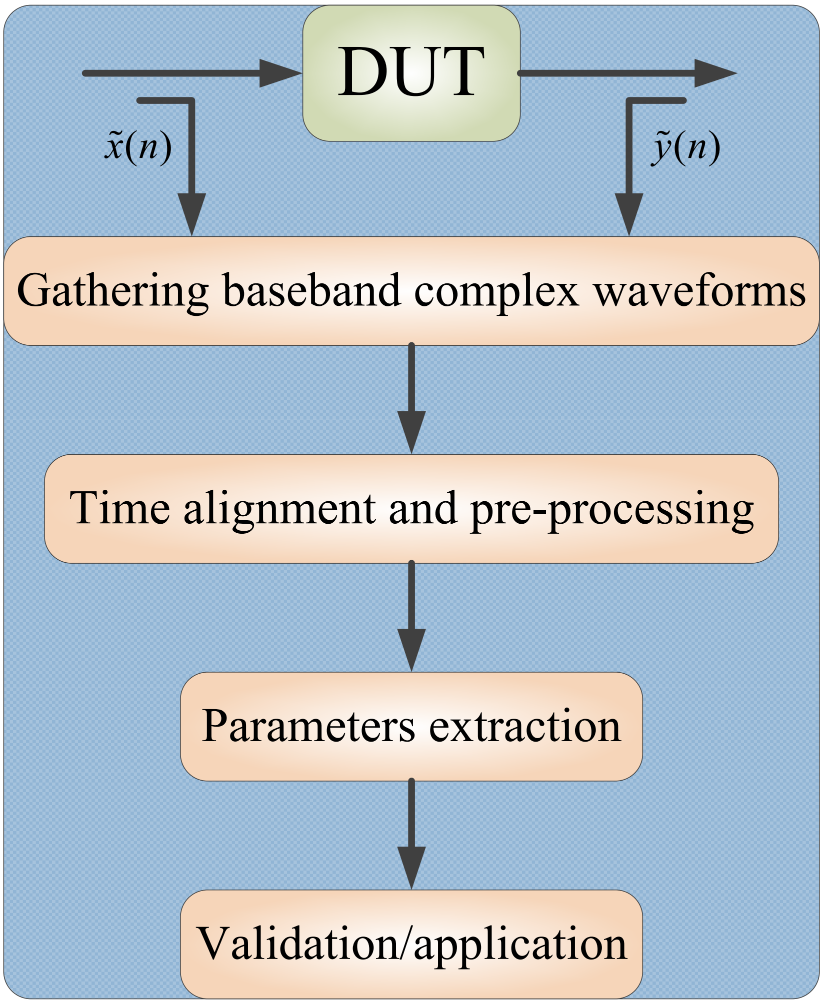

**Figure 3.1: Behavioral model parameter extraction procedure: main steps from measurements to model validation.**

### 3.1.2 Experimental Setup

In order to capture the input and output complex envelope signals of the DUT the experimental test bench is presented in Fig. 3.2. The test baseband signals were designed in MATLAB and fed into a VSG to be up-converted to RF domain with a carrier frequency of 1 GHz. A commercial AMP, ZHL-42W, was used to drive the DUT. The input and output of the DUT are down-converted and sampled by a VSA. This was realized by a switch. For instance, the direct connection between the output of the AMP and VSA enables us to obtain the measurements of the input signals for the

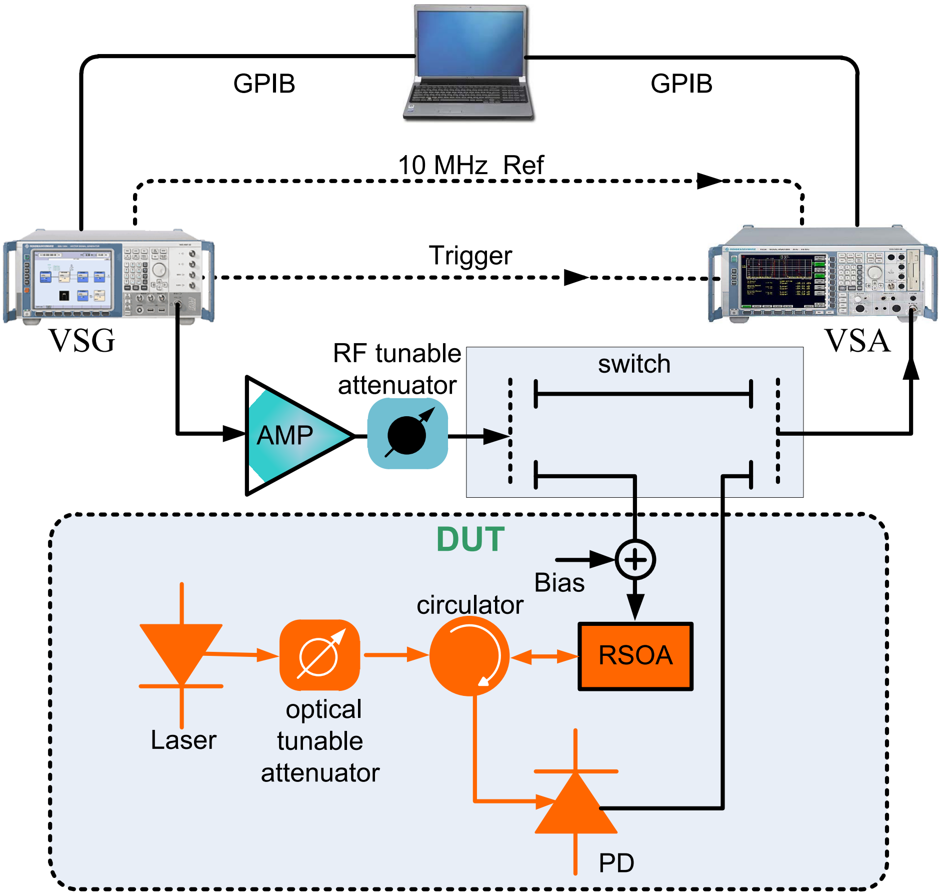

Figure 3.2: Experimental setup.

DUT. The VSG and VSA were connected to a computer controller using General Purpose Interface Bus (GPIB) cables. A 10 MHz reference and trigger signals between the VSG and VSA were used in order to synchronize and trigger multi measurement events. Any error in the generation acquisition synchronization could lead to poor repeatability of measurements.

### 3.1.3 Time Alignment and Compensation

The time delay between the measured input and output baseband complex signals of the DUT has to be accurately estimated in order to align the input and output signals prior to identifying the behavioral model. Clearly, any time delay mismatch between these two signals will impact the performance of the behavioral model [79].

A time alignment algorithm has been presented in [40]. The integer time delay between the input and output baseband complex signals is first estimated by conventional cross correlation method. Then sinc interpolation is applied to estimate the fractional time delay in order to further improve the distortion resulting from the time mismatch. The conventional cross correlation is depicted by

$$R_{\tilde{x},\tilde{y}}(d_{\text{int}}) = \begin{cases} \sum\limits_{k=0}^{K-d_{\text{int}}-1} [\tilde{x}(k+d_{\text{int}}) - \bar{x}][\tilde{y}^*(k) - \bar{y}^*], & \text{for } d_{\text{int}} \geq 0 \\ R^*_{\tilde{y},\tilde{x}}(-d_{\text{int}}), & \text{for } d_{\text{int}} < 0 \end{cases} \tag{3.1}$$

where $(\cdot)^*$ is the complex conjugate operator. $\bar{x}$ and $\bar{y}^*$ are the mean values of the waveform $x$ and the conjugate of $y$, respectively.

The integer time delay can be estimated by

$$d_{\text{int}} = \max_{d_{\text{int}}} \left\{ R_{\tilde{x},\tilde{y}} \left( d_{\text{int}} \right) \right\} \tag{3.2}$$

In time domain, the reconstruction of the continuous-time signal from the discrete-time signal can be considered as an interpolation process. After the integer time delay removed, the sinc interpolation is then used to estimate the fractional time delay $d_{frac}$. The sinc interpolation is given by

$$\begin{aligned} \tilde{x}_r(t) &= \sum_{k=-\infty}^{\infty} \tilde{x}(kT)\text{sinc}\left(\frac{t-kT}{T}\right) \\ &= \sum_{k=-\infty}^{\infty} \tilde{x}(kT)\frac{\sin\left(\frac{\pi\left(t-kT\right)}{T}\right)}{\frac{\pi\left(t-kT\right)}{T}} \end{aligned} \tag{3.3}$$

The reconstruction of the output signal $\tilde{y}_r(t)$ can be done using the similar process. Then the reconstructed $\tilde{x}_r(t)$ and $\tilde{x}_r(t)$ are resampled and used to calculate the discrete-time cross-correlation function $R_{\tilde{x}_r,\tilde{y}_r}(d_{frac})$.

The fractional time delay is estimated by

$$d_{\text{frac}} = \max_{d_{\text{frac}}} \left\{ R_{\tilde{x}_r,\tilde{y}_r} \left( d_{\text{frac}} \right) \right\} \tag{3.4}$$

After the integer time delay and fractional time delay removed, the data can finally be used for further process.

### 3.1.4 Model Accuracy Evaluation

The behavioral model operates on baseband time domain waveforms. In order to assess the performance of the model, two assessments, termed Normalized Mean Square Error (NMSE) criterion in the time domain and RMS EVM given in Equation (2.16), can be employed. The NMSE verification metric is the total power of the error vector between the measured and modeled waveforms, normalized to the measured signal power, depicted explicitly by

$$NMSE = 10\log_{10}\left\{\frac{\sum_{n=1}^{N}\left([y_I^{meas}(n) - y_I^{model}(n)]^2 + [y_Q^{meas}(n) - y_Q^{model}(n)]^2\right)}{\sum_{n=1}^{N}\left([y_I^{meas}(n)]^2 + [y_Q^{meas}(n)]^2\right)}\right\} \tag{3.5}$$

where $y_I^{meas}$, $y_Q^{meas}$, $y_I^{model}$ and $y_Q^{model}$ are the in-phase and quadrature components of measured and modeled output waveforms, respectively.

## 3.2 TDMLP

In this section, we focus on the modeling of the RSOA modulator with ANN. ANN based behavioral models have been widely used to model RF power amplifiers [80, 81], EDFA [42] and QD-SOA [44] because of its generality and accuracy. In [44], the pulse amplification and FWM characteristics of the QD-SOA has been investigated by using a Multilayer Perceptron (MLP) model.

### 3.2.1 TDMLP Model

Schematic representation of a single hidden layer TDMLP based model is shown in Fig. 3.3. To account for the memory effects, a set of neurons can be added in the input layer. The transformation from the input layer to the hidden layer is nonlinear, while the transformation from the hidden layer to the output layer is pure linear. $b_{h,j}$ ($j = 1, 2, ..., M$) are the biases in the hidden layer. $f(\cdot)$ is the activation function in the hidden layer, which will be introduced in Section 3.2.3. $b_{o,k}$ ($k = 1, 2$ in our case) are the biases in the output layer.

The output $u_j(n)$ of the *j*th node in the hidden layer is depicted by

$$u_j(n) = f(\sum_{i=0}^{m} \omega_{i,j}x(n-i) + b_{h,j}) \tag{3.6}$$

where the $\omega_{i,j}$ is the weighting coefficient from the *i*th node in the input layer to the *j*th node in the hidden layer. The $x$ can be $x_I$ or $x_Q$.

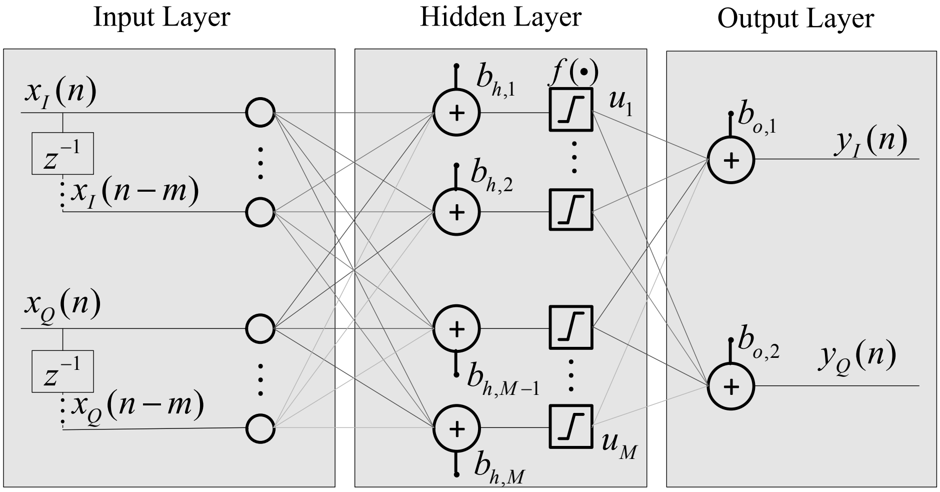

**Figure 3.3: TDMLP based model with $2 \times (m+1)$ input nodes, $m$ is the number of memory depth, $z^{-1}$ is for unit delay operation, $M$ hidden nodes and two output nodes.**

The output of the *k*th node in the output layer is given by

$$y_k(n) = \sum_{j=1}^{M} \omega_{j,k} u_j(n) + b_{o,k} \tag{3.7}$$

where the $\omega_{j,k}$ is the weighting coefficient from the *j*th node in the hidden layer to the *k*th node in the output layer. $y_k$ is $y_I$ or $y_Q$ in our case.

All of the weighting coefficients $\omega_{i,j}$, $\omega_{j,k}$ and bias parameters $b_{h,j}$, $b_{o,k}$ need to be determined during the training phase. One of the most critical issues in constructing the ANN is to determine the number of hidden layers and the number of neurons in hidden layers. The number of the hidden layer can be increased if needed. The mathematical results, however, have been shown that the single hidden layer MLP is capable of approximating uniformly any continuous multivariate function to any desired degree of accuracy [82]. This implies that any failure of a function mapping must arise from inadequate choice of parameters or an insufficient number of hidden nodes. More than one hidden layer is often used to reduce the number of total nodes in hidden layers.

### 3.2.2 Overfitting

It is difficult to determine the optimal number of hidden nodes. The large number of nodes in the hidden layer makes the poor generality of the TDMLP as the nets with too much capacity overfit the training data [83]. In order to avoid overfitting during the training phase, it is necessary to use additional techniques such as regularization, early stopping, or cross-validation [84]. The cross-validation is the most popular method to achieve generalization by evaluating the performance of the model on a different set of data from ones for training [81].

### 3.2.3 Activation Function

The effects toward obtaining the best performance of the ANN based model also need to focus on the neuronal activation scheme. Different choices of the activation functions result in different network models. In general, the activation function in the hidden layer is a nonlinear function. The anti-symmetric functions often yield faster convergence. The most common choice of the activation function in the hidden layer is the anti-symmetric hyperbolic tangent, which is differentiable everywhere and mathematically described as:

$$f(x) = \tanh(x) = \frac{e^x - e^{-x}}{e^x + e^{-x}} \tag{3.8}$$

### 3.2.4 Back Propagation Learning Algorithm (BPLA)

BPLA is a popular method of training ANN, especially training MPL nets. The traditional BPLA, however, converges very slowly when compared with second-order algorithms. The Levenberg-Marquardt (LM) method was designed to utilize the advanced and complex second-order optimization algorithm to achieve significant advances in training speed and accuracy [85]. The LM back propagation algorithm is the fastest method for training feed-forward neural networks. It has been implemented in the MATLAB ANN toolbox. In order to obtain the optimal weight and bias parameters, one will minimize the average error function, which is represented as [84], [85]

$$V(\omega) = \frac{1}{2P}\sum_{p=1}^{P}\sum_{i=1}^{N}\left[t_i^p(\omega) - y_i^p(\omega)\right]^2 = \frac{1}{2P}\sum_{p=1}^{P}\sum_{i=1}^{N}\left[e_i^p(\omega)\right]^2 \tag{3.9}$$

where $P$ is the number of training patterns. $N$ is the number of the output nodes ($N$ is equal to 2 in our model). $t$ is the target output and $y$ is the model output. $e$ is the network errors. $\omega$ is the parameters such as weights and biases to be extracted. In our case, $t$ and $y$ choose the corresponding in-phase parts and quadrature parts when $i$ is equal to 1 and 2, respectively.

For the LM algorithm, the weight and bias parameters are updated by [85]

$$\boldsymbol{\omega}_{n+1} = \boldsymbol{\omega}_n - \left[\mathbf{J}^T\mathbf{J} + \mu\mathbf{I}\right]^{-1}\mathbf{J}^T\mathbf{e} \tag{3.10}$$

where $(\cdot)^T$ denotes the transpose operation. $n$ is the number of iteration. $\boldsymbol{\omega}$ denotes the vector of all training parameters (weights and biases). $\mathbf{J}$ is the Jacobian matrix that contains first derivatives of the net errors with respect to the weights and biases. $\mathbf{e}$ is the vector of the network errors. $\mathbf{I}$ is the identity matrix and $\mu$ is the learning parameter.

### 3.2.5 TDMLP Training

The training of the TDMLP involves choosing a set of weights and biases to optimize the accuracy of the mapping. The TDMLP based model can be easily trained by the BPLA in MATLAB. In order to train the TDMLP, a random 64QAM signal with the symbol rate of 20 Msymbol/s, which were filtered with a Square Root Raised Cosine (SRRC) filter with the roll-off factor of $\alpha = 0.22$, were created at baseband in MATLAB. The 64QAM signal creates a Peak-to-Average Power Ratio (PAPR) of around 7.1 dB. The signal with a sampling rate at 80 MHz was fed into the VSG memory to be up-converted to the RF band at 1 GHz and finally to be passed through the DUT. In our case the average RF input power of the DUT was set up to 13 dBm, which is near the input 1 dB compression point of the RSOA modulator. as mentioned earlier, the complex baseband (complex envelope) input and output signals of the DUT were captured from the VSA. After time alignment and preprocessing, around 40 000 samples were captured to train, validate and test the TDMLP model. Using the cross-validation technique, the training, validation and testing of the TDMLP were carried out using different segments of the measured input and output signals. The first 10 000 samples were used for training the nets. The second 20 000 samples, which were different with ones for training, were used to validate the model. The remaining 10 000 different samples were used for testing of the capacity of the model to predict the output of the RSOA modulator.

Table 3.1 shows the performance of the TDMLP model as a function of the memory depth and the number of nodes in the hidden layer. Based on Table 3.1, the higher memory depth and larger number of hidden nodes do not imply the better performance. The performance of the TDMLP model increases with the number of hidden nodes increasing. By further increasing the hidden nodes, however, the performance starts to degrade due to overfitting the training data set, which reduces the generality of the TDMLP. This issue can be solved by increasing the training data set.

**Table 3.1: TDMLP model performance versus memory depth and the number of hidden nodes.**

| NMSE (dB) | | Number of nodes ($M$) | | | | | | |
|---|---|---|---|---|---|---|---|---|
| | | 5 | 10 | 15 | 20 | 25 | 30 | 35 |
| Memory depth ($m$) | 0 | -28.62 | -28.64 | -28.65 | -28.66 | -28.64 | -28.64 | -28.65 |
| | 1 | -30.49 | -36.8 | -37.03 | -37.08 | -37.08 | -37.09 | -37.11 |
| | 2 | -31.05 | -41.68 | -41.83 | -41.79 | -42.21 | -42.22 | -42.42 |
| | 3 | -41.96 | -43.01 | -43.73 | -44.33 | -44.31 | -43.46 | -44.12 |
| | 4 | -42.37 | -43.62 | -44.18 | -44.21 | -44.37 | -44.39 | -44.32 |
| | 5 | -41.56 | -44.13 | -44.24 | -43.88 | -44.38 | -44.36 | -44.29 |
| | 6 | -41.22 | -44.05 | -44.23 | -43.53 | -43.95 | -44.19 | -44.35 |

In our work we chose the hidden nodes of 20 and memory depth of 3 for following analysis even though there are several slightly better points but the more weighting coefficients are required.

### 3.2.6 TDMLP Validation

The training, validation and testing performance under the hidden nodes of 20 and memory depth of 3 is shown in Fig. 3.4. It is shown that the performance of the TDMLP model improves with increasing number of training epochs. The error on the validation and testing data sets starts off decreasing as the underfitting is reduced, but then it eventually begins to increase again as overfitting occurs. A solution to ensure the best generality of the TDMLP is to use the procedure of early stopping. One trains the network on the training data set until the performance on the validation data set starts to deteriorate and then stops the training phase. Therefore, the overfitting problem can be avoided by introducing validation step.

The time domain waveforms of in-phase and quadrature parts of the RSOA outputs are shown in Fig.3.5, where only first 250 samples are shown for clarity. They indicate that the measured data points are fitted by the modeled ones well.

When studying nonlinear distortion, it is important to observe the Power Spectral Density (PSD) which will demonstrate the spectral regrowth due to the nonlinearity of the RSOA modulator. It gives us an overview of the fitting between measurement and model in frequency domain. The measured and modeled PSDs are shown in Fig. 3.6. The spectral regrowth is clearly visible. A compensation strategy can be introduced, which will be addressed in chapter 4.

After demodulation process, the constellation for symbols of the transmitted, measured output and TDMLP model outputs are depicted in Fig. 3.7. Comparison of the EVM with the level of distor-

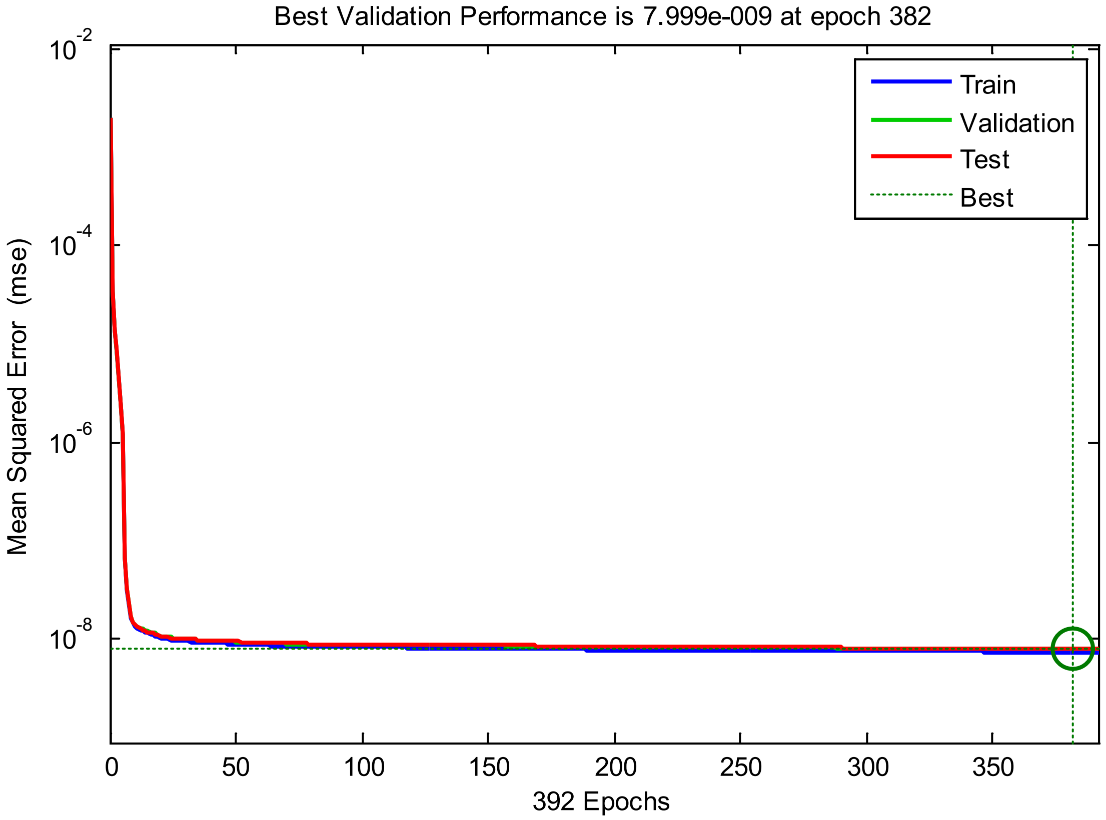

**Figure 3.4: The training performance of the TDMLP based model for the RSOA modulator with memory depth of 3 and hidden nodes of 20.**

tion of the constellation points caused by the RSOA would further help to show whether sufficient accuracy has been achieved. The EVMs for measured and modeled output symbols are 5.70% and 5.64%, respectively, calculating by the formula (see Equation (2.16)).

The nonlinear distortion and memory effect can be described by plotting the dynamic AM-AM and dynamic AM-PM characteristics as shown in Fig. 3.8. We can clearly see that the distortion including static nonlinearities and memory effects was induced by the RSOA modulator. It is also clearly shown that the TDMLP model can produce a similar scattering to ones exhibited by the measurement data since the memory effect is considered in the model. The TDMLP based model with memory can accurately predict the dynamic behaviors of the RSOA modulator. The AM-PM conversion graph appears to show large random phase at low input powers due to the effect of measurement noise. The small signal is more sensitive to the noise. Thus, the AM-PM curve is open at the low input power side. The phase changes are up to 7° at the high input power side.

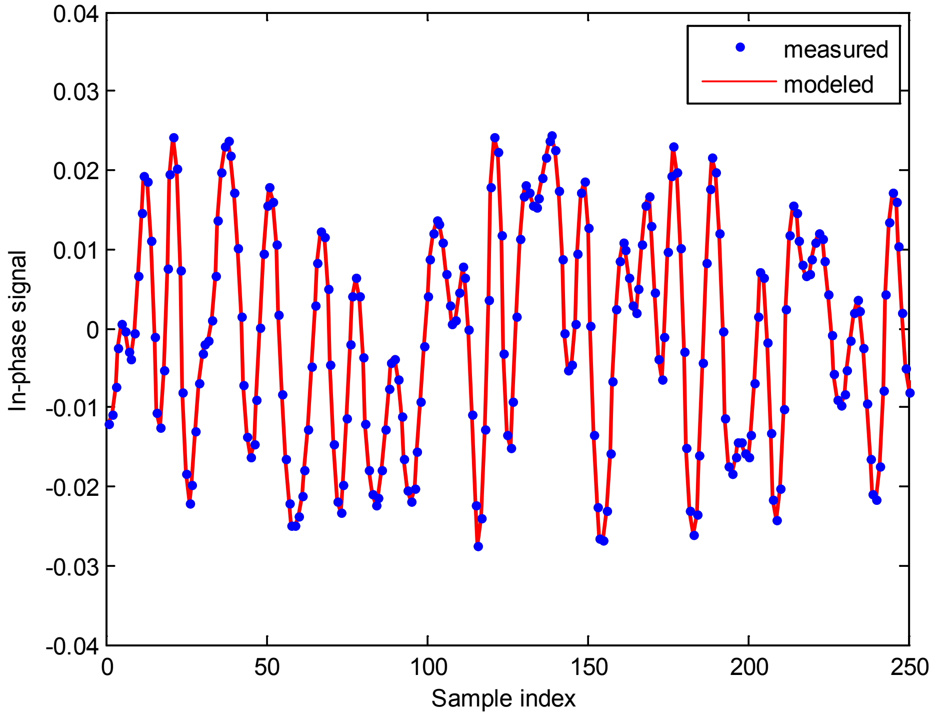

(a)

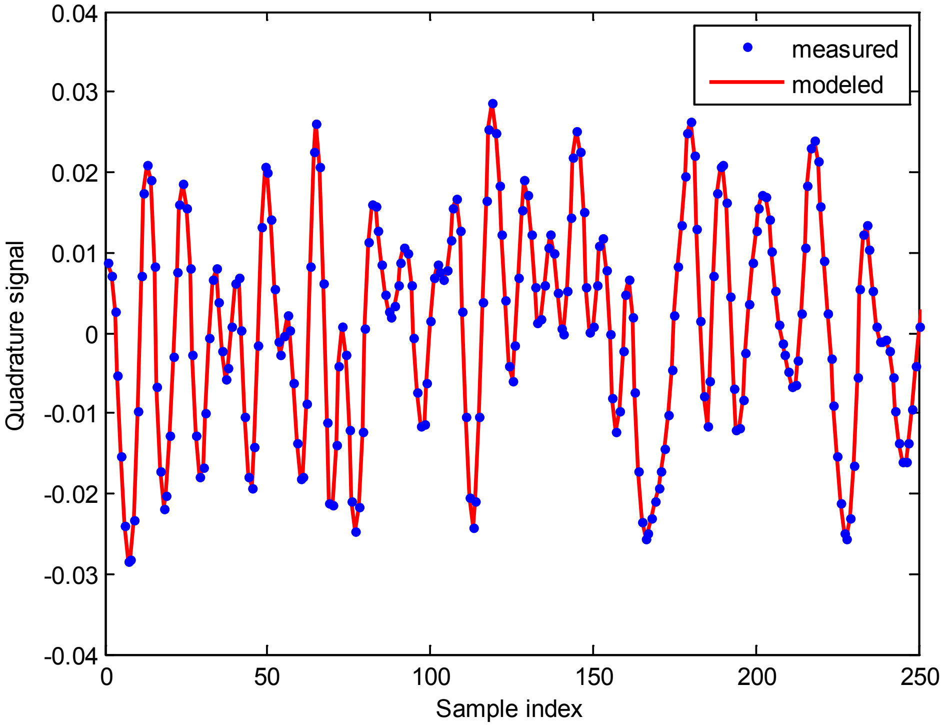

(b)

**Figure 3.5: Measured and modeled outputs in-phase (a) and quadrature (b) parts in time domain.**

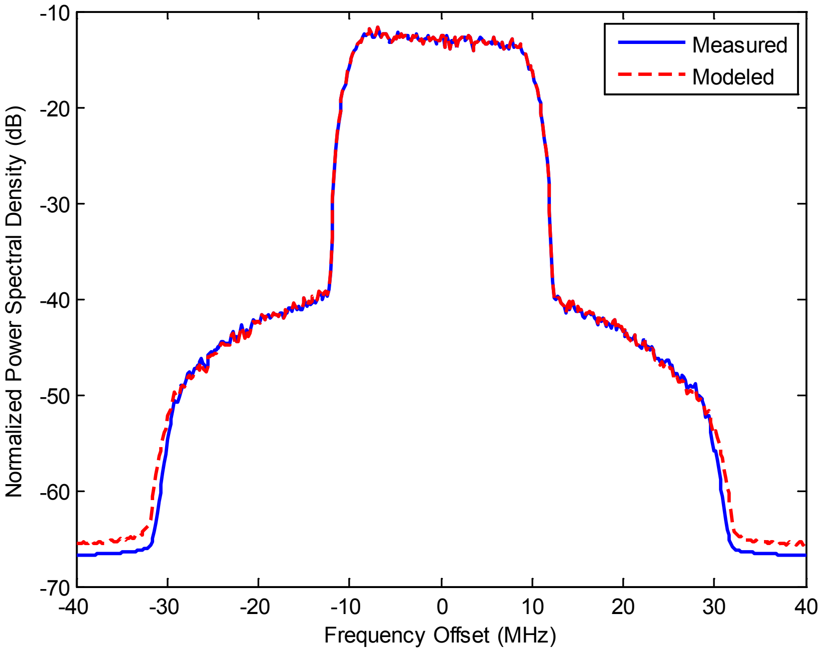

**Figure 3.6: Normalized power spectral density of measured and modeled outputs.**

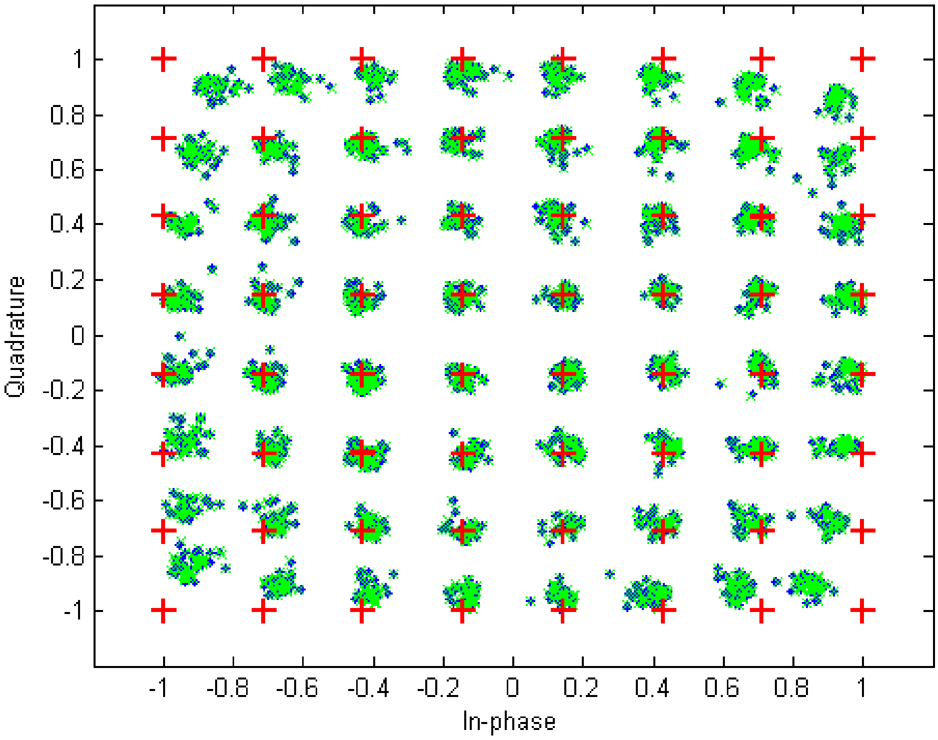

**Figure 3.7: Normalized constellation (red '+' for the transmitted symbol, blue '·' for the measured output, and green 'x' for the TDMLP model output).**

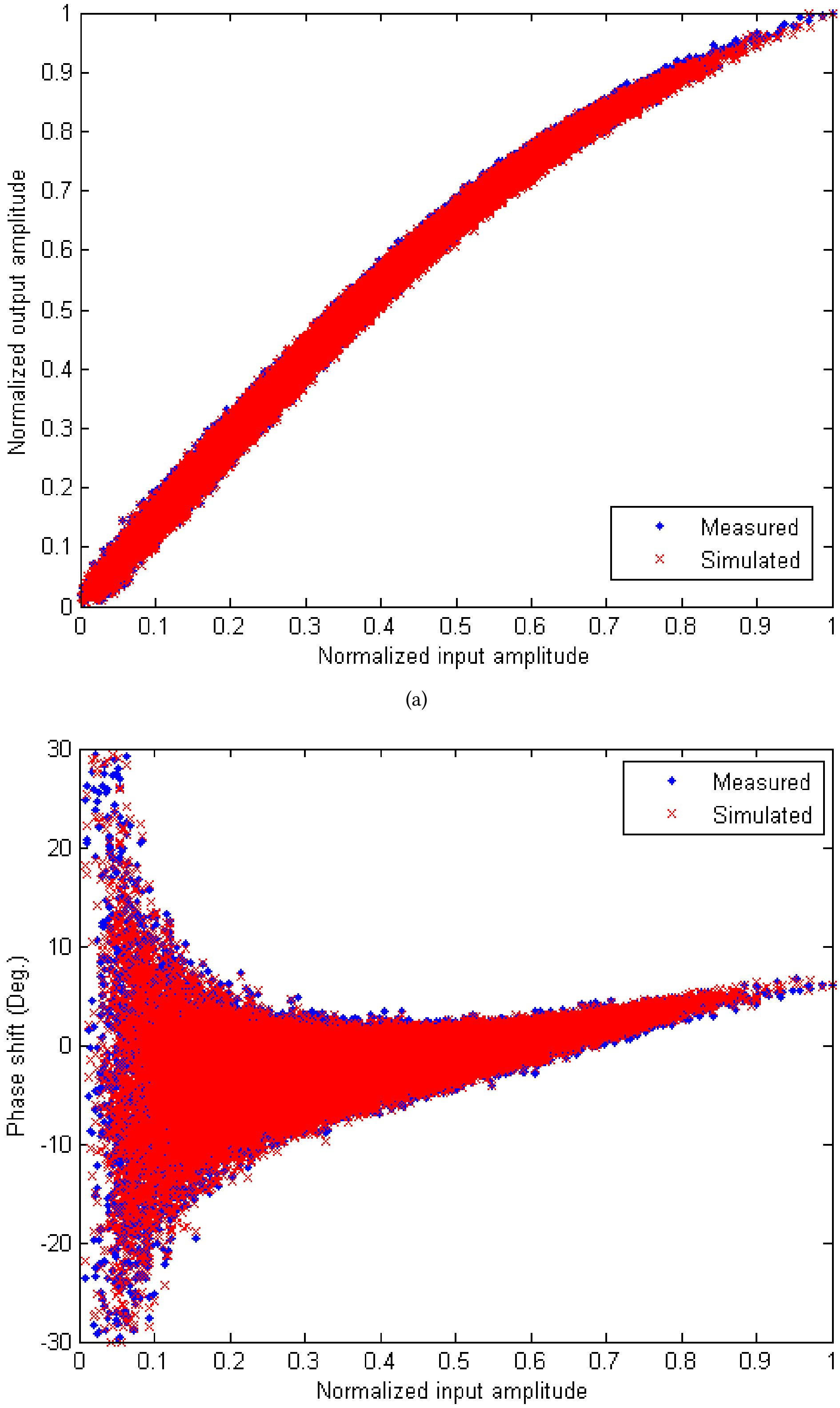

(a)

(b)

**Figure 3.8: Dynamic AM-AM (a) and AM-PM (b) characteristics of the RSOA modulator.**

## 3.3 GMP

As mentioned previously, the memory polynomial is one of the most popular methods to model the nonlinear devices [52,86] or to compensate the nonlinear distortion of the devices [50,51,61]. In this section we attempt to model the RSOA modulator by using the GMP.

### 3.3.1 GMP Based Modeling

The baseband GMP model [61] is described as follows

$$\begin{aligned}\tilde{y}(n) &= \sum_{k=1}^{K_a}\sum_{l=0}^{L_a-1} a_{kl}\tilde{x}\left(n-l\right)\left|\tilde{x}\left(n-l\right)\right|^{k-1} \\ &+ \sum_{k=1}^{K_b}\sum_{l=0}^{L_b-1}\sum_{m=1}^{M_b} b_{klm}\tilde{x}\left(n-l\right)\left|\tilde{x}\left(n-l-m\right)\right|^{k} \\ &+ \sum_{k=1}^{K_c}\sum_{l=0}^{L_c-1}\sum_{m=1}^{M_c} c_{klm}\tilde{x}\left(n-l\right)\left|\tilde{x}\left(n-l+m\right)\right|^{k}\end{aligned} \tag{3.11}$$

where $\tilde{x}$ and $\tilde{y}$ are the baseband input and output signals, respectively; $K_a$, $L_a$ are the number of coefficients for aligned signal and envelope, $K_b$, $L_b$ and $M_b$ are the number of coefficients for signal and lagging envelop, $K_c$, $L_c$ and $M_c$ are the number of coefficients for signal and leading envelope, $a_{kl}$, $b_{klm}$ and $c_{klm}$ are the corresponding polynomial coefficients.

The first term represents the conventional memory polynomial [51]. The second and third terms account for the effects of lagging and leading envelopes. A simple Least Square (LS) algorithm can be used for the parameter estimation of the GMP model as the output $\tilde{y}(n)$ of the model is linear with respect to its coefficients.

### 3.3.2 Extraction Methodology

As mentioned previously, the output of the GMP model is linear with respect to its coefficients. It enables us to extract the coefficients in a direct way by using measured input and output signals.

In particular, we can form a single parameter $P \times 1$ vector $\mathbf{h}$ containing all coefficients of the GMP model. $P = K_aL_a + K_bL_bM_b + K_cL_cM_c$. The $\mathbf{h}$ is depicted as follows

$$\mathbf{h} = \left[a_{10}\; a_{11}\; \cdots a_{K_a(L_a-1)}\; b_{101}\; b_{102}\; \cdots\; b_{K_b(L_b-1)M_b}\; c_{101}\; c_{102}\; \cdots c_{K_c(L_c-1)M_c}\right]^T \tag{3.12}$$

where $(\cdot)^T$ represents the transpose operator.

We define a $N \times P$ matrix $\mathbf{X}$ for all of the product terms of the sampled input signal appearing in the model. A $N \times 1$ vector $\mathbf{Y}$ is defined for the sampled output signal. Both are given in equation (3.13) and equation (3.14), respectively.

$$\mathbf{X} = \begin{bmatrix} \tilde{x}(0) & \cdots & \tilde{x}(-(L_a-1))|\tilde{x}(-(L_a-1))|^{K_a-1} & \tilde{x}(0)\,|\tilde{x}(-1)| & \cdots & \tilde{x}(-(L_b-1))|\tilde{x}(-(L_b-1)-M_b)|^{K_b} & \tilde{x}(0)\,|\tilde{x}(1)| & \cdots & \tilde{x}(-(L_c-1))|\tilde{x}(-(L_c-1)+M_c)|^{K_c} \\ \vdots & & \vdots & \vdots & & \vdots & \vdots & & \vdots \\ \tilde{x}(n) & \cdots & \tilde{x}(n-(L_a-1))|\tilde{x}(n-(L_a-1))|^{K_a-1} & \tilde{x}(n)\,|\tilde{x}(n-1)| & \cdots & \tilde{x}(n-(L_b-1))|\tilde{x}(n-(L_b-1)-M_b)|^{K_b} & \tilde{x}(n)\,|\tilde{x}(n+1)| & \cdots & \tilde{x}(n-(L_c-1))|\tilde{x}(n-(L_c-1)+M_c)|^{K_c} \\ \vdots & & \vdots & \vdots & & \vdots & \vdots & & \vdots \\ \tilde{x}(N-1) & \cdots & \tilde{x}(N-1-(L_a-1))|\tilde{x}(N-1-(L_a-1))|^{K_a-1} & \tilde{x}(N-1)\,|\tilde{x}(N-1-1)| & \cdots & \tilde{x}(N-1-(L_b-1))|\tilde{x}(N-1-(L_b-1)-M_b)|^{K_b} & \tilde{x}(N-1)\,|\tilde{x}(N-1+1)| & \cdots & \tilde{x}(N-1-(L_c-1))|\tilde{x}(N-1-(L_c-1)+M_c)|^{K_c} \end{bmatrix} \tag{3.13}$$

and

$$\mathbf{Y} = \begin{bmatrix} \tilde{y}(0) & \cdots & \tilde{y}(n) & \cdots & \tilde{y}(N-1) \end{bmatrix}^T \tag{3.14}$$

Therefore, the GMP model can be written as

$$\mathbf{Y} = \mathbf{X}\mathbf{h} + \mathbf{e} \tag{3.15}$$

where $\mathbf{e}$ is one $N \times 1$ error vector. The estimation error is written as

$$\mathbf{e} = \mathbf{Y} - \mathbf{X}\mathbf{h} \tag{3.16}$$

As mentioned earlier, the output of the model is linear with its coefficients. Therefore, the LS estimator that minimizes $\|\mathbf{e}\|^2$ is given as follows

$$\hat{\mathbf{h}} = \left(\mathbf{X}^H\mathbf{X}\right)^{-1}\mathbf{X}^H\mathbf{y} \tag{3.17}$$

where $(\cdot)^H$ represents the Hermitian transpose.

### 3.3.3 Validation and Results

An essential step in the development of any simulation model is validation. The measured samples are same with one we used in section 3.2. In this section, using cross validation technique, the 10 000 samples are used to extract the model coefficients. Another 10 000 samples from different segments of the measured baseband input and output signals are used for the model validation.

To demonstrate the effect of the memory depths and nonlinear orders in the model, we use the figure of merit, NMSE, to evaluate the performance of the GMP model. The performances of the model versus memory depths and nonlinear orders are shown in Table 3.2

Table 3.2 shows clearly that the performance of the model improves with the nonlinear orders and memory depths increasing. We can see that the contribution comes mainly from the first term in (3.11). For following analysis we use $K_a = 5$, $L_a = 6$, $K_b = 2$, $L_b = 3$, $M_b = 4$, $K_c = 2$, $L_c = 1$, and $M_c = 1$. Under this condition, the NMSE is -46.02 dB.

The measured and modeled in-phase and quadrature waveforms versus sample index are shown in Fig. 3.9. Only first 250 samples are shown for clarity. The real and imaginary components for measurement and simulation match very well. An overview in frequency domain is plotted with the PSD of the measured and modeled data in Fig. 3.10.

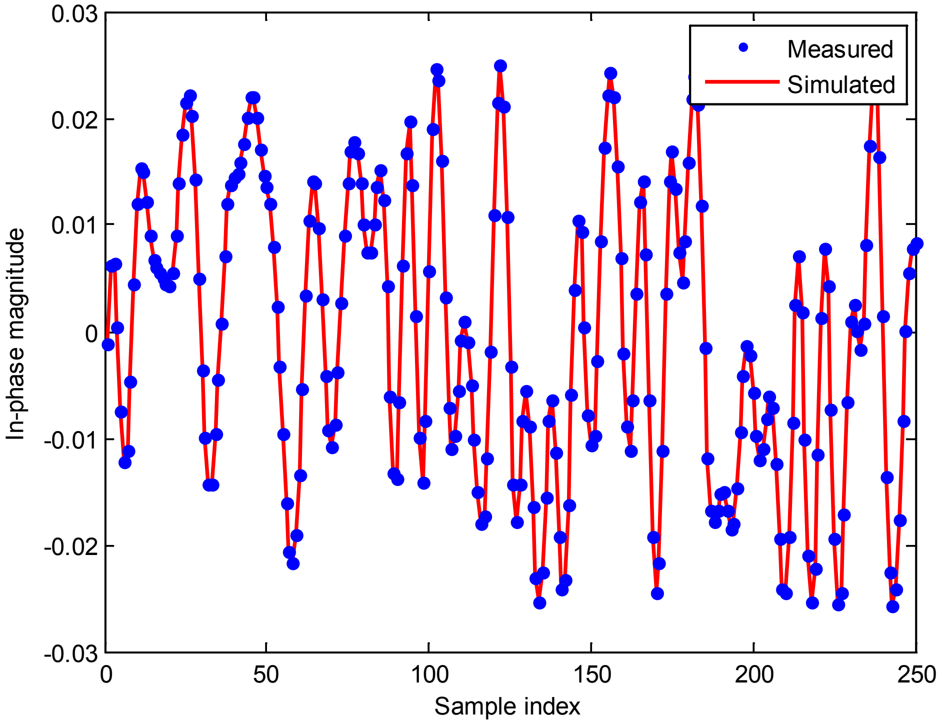

(a)

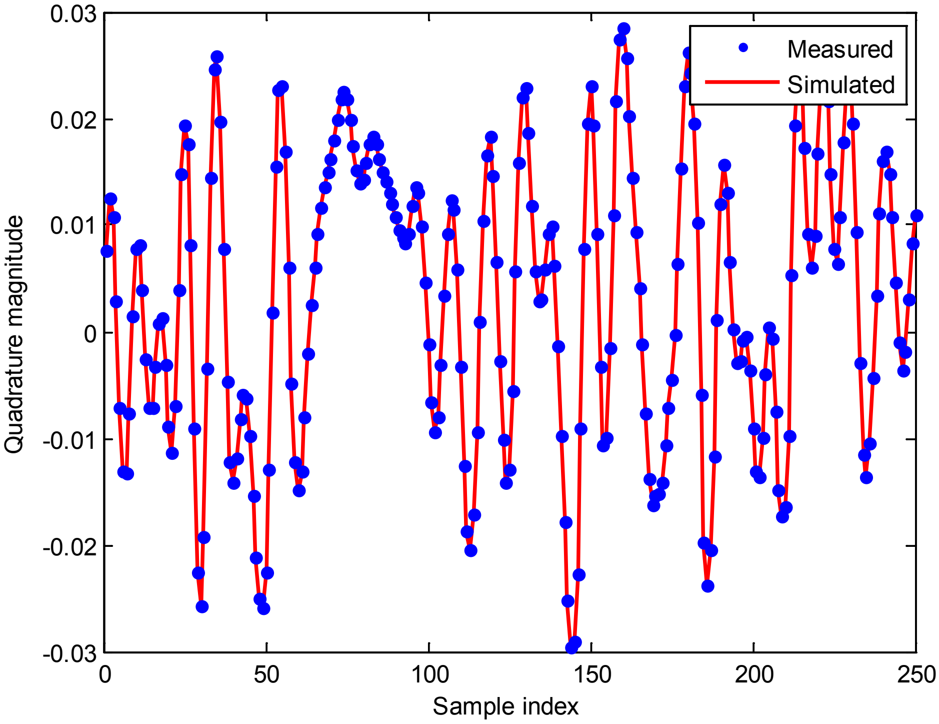

(b)

**Figure 3.9: Measured and modeled in-phase waveform (a) and quadrature waveform (b) in time domain.**

**Table 3.2: Performance of the GMP model versus nonlinear orders and memory depths.**

| Nr. Coeff. | $K_a$ | $L_a$ | $K_b$ | $L_b$ | $M_b$ | $K_c$ | $L_c$ | $M_c$ | NMSE (dB) |
|---|---|---|---|---|---|---|---|---|---|
| 3 | 3 | 1 | – | – | – | – | – | – | -28.63 |
| 5 | 5 | 1 | – | – | – | – | – | – | -28.65 |
| 20 | 5 | 4 | – | – | – | – | – | – | -43.88 |
| 30 | 5 | 6 | – | – | – | – | – | – | -44.01 |
| 40 | 5 | 8 | – | – | – | – | – | – | -44.08 |
| 32 | 5 | 6 | 2 | 1 | 1 | – | – | – | -45.06 |
| 38 | 5 | 6 | 2 | 1 | 4 | – | – | – | -45.70 |
| 54 | 5 | 6 | 2 | 3 | 4 | – | – | – | -45.93 |
| 78 | 5 | 6 | 4 | 3 | 4 | – | – | – | -45.96 |
| 56 | 5 | 6 | 2 | 3 | 4 | 2 | 1 | 1 | -46.02 |
| 64 | 5 | 6 | 2 | 3 | 4 | 2 | 1 | 5 | -46.09 |
| 74 | 5 | 6 | 2 | 3 | 4 | 4 | 1 | 5 | -46.15 |

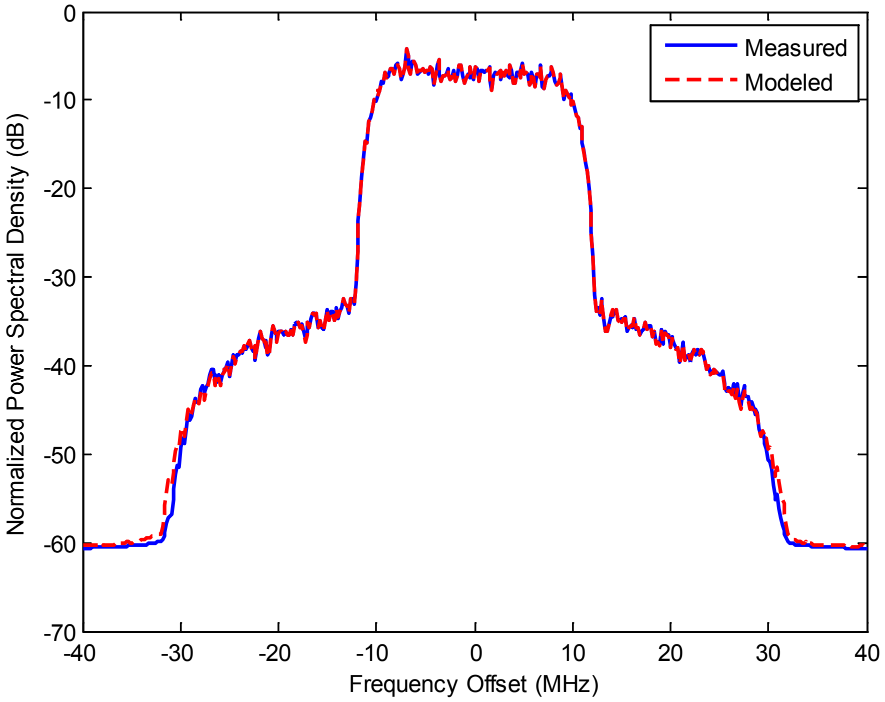

**Figure 3.10: Normalized power spectral density of measured and modeled outputs.**

After 64QAM demodulation, the constellations of the transmitted, measured and modeled symbols are shown in Fig. 3.11. The EVMs for measured and modeled output symbols are 5.72% and 5.71%, respectively, calculating by the formula (see Equation (2.16)).

The nonlinear distortion and memory effect of the RSOA modulator can be described by plotting its dynamic AM-AM and AM-PM characteristics. In Fig. 3.12, the AM-AM and AM-PM characteris-

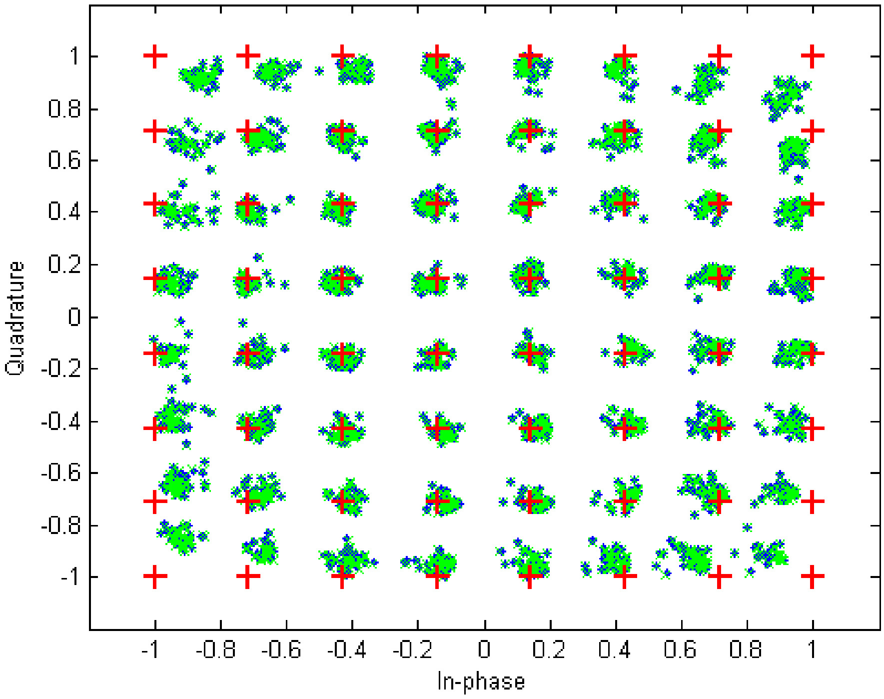

**Figure 3.11: Normalized constellation (red '+' for the transmitted symbol, blue '·' for the measured output, and green 'x' for the GMP model output).**

tics of the measured data are compared with those of the GMP output. It can be seen that the gain is compressed at the high-power level due to the average input power near the P1dB of the RSOA. It is also shown clearly that the GMP model can produce a similar scattering to ones exhibited by the measurement data since the memory effect is considered in the model. The GMP based model can accurately predict the dynamic behaviors of the RSOA modulator.

## 3.4 X-parameters

### 3.4.1 Polyharmonic Distortion (PHD) Model and X-parameters

As mentioned previously, the PHD modeling approach developed by Root and Verspecht [2,3] is a black-box frequency-domain nonlinear behavioral modeling technique that has been presented as a natural extension of S-parameters under large signal stimulus conditions. Since the model derives from a multi-harmonic linearization around a periodic steady state established by a large signal input tone, the system depends in a strongly nonlinear way on the large signal stimulus. Nevertheless, it responds linearly to additional harmonic components which can be considered as small perturbation around the time varying system state. This is so-called the harmonic superposition principle as

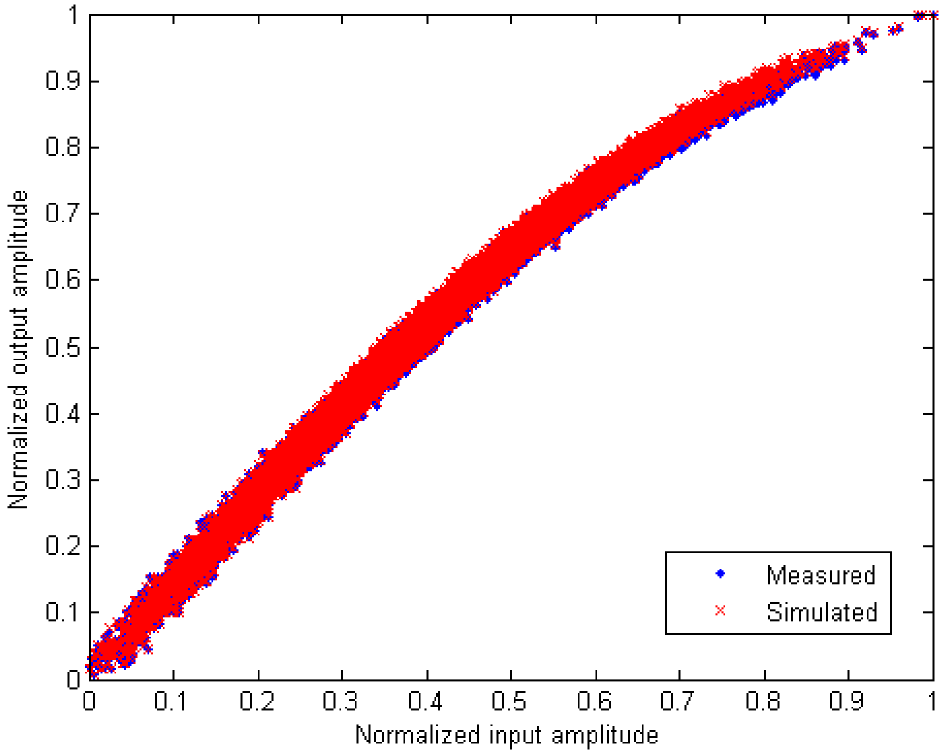

(a)

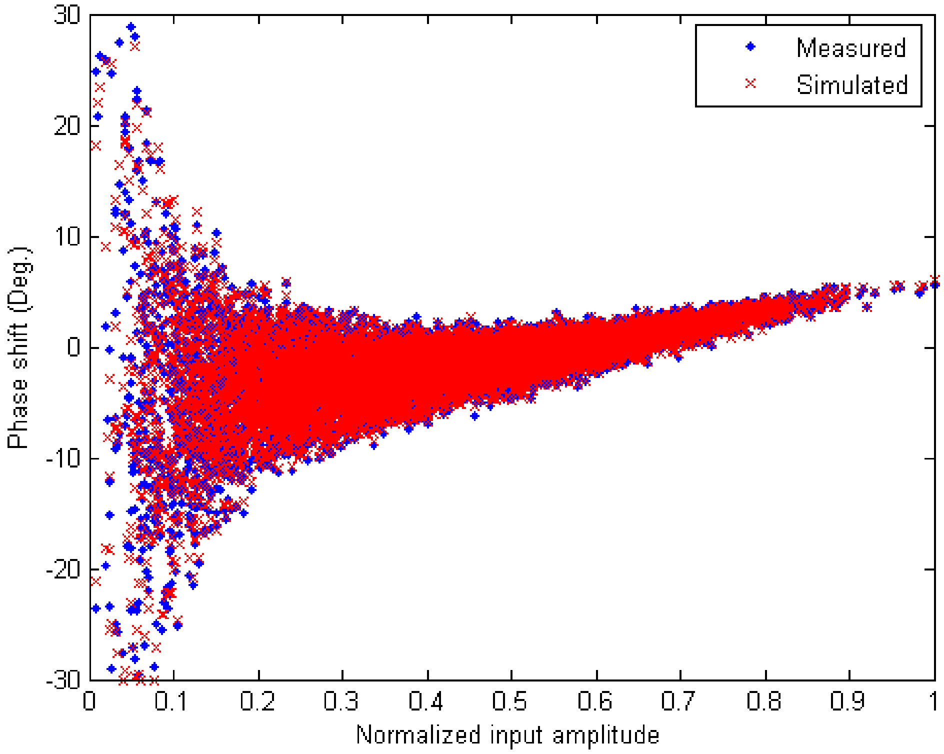

(b)

**Figure 3.12: Dynamic AM-AM (a) and dynamic AM-PM (b) characteristics of the RSOA modulator.**

illustrated graphically in Fig. 3.13. Basically, the PHD model uses the concept of harmonic superposition to analytically describe the large signal $B_{ef}$ wave response of a nonlinear device or system in terms of a mapping incident signals $A_{gh}$. The PHD model is identified from the response of a DUT stimulated by a set of discrete harmonic tones, where the fundamental tone is dominant and the harmonic tones are relatively small.

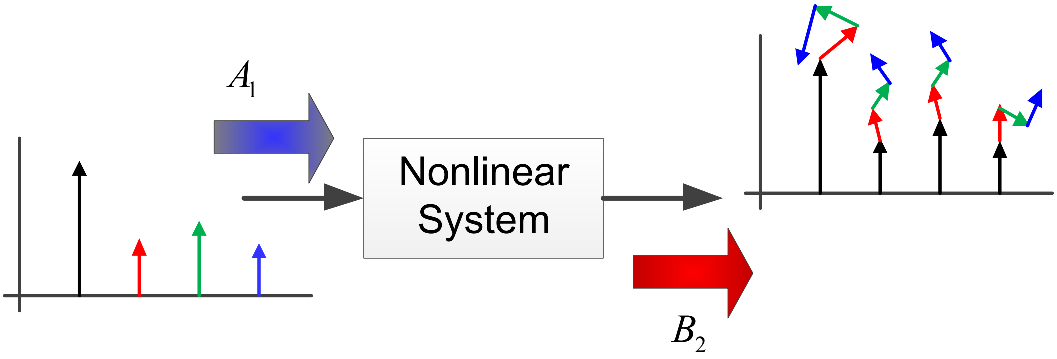

**Figure 3.13: The concept of harmonic superposition [2].**

X-parameters are derived from the PHD framework for linear and nonlinear modeling of a nonlinear device [78, 87]. X-parameters are much more powerful because they contain magnitude and phase information on all harmonics and inter-modulation spectra. X-parameter behavioral models may run significantly faster than circuit-level or physical models. For a one-tone large signal at port 1 at the fundamental frequency, the basic PHD model can be described as follows [87]

$$B_{ef} = X_{ef}^{(F)}(|A_{11}|)P^{f} + \sum_{g,h} X_{ef,gh}^{(S)}(|A_{11}|)P^{f-h}A_{gh} + \sum_{g,h} X_{ef,gh}^{(T)}(|A_{11}|)P^{f+h}A_{gh}^{*} \tag{3.18}$$

where $X_{ef}^{(F)}$, $X_{ef,gh}^{(S)}$ and $X_{ef,gh}^{(T)}$ are identified as X-parameters. $(\cdot)^{*}$ denotes the complex conjugate. $A_{11}$ is the large signal drive to the port 1 at the fundamental frequency. $P$ (equals to $A_{11}/\left|A_{11}\right|$) provides phase correction for harmonic conversion. $e$, $f$, $g$, and $h$ are the output port index, the output frequency index, the input port index and the input frequency index, respectively. $A_{gh}$ is the incident wave at input port $g$ and harmonic $h$. $B_{ef}$ is the reflected wave at output port $e$ and harmonic $f$. $X_{ef,gh}^{(S)}(\cdot)$ , $X_{ef,gh}^{(T)}(\cdot)$ are S-type and T-type X-parameters, providing the small-signal added-contribution to the reflected and phase-reversed reflected waves at output port $e$ and harmonic $f$ due to the incident wave at input port $g$ and harmonic $h$.

### 3.4.2 Extraction Procedure and Simulation Configures of X-parameters

Generally, X-parameters can be generated through measurement using a NVNA or from a simulation of a circuit-level design using the Agilent ADS software.

The NVNA based extraction of X-parameters is illustrated in Fig. 3.14, where the main element is the NVNA equipment. The NVNA allows to measure both amplitude and phase of all spectral components at both ports. The source 1 excite the DUT at port 1 with a large fundamental ($A_{11}$ as noted above). At a particular value of the large signal inputs, relatively small harmonic components are injected one by one at both port 1 and port 2, with all frequencies of interest, by using the source 2. Thus, the coefficients $X^{(F)}_{ef}$, $X^{(S)}_{ef,gh}$, and $X^{(T)}_{ef,gh}$ can be estimated by performing a least-squares fit algorithm on the measured data since the model is linear in the parameters. The procedure can be repeated for any value of the large signals.

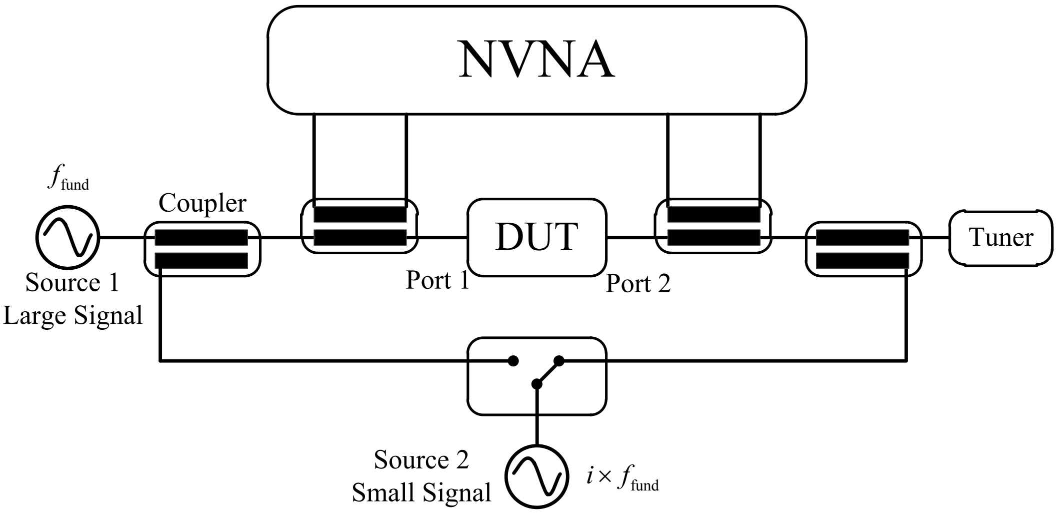

**Figure 3.14: NVNA based X-parameter extraction setup [3].**

Due to the NVNA unavailable in labs, in this section, we extract X-parameters from the physical model which has been developed in the previous chapter. A three-port configuration of X-parameters extraction using X-parameter generator in ADS is illustrated in Fig. 3.15. The RSOA used in the diagram is the physical model developed in chapter 2. The XP_Source component provides RF input signal and establishes power sweeps. The XP_Bias component is a bias source for X-parameter generator to establish DC biasing conditions. In our work we used a current source to bias the RSOA modulator. The XP_Load component provides a load or a load sweep if needed. After the generation, the extracted X-parameters will be saved into a data file and can be used for further simulation in both circuit level and system level. Furthermore, the extracted X-parameters can be easily transferred to any third party with the Intellectual Property (IP) protection. Fig. 3.16 shows plots of various X-parameters versus amplitudes of input signal for the RSOA modulator. The variations of the X-parameters with the input amplitude at high input power indicate the nonlinearity of the RSOA modulator.

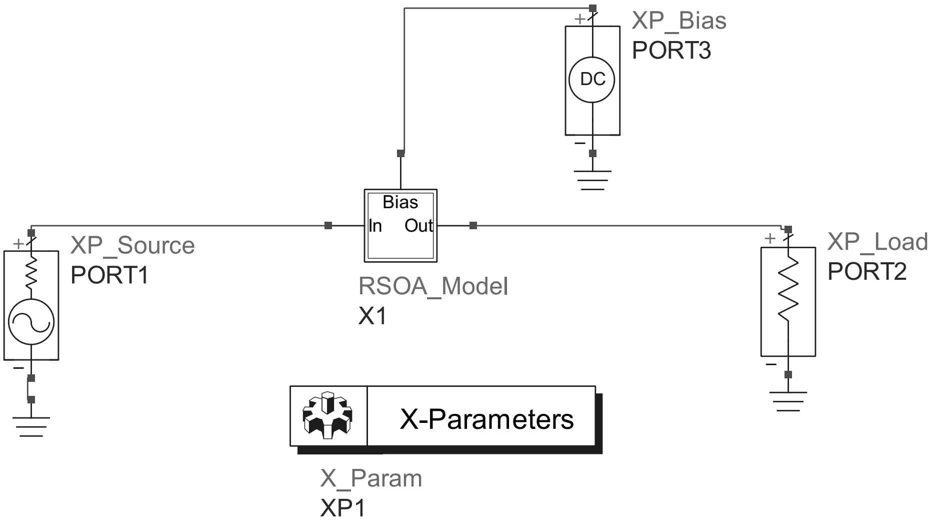

**Figure 3.15: Extraction of X-parameters based on the physical model of RSOA.**

The simulation setup schematic based on X-parameters is shown in Fig. 3.17. The ADS X3P component is a three-port X-parameter symbol and allows loading the X-parameter data file generated with the configure as shown in Fig. 3.15. The two DC blocks are used at input and output to prevent DC signals generated by the X-parameter model from affecting the signal source and sink. In order to compare the performance of both X-parameters and the physical model, the same simulation setup can be used for the physical model.

To demonstrate the harmonic distortion of the RSOA modulator, we swept the RF input power range from -15 to 20 dBm and carrier frequency range from 0.7 to 2.0 GHz for extraction of X-parameters and simulation. The magnitude and phase of the fundamental signals are shown in Fig. 3.18. The magnitude and phase of the third-order harmonic distortion are shown in Fig. 3.19. From these results, we can clearly see that X-parameter model can not only match the magnitude and phase of fundamental signals, but the magnitude and phase of harmonic components. The X-parameters based simulation ran five times faster than the physical model based one and can run even faster for more complex systems.

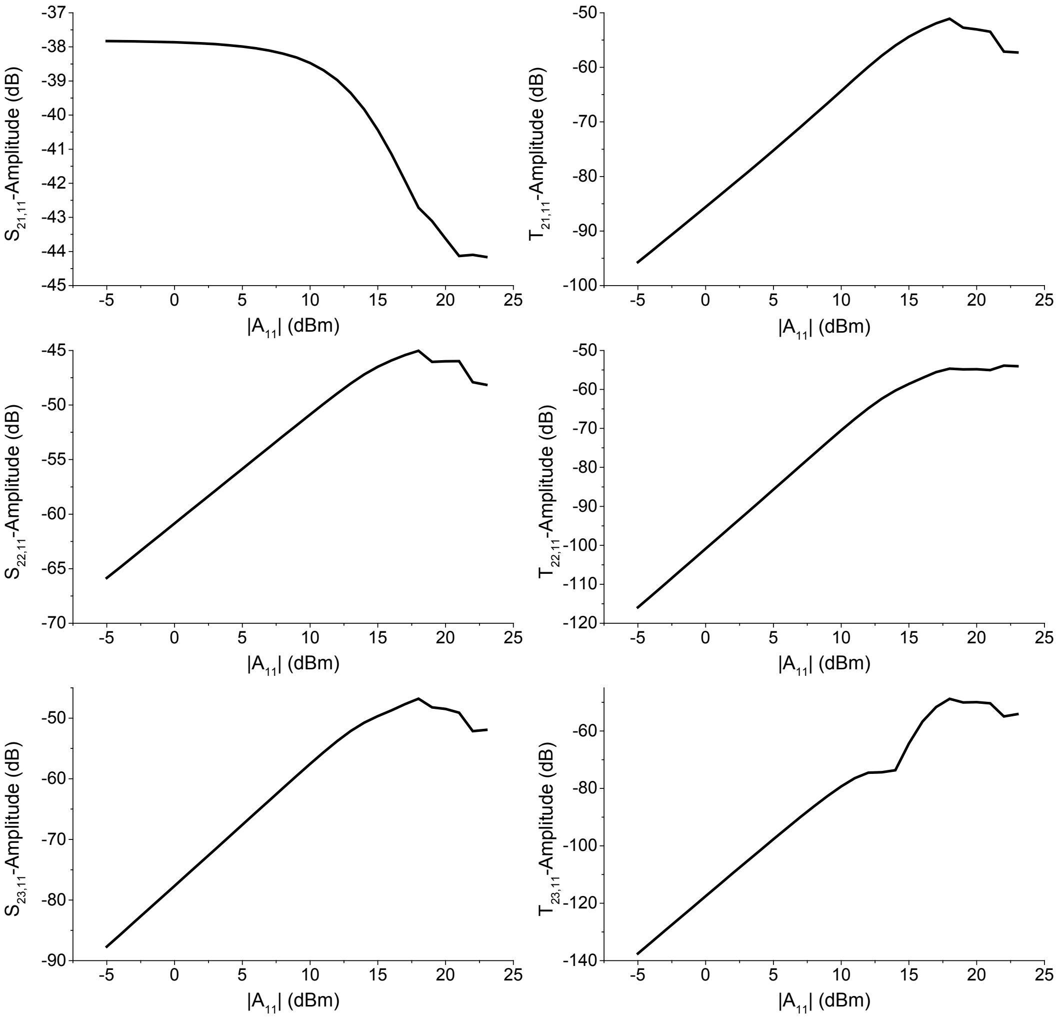

Figure 3.16: Plots of various types of X-paramters as a function of large signal amplitude ($|A_{11}|$).

Two-tone test signals were generated to demonstrate the inter-modulation components for the X-parameter model. The central frequency of two-tone signals was set to 1.0 GHz with the spacing of 10 MHz. The RF input power of the each tone signal was swept from -7 to 18 dBm under the different biases of 60 mA, 90 mA and 120 mA. The fundamental and IMD3 of X-parameter model and physical model are shown in Fig. 3.20. An excellent match is achieved between the X-parameter model and the physical model.

## 3.5 Summary

Three types of behavioral modeling approaches such as TDMLP, GMP and X-parameters were introduced to model the RSOA modulator.

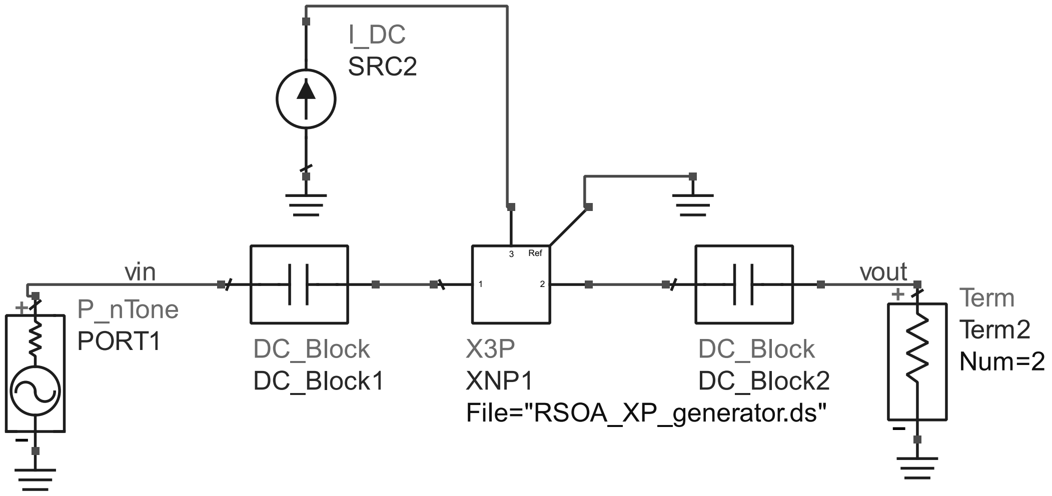

**Figure 3.17: Schematic diagram of simulation with X-parameters data.**

The dynamic nonlinear AM-AM and AM-PM characteristics of the RSOA modulator are demonstrated. The TDMLP and GMP models can produce a similar scattering to ones exhibited by the measurement data since the memory effects are considered in the models. The parameters of the models were adjusted to provide a best fit to experimental measurements. The accuracy of both TDMLP and GMP are evaluated with the NMSE as the figure of merit. Comparing the Table 3.1 and Table 3.2, we can see that the GMP based model exhibits the better performance for the RSOA modulator. The NMSE is up to 46.02 dB with 56 coefficients. From the results, The RSOA modulator does not show strong memory effects.

Basically, X-parameters are used under the large signal drive condition. X-parameters are extracted from the physical model developed in the previous chapter. Harmonic balance analysis was applied to demonstrate nonlinear distortions of the RSOA modulator. Therefore, harmonic and intermodulation distortions can be depicted. X-parameters run five times faster than the physical model, even faster for a complex simulation.

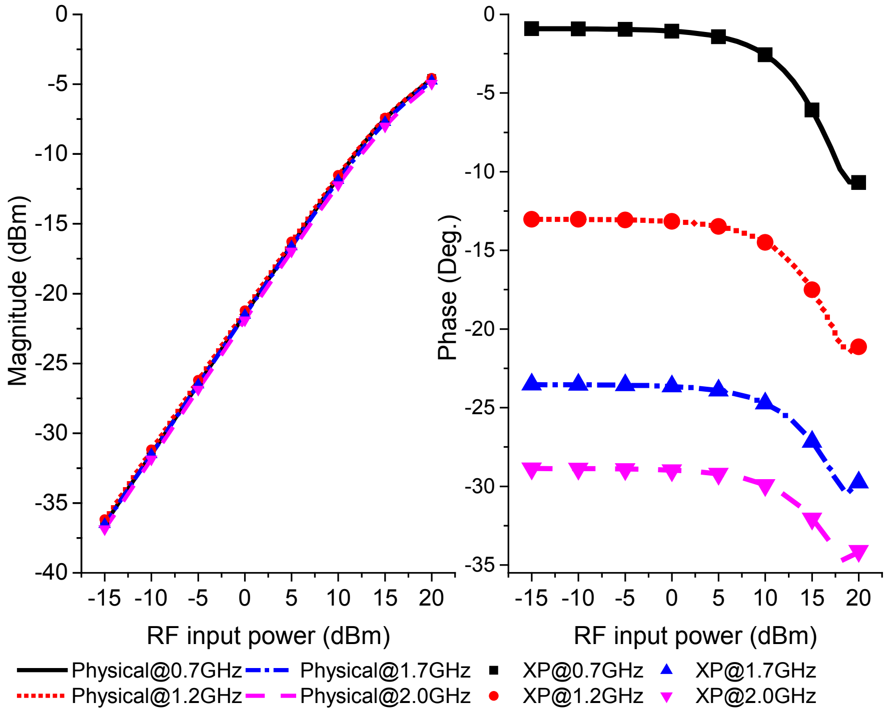

**Figure 3.18: Fundamental magnitude (left) and phase (right) as a function of the input power under different carrier frequencies of 0.7 GHz, 1.2 GHz, 1.7 GHz and 2.0 GHz.**

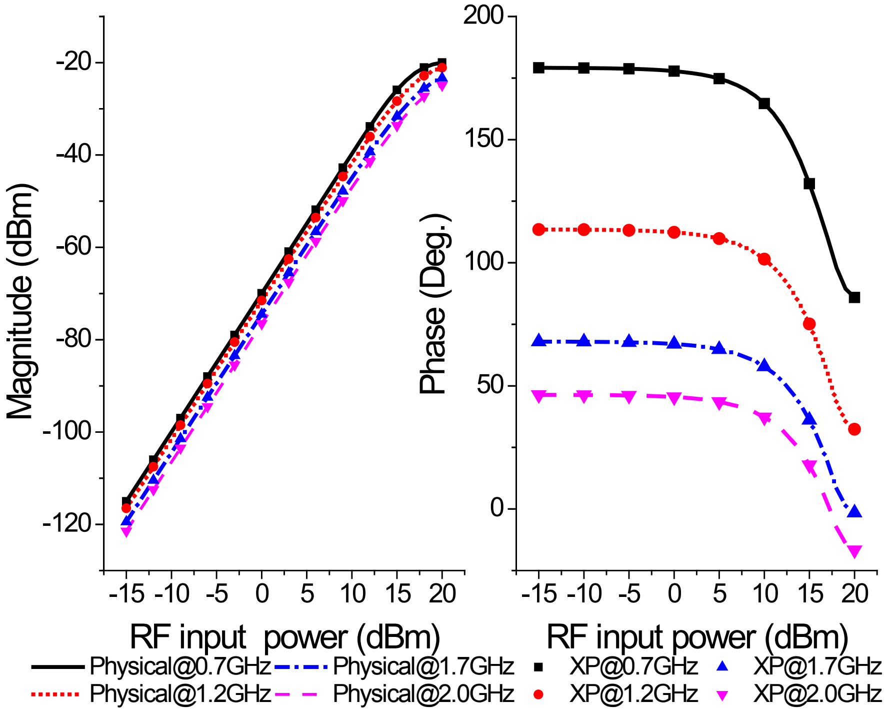

**Figure 3.19: Third harmonic magnitude (left) and phase (right) as a function of the input power under different carrier frequencies of 0.7 GHz, 1.2 GHz, 1.7 GHz and 2.0 GHz.**

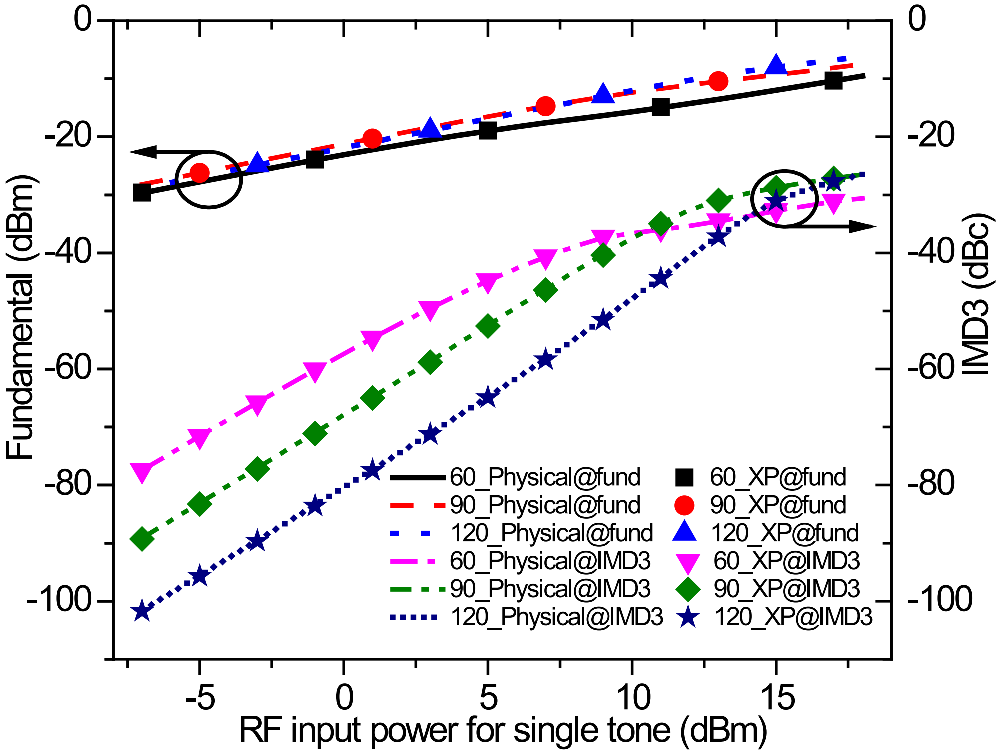

Figure 3.20: Fundamental and IMD3 as a function of the RF input power under two-tone test at different bias currents of 60 mA, 90 mA and 120 mA.

# Chapter 4

# Nonlinear Distortions and Compensation

*The work presented in this chapter focuses on compensation techniques in RoF links. The nonlinear distortions of the RSOA modulator in RoF links were experimentally compensated by using a GMP based predistortion approach.*

## 4.1 Introduction

The RoF links have adequate bandwidth to support wide band and high data rates services. However, when radio links are in cascade with optical links, the nonlinear distortion in RoF links becomes the main issue [54,88]. As mentioned previously, the major impairments in the RoF links is the nonlinear distortion caused mainly by the optical modulator, specifically RSOA modulator in our work, rather than the PD. The dynamic range of the RoF links is limited due to nonlinear distortion of the optical modulator. As we know, the nonlinearity of the device generates new frequencies, for instance, harmonic and intermodulation components which spread the signal bandwidth, in term of spectral regrowth, as shown in Fig. 4.1 under two-tone excitation with frequencies $\omega_1$ and $\omega_2$. The dynamic range is typically characterized by the IMD. For instance, under two-tone excitation, the most important components are $2\omega_1 - \omega_2$, $2\omega_2 - \omega_1$, $3\omega_1 - 2\omega_2$, $3\omega_2 - 2\omega_1$, and so on, so called the intermodulation components. They fall into "Zone 1" and are so close to the fundamental components. Therefore, it is difficult to eliminate them by filters. The other components can be removed by filtering.

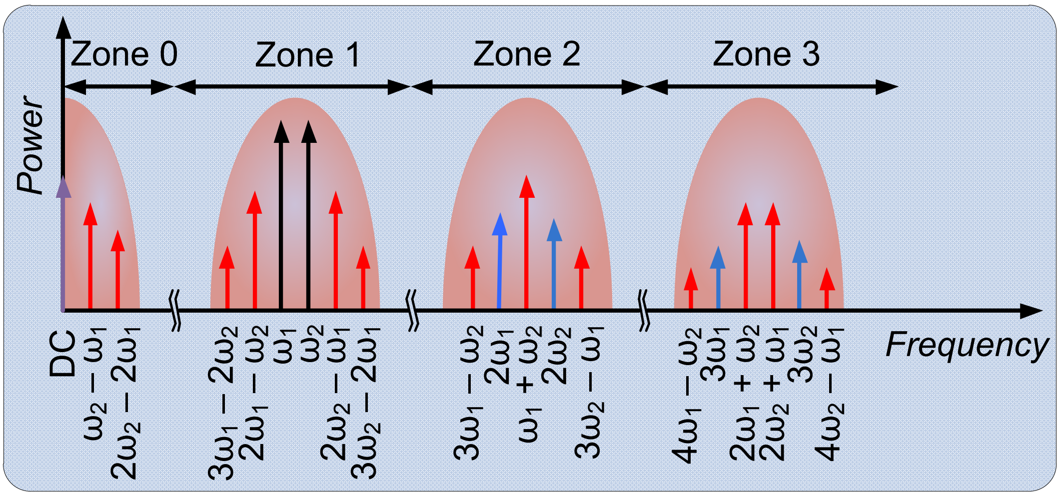

**Figure 4.1: Response spectral of a nonlinear device to a two-tone excitation with frequencies $\omega_1$ and $\omega_2$.**

## 4.2 Distortion Compensation Techniques

As mentioned earlier, methods for the compensation of nonlinearities in RoF links can be categorized into two main types: in optical domain and in electrical domain [54].

### 4.2.1 Optical Distortion Compensation

The optical compensation methods typically require the use of duplicate lasers or external modulators by selecting the biases such that the transfer function of the combination is more linear than the individual ones [54]. This approach has economic disadvantages due to high costs for the additional optical components. The use of the optical distortion compensation, however, achieves a very wide compensation bandwidth.

### 4.2.2 Electrical Distortion Compensation

In the electrical domain, a number of linearization techniques have been proposed for RoF links. The most popular techniques are feedforward linearization and predistortion linearization[1] as shown in Fig. 4.2. In the feedforward configure the RF signal is split into two branches as shown in Fig. 4.2(a). In the upper branch, the signal modulates directly optical lightwave via a laser or other modulator. A part of optical signal is coupled and converted into an electrical signal with a PD (PD1). This electrical signal is subtracted with the lower branch electrical signal, which is first through a

---

[1] Here lasers are used in the diagram. In Fact, they can be other modulators such as MZM and RSOA.

proper electrical delay, to generate an error signal, or intermodulation components in the spectral domain. The second electrical delay (delay2) is used to adjust the phase of the error signal. The error signal modulates the second laser (laser2) after being amplified and is injected into the first branch. The distortions can be canceled or reduced. This technique also requires additional optical devices and therefore increases the cost of the systems. It has been implemented for a DML [64] and externally modulated analog fiber-optic links [89].

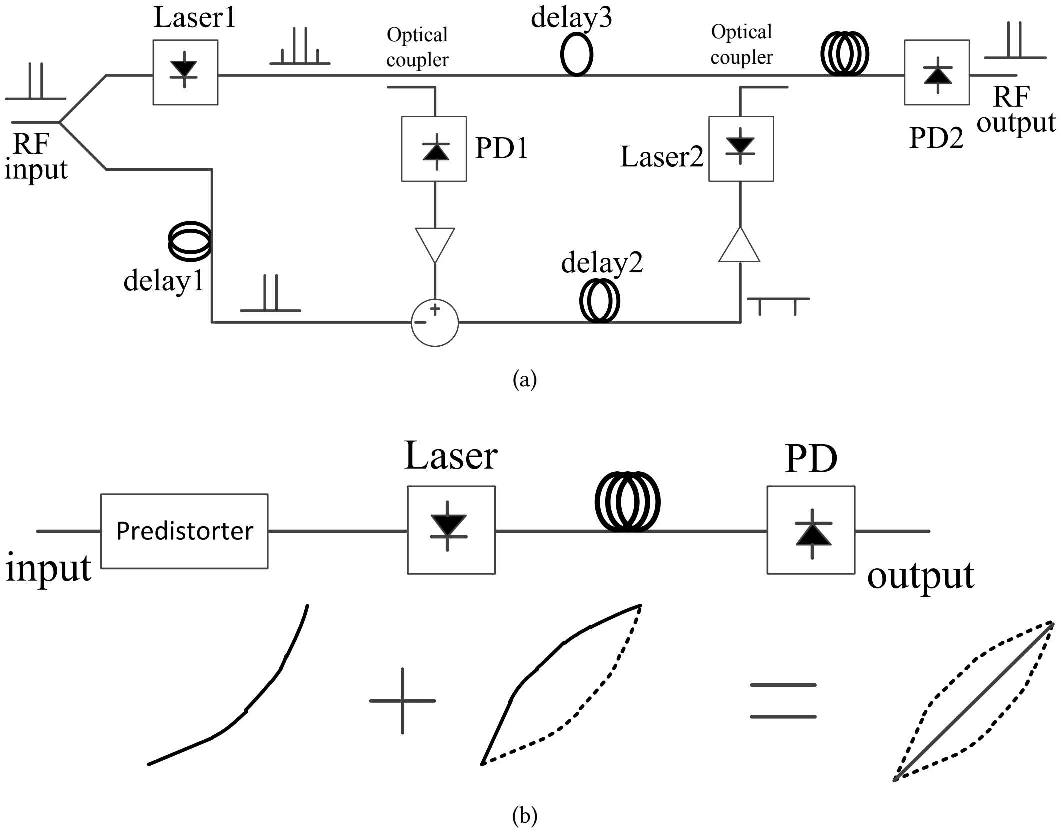

(a)

(b)

**Figure 4.2: Schematic diagrams of electrical compensation. (a): feedforward and (b): predistortion.**

The main principle of the predistortion is to insert a circuit with the inverse of the nonlinearity of the laser or other modulators as shown in Fig. 4.2(b). Due to its simplicity, predistortion has been widely proposed and used to compensate the nonlinearities of RF power amplifiers [50, 51, 61, 90], MZM [66] and DFB laser [91–93]. Memory effects are usually considered in most of predistortion models to improve the linearization performance.

In this chapter we attempt to compensate the nonlinearity of the RSOA modulator with the predistortion techniques based on the memory polynomial model.

## 4.3 GMP Predistorter

In order to compensate the nonlinear distortion of the RSOA modulator in RoF links, a predistorter scheme based on GMP [61] is used, and given by

$$\begin{aligned} \tilde{u}(n) \;=\; & \sum_{k=1}^{K_a} \sum_{l=0}^{L_a-1} a_{kl} \tilde{y}\left(n-l\right) \left|\tilde{y}\left(n-l\right)\right|^{k-1} \\ +\; & \sum_{k=1}^{K_b} \sum_{l=0}^{L_b-1} \sum_{m=1}^{M_b} b_{klm} \tilde{y}\left(n-l\right) \left|\tilde{y}\left(n-l-m\right)\right|^{k} \\ +\; & \sum_{k=1}^{K_c} \sum_{l=0}^{L_c-1} \sum_{m=1}^{M_c} c_{klm} \tilde{y}\left(n-l\right) \left|\tilde{y}\left(n-l+m\right)\right|^{k} \end{aligned} \tag{4.1}$$

where $\tilde{u}$ and $\tilde{y}$ are the complex envelopes of the input and output of the DUT, respectively; $K_a$, $K_b$and $K_c$ are the order of nonlinearity; $L_a$, $L_b$, $L_c$, $M_b$ and $M_c$ are the memory lengths; $a_{kl}$, $b_{klm}$and $c_{klm}$ are the corresponding coefficients of the DPD.

The identification of the predistorter is carried out by using an indirect learning architecture [51, 62] as depicted in Fig. 4.3. The complex envelope signals are first captured from the input and output of the RSOA modulator. Since the *p*th-order pre-inverse transfer function is identical to the *p*th-order post-inverse transfer function [62] as shown in Fig. 4.4, the input and output of the DUT can be regarded as the output and input of the DPD model in order to inverse the characteristics of the DUT. Thus the coefficients of the model can be simply extracted with an offline process. Once the estimation of the coefficients of the model, they are directly copied to the predistorter which will be running in open-loop mode. Note that in case of nonlinear time-variant systems, the training branch should be always connected [94].

As the model is linear in the coefficients, the linear least-squares error minimization method can be used to estimate the coefficients of the model, which is described by

$$\hat{\mathbf{h}} = \left(\mathbf{Y}^H \mathbf{Y}\right)^{-1} \mathbf{Y}^H \mathbf{u} \tag{4.2}$$

where $(\cdot)^H$ represents the Hermitian transpose. $\hat{\mathbf{h}}$ has the same meaning as in 3.12.

The matrix $\mathbf{Y}$ and vector $\mathbf{u}$ are described in detail by equations (4.3) and (4.4), respectively.

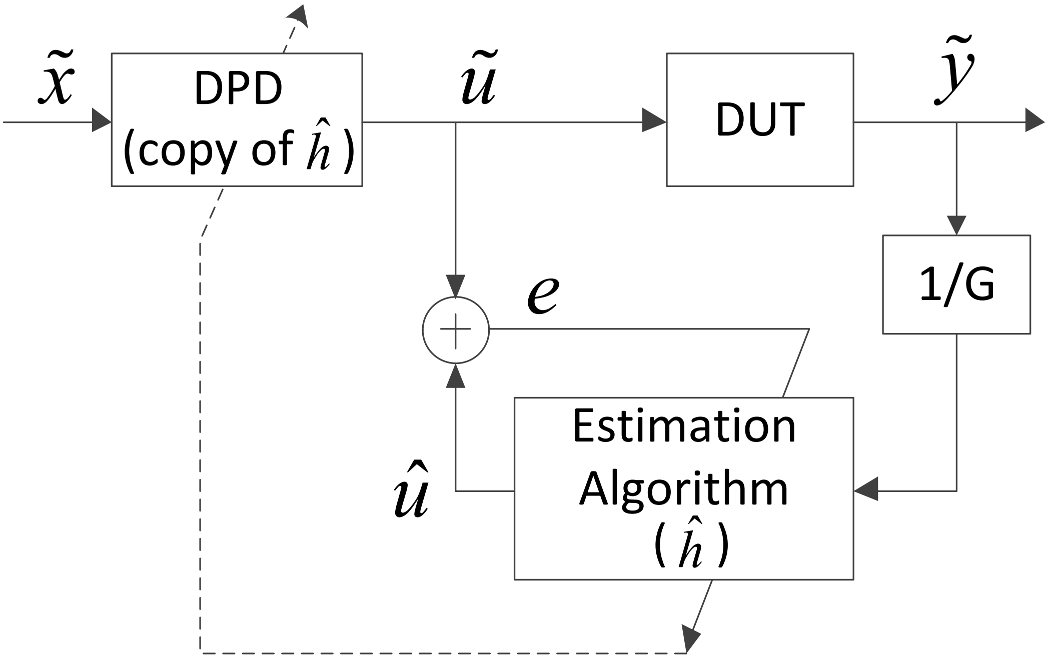

Figure 4.3: Schematic diagram of predistortion characterization by using indirect learning architecture.

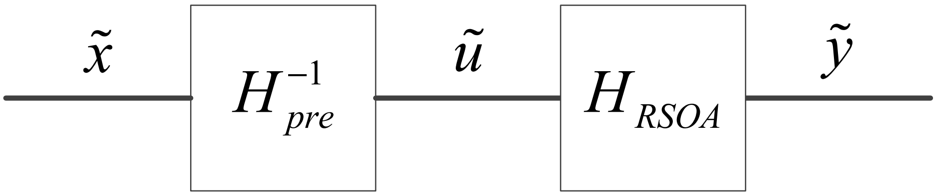

(a)

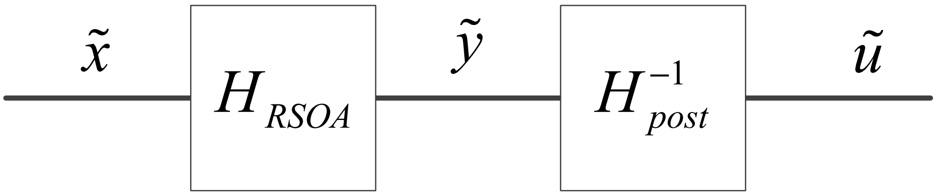

(b)

Figure 4.4: *P*th order inverse: (a) pre-inverse and (b) post-inverse.

$$\mathbf{Y} = \begin{bmatrix} \tilde{y}(0) & \cdots & \tilde{y}(-(L_a-1))|\tilde{y}(-(L_a-1))|^{K_a-1} & \tilde{y}(0)\,|\tilde{y}(-1)| & \cdots & \tilde{y}(-(L_b-1))|\tilde{y}(-(L_b-1)-M_b)|^{K_b} & \tilde{y}(0)\,|\tilde{y}(1)| & \cdots & \tilde{y}(-(L_c-1))|\tilde{y}(-(L_c-1)+M_c)|^{K_c} \\ \vdots & & \vdots & \vdots & & \vdots & \vdots & & \vdots \\ \tilde{y}(n) & \cdots & \tilde{y}(n-(L_a-1))|\tilde{y}(n-(L_a-1))|^{K_a-1} & \tilde{y}(n)\,|\tilde{y}(n-1)| & \cdots & \tilde{y}(n-(L_b-1))|\tilde{y}(n-(L_b-1)-M_b)|^{K_b} & \tilde{y}(n)\,|\tilde{y}(n+1)| & \cdots & \tilde{y}(n-(L_c-1))|\tilde{y}(n-(L_c-1)+M_c)|^{K_c} \\ \vdots & & \vdots & \vdots & & \vdots & \vdots & & \vdots \\ \tilde{y}(N-1) & \cdots & \tilde{y}(N-1-(L_a-1))|\tilde{y}(N-1-(L_a-1))|^{K_a-1} & \tilde{y}(N-1)\,|\tilde{y}(N-1-1)| & \cdots & \tilde{y}(N-1-(L_b-1))|\tilde{y}(N-1-(L_b-1)-M_b)|^{K_b} & \tilde{y}(N-1)\,|\tilde{x}(N-1+1)| & \cdots & \tilde{y}(N-1-(L_c-1))|\tilde{y}(N-1-(L_c-1)+M_c)|^{K_c} \end{bmatrix} \tag{4.3}$$

and

$$\mathbf{u} = \begin{bmatrix} \tilde{u}(0) & \cdots & \tilde{u}(n) & \cdots & \tilde{u}(N-1) \end{bmatrix}^T \tag{4.4}$$

where $(\cdot)^T$ denotes the transpose.

In order to obtain the predistorted RF input signal of the DUT, the predistorted baseband output signal of the DPD $\hat{\mathbf{u}}$ can be first obtained by

$$\hat{\mathbf{u}} = \mathbf{X}\hat{\mathbf{h}} \tag{4.5}$$

where $\mathbf{X}$ is the baseband input signal matrix ($N \times P$) of the DPD, which is also the desired output signal of the DUT and is similar with the matrix $\mathbf{Y}$.

## 4.4 Results and Discussion

In order to extract the coefficients of the DPD and generate the predistorted signal for the RSOA modulator, two random 64QAM signals with 20 Msymbol/s, which were filtered with a SRRC filter with the roll-off factor of $\alpha = 0.22$, were generated in MATLAB. One is used to estimate the parameters of the DPD. The other is to generate the desired predistorted signal. The experimental test bench is shown in Fig. 3.2. Next, higher power transmission experiments are performed to show that effects of nonlinearity of the RSOA modulator are being compensated by the DPD. The RF signals used to drive the RSOA is with the average power of 13 dBm, which is near the P1dB point of the RSOA. Its PAPR is around 7.1 dB. The predistorted signal can be obtained with Equation (4.5). Its PAPR is around 10.8 dB.

The dynamic AM-AM and AM-PM performances of the RSOA modulator without and with the DPD and the predistorted signal are shown in Fig. 4.5 and 4.6, respectively. From these figures, we can clearly see that the nonlinear distortion and memory effects of the RSOA modulator have been successfully compensated.

To evaluate the performance in frequency domain, the normalized power spectral densities without and with the DPD and the transmitted signal are plotted in Fig. 4.7. It is clearly shown that the third order intermodulation distortion has been improved by around 17 dB with the DPD when compared to the situation without the DPD.

After demodulation process in MATLAB, the constellations without and with the DPD and for the transmitted symbols are shown in Fig. 4.8. It can also be clearly seen that the nonlinearity effects of the RSOA modulator have been successfully compensated. To further evaluate the performance of the DPD, the EVM defined in Equation (3.9) is used as a figure of merit. The EVMs without and with the DPD are 6.1% and 2.0%, respectively.

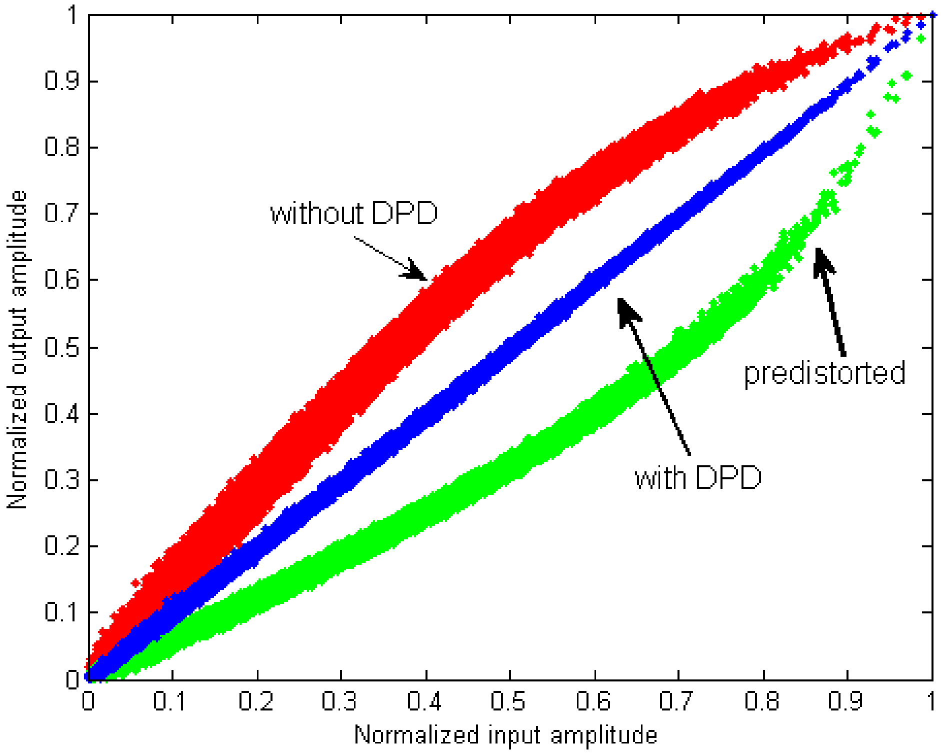

**Figure 4.5: Dynamic AM-AM characteristics of the RSOA modulator without DPD, with DPD and predistorted signal.**

## 4.5 Summary

This chapter addressed the compensation on the nonlinear distortion of the RSOA modulator based on the memory polynomial model.

By adding the predistorter, the RSOA modulator can be allowed to operate the nonlinear region, thereby the significantly increasing its dynamic range. As demonstrated experimentally, the nonlinear distortion can be improved up to 17 dB. The memory effect can also be compensated due to the memory considered in the model.

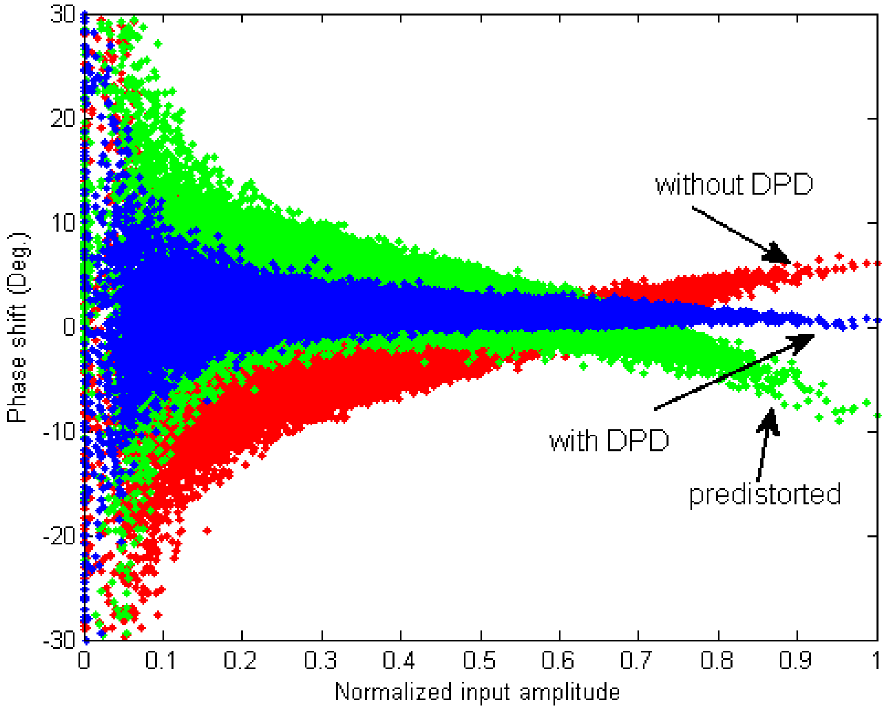

Figure 4.6: Dynamic AM-PM characteristics of the RSOA modulator without DPD, with DPD and predistorted signal.

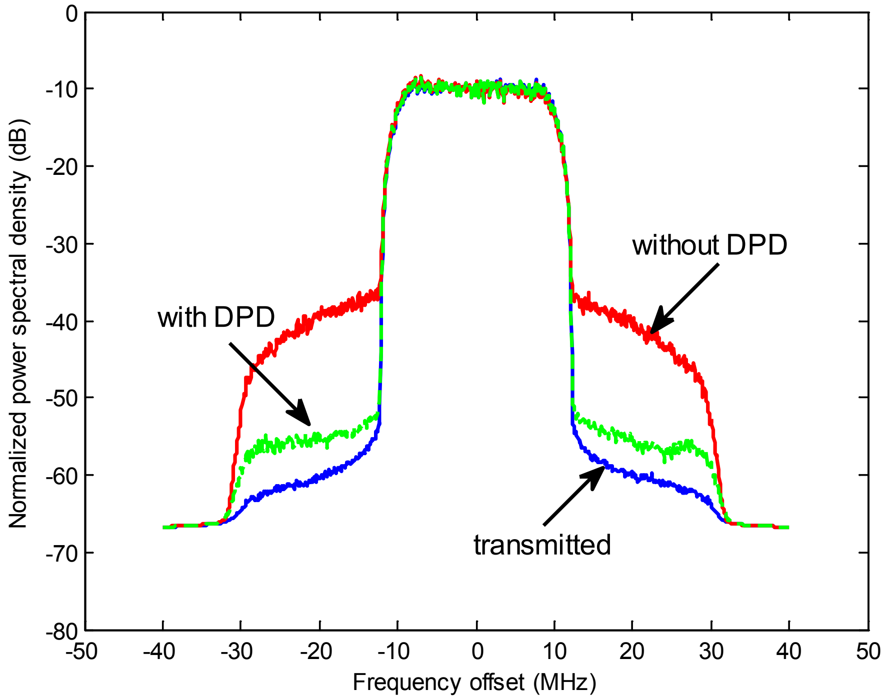

Figure 4.7: Normalized output power spectra of the RSOA modulator without DPD, with DPD and spectrum of the transmitted signal.

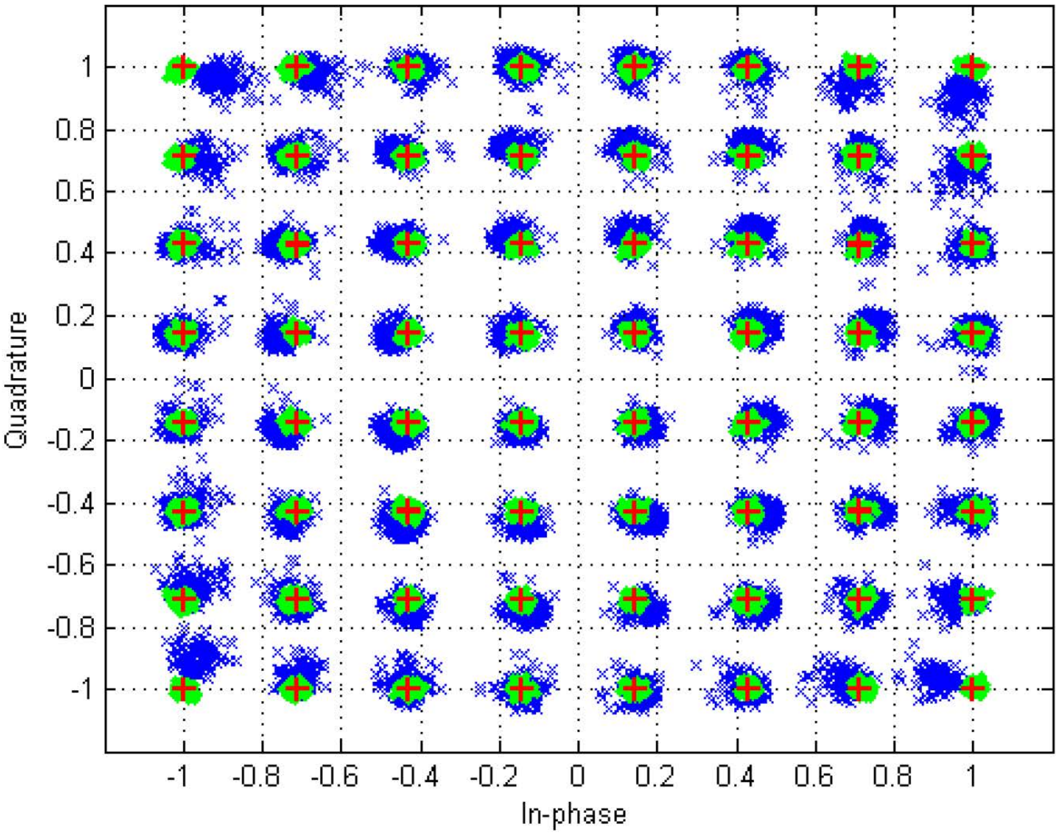

**Figure 4.8: Normalized constellation. (blue 'x' for without DPD, green '·' for with DPD, and red '+' for the transmitted symbols).**

## Chapter 5

# Transmission Performance of Multi-Channel Systems

*This chapter is a part of the FUTON project. In chapter 2 we have developed and validated a simple physical model for the RSOA modulator. This chapter will address the prediction of the performance of FUTON system by using the developed model.*

## 5.1 Introduction

There is currently in the wireless arena considerable research aiming at what is commonly called Fourth Generation (4G) systems that are spurred by interdependent technical and economical deployment trends. Such 4G systems should fulfill several goals, among which are the provision of true broadband wireless access, for which a new air interface has to be developed, and the enhanced system capacity when compared with current Third Generation (3G) networks.

Towards 4G, changes in the wireless systems architectures are necessary. For instance, in order to support more users at higher data rates, the use of higher radio carrier frequencies is required, which results in smaller radio cells (in a cellular system), due to increased propagation losses and line-of-sight restrictions. However, since interference does not undergo the same scaling effect as the cell size, the system capacity does not increase proportionally with cell size reduction. Due to the radio cells reduction at higher frequencies, more and more antenna sites are needed to cover a certain area.

Since the work presented in this chapter is based on the FUTON project, an overview of the FUTON project is first presented. The transmission performance of the FUTON system is predicated by using the physical model developed previously.

## 5.2 Overview of FUTON Project

The FUTON is an international collaborative EU FP7 research project, that started in January 2008 and finished in September 2010, and involved 16 research institutes, universities, manufacturers and operators. The FUTON project aimed at researching, developing and validating a flexible architecture for wireless systems based on the joint processing of the radio signals from a large number of RAUs and supported by a transparent fiber infrastructure. This architecture enables the high bit rates targeted for the broadband component of future wireless systems and provides a framework for the integration of the various current heterogeneous wireless systems. The FUTON infrastructure provides enough flexibility to share its resources by a wide range of wireless systems and also by fixed optical connections. The supported systems should include outdoor Distributed Broadband Wireless System (DBWS), where the infrastructure acts as a virtual MIMO enabler to achieve the target high bit rates, indoor DBWS, and also the remote control of dedicated radio systems. A general FUTON architecture is depicted in Fig. 5.1. The system is composed of the number of RAUs and the optical fiber infrastructure, which transport the user and network information to the central unit for its processing. In the context of the FUTON architecture, the different systems can coexist in a serving area and are connected to the same CU.

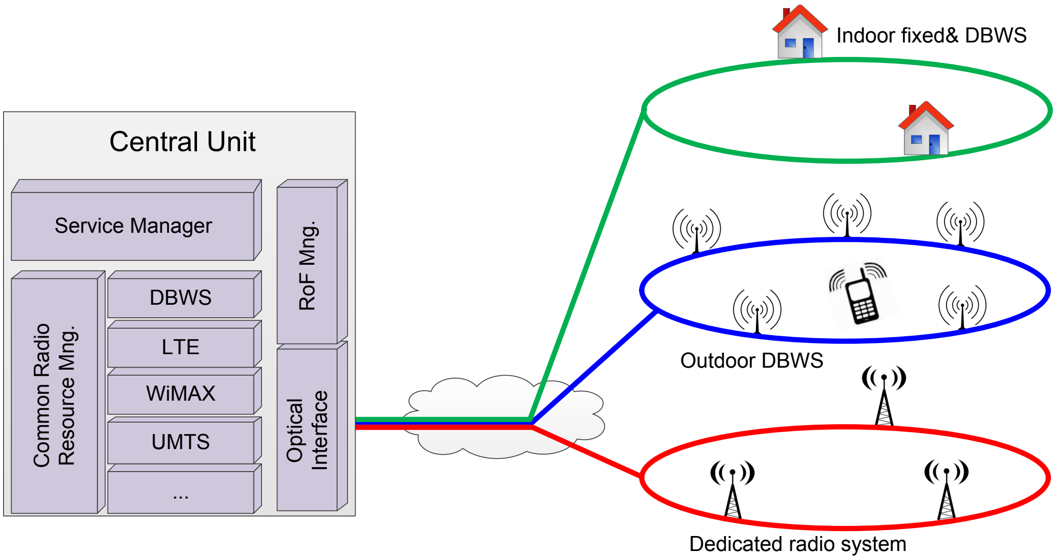

**Figure 5.1: FUTON architecture [4].**

The main objectives of the FUTON project were

- Specify, design, implement and provide proof of concept for a hybrid optical-radio infrastructure enabling the high bit rates envisioned for 4G.
- Exploit the potentialities offered by the infrastructure to develop mechanisms for inter-system coordination and optimum usage of the radio resources and provide the proof of concept.
- Evaluate the implications on the current wireless architecture models of the FUTON concept.

These FUTON links are designed to support the transport of 4 different radio channels per link direction. Each of these channels carries DBWS signals between the CU and the RAUs. The link budget calculation for the RSOA-based link, focused only on the Uplink (UL) direction, as explained previously, and the components and parameter values of this link are in detail presented in Fig. 5.2.

The IF plan defined for FUTON DBWS transmission is depicted in Fig. 5.3. The Downlink (DL) and UL channels are not interleaved, instead they occupy separate bands. The UL band is below 1 GHz so that the RSOA can be used as a transmitter option.

## 5.3 Optical Subcarrier Multiplexing

The use of MIMO results in an increase in the number of radio channels. all of these signals have the same carrier frequency and bandwidth. They cannot be transported via the same optical fiber without any multiplexing scheme. Three multiplexing schemes are categorized as follows.

- Space Division Multiplexing (SDM), in which each signal is delivered to a separate optical fiber. These scheme requires one optical source and one fiber for each signal.
- WDM, in which each signal modulates a separate optical source with a separate wavelength. All signals can be transported via the same optical fiber. Therefore, the WDM scheme requires one optical source for each signal.
- SCM, in which each signal is converted a separate IF. These IF signals can combined in the radio domain and then modulate a lightwave. The SCM scheme requires one optical source for all signals, and one frequency conversion per signal at each transmitter and receiver sides for each transmission direction.

For the FUTON system, frequency translation (subcarrier multiplexing) would be necessary to accommodate the radio channels being specified for the DBWS, since it is envisaged that multiple

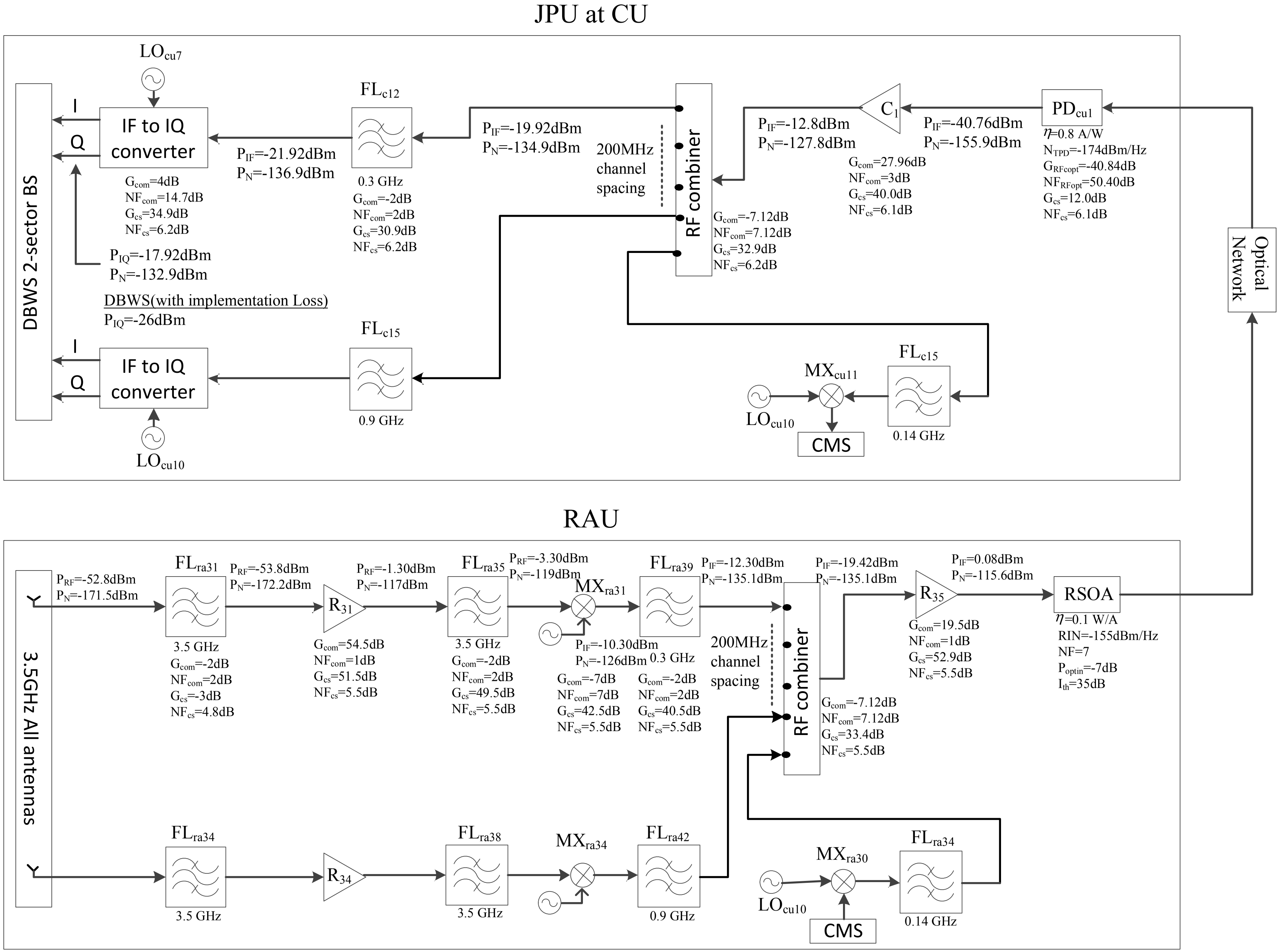

Figure 5.2: Detailed uplink system power budget for RSOA-based links [4].

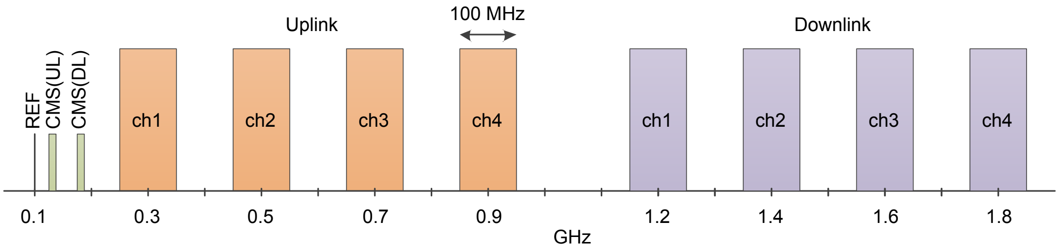

**Figure 5.3: IF frequency plan for a 2×4-channel RoF link architecture in the FUTON project. (CMS: control/monitor/synchronization)**

channels operating at the same radio frequency must be transmitted between the CU and RAU over a single optical link. As mentioned earlier, the FUTON systems provide the virtual MIMO scheme with SCM techniques.

Optical SCM is depicted in Fig. 5.4. Several individual signals are multiplexed by separate carriers in the electrical domain and used to modulate an optical carrier with an E/O at a transmitter. At a receiver the electrical signals are recovered by an O/E such as a photodetector. And then the carriers are separated with the corresponding local oscillators. This gives an advantage over a pure WDM access, due to the lower cost of electrical components if compared with an optical multiplexer. The mature microwave devices such as stable microwave oscillators and high selectivity electrical filters are also more superior to the corresponding optical counterparts. But SCM is limited in maximum subcarrier frequencies and data rates by the available bandwidth of the electrical and optical components. SCM usually is used in conjunction with WDM in order to take advantage of most of the available fiber bandwidth. In multichannel application a wideband RF signal will suffer from distortion from both in-channel and out-of-channel signals due to the nonlinear behavior of the E/O modulator. Therefore, the harmonic and intermodulation products generated by the RSOA modulator between channels become one of the important limiting factors in performance of RoF links.

## 5.4 Predicted Performance of the Multi-Channel System

Based on the model developed for the RSOA link type, and on its corresponding experimental validation, the performance of the RSOA link in the FUTON systems can be predicted. The performance was evaluated by using the EVM as the figure of merit to assess the signal degradation caused mainly by the intrinsic nonlinearity of the RSOA modulator.

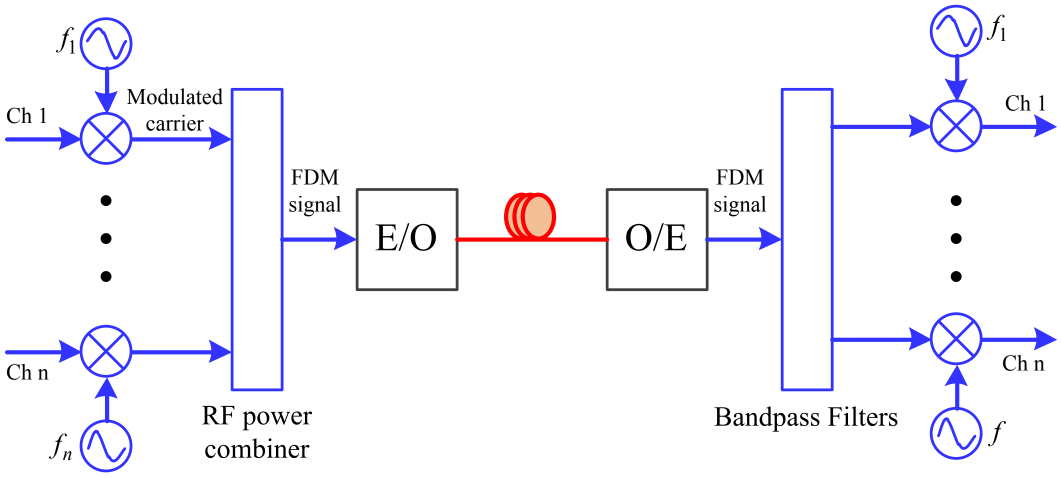

**Figure 5.4: Basic schematic diagram of the optical SCM.**

In this section, we attempted to use a Virtual Photonics Inc. (simulation software manufacturer) (VPI)/ADS co-simulation to predict the performance of the FUTON since the VPI provides an OFDM modulator module by which the arbitrary bandwidth OFDM signal could be generated by setting corresponding parameters. The co-simulation schematic is depicted in Fig. 5.5. A co-simulation interface block is used to pass the data into the ADS where the physical model has been implemented. An OFDM receiver decodes the electrical OFDM signals and evaluates EVMs of the signals. The carrier frequencies of the four channels in the FUTON uplink are set to 0.3 GHz, 0.5 GHz, 0.7 GHz and 0.9 GHz as defined in Fig. 5.3.

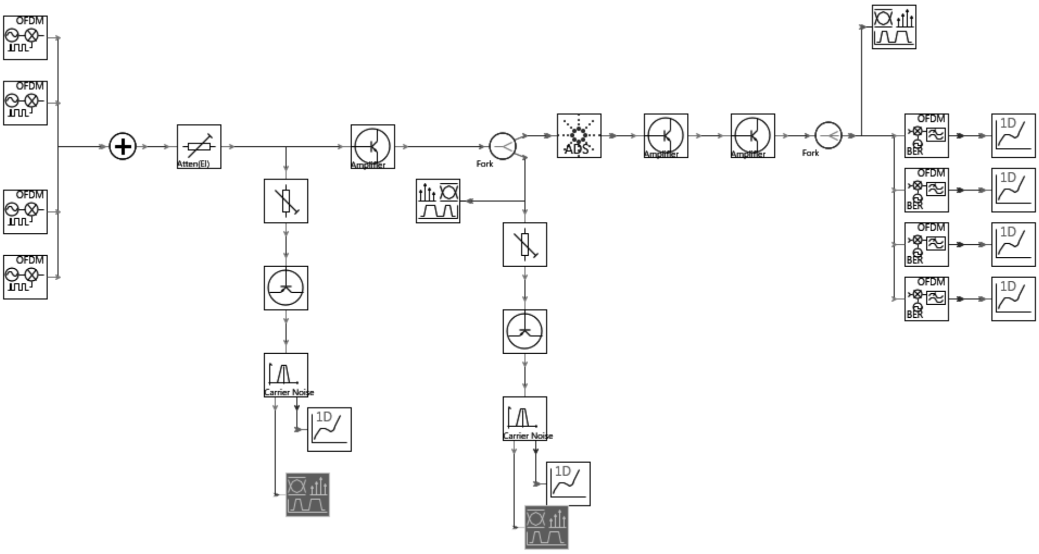

**Figure 5.5: Simulation diagram for 4-channel uplink transmission in the FUTON system.**

The simulation was carried out for various Inverse Fast Fourier Transform (IFFT) sizes (various number of OFDM subcarriers) and QAM levels of 64 and 256 while the 3-dB RF bandwidth of each channel is 100 MHz. This means that for the two QAM levels the corresponding data rate is 600 Mbit/s and 800 Mbit/s, respectively. Therefore, there are four cases as follows:

- Case I: 64QAM, IFFT size of 64, and data rate of 600 Mbit/s.
- Case II: 64QAM, IFFT size of 512, and data rate of 600 Mbit/s.
- Case III: 256QAM, IFFT size of 1024, and data rate of 800 Mbit/s.
- Case IV: 256QAM, IFFT size of 2048, and data rate of 800 Mbit/s.

The four-channel signal generated with OFDM transmitters in VPI for the Case IV is shown in Fig. 5.6. The received signal for the Case IV is shown in Fig. 5.7. It clearly shows the distortions generated by the RSOA modulator in Fig. 5.7.

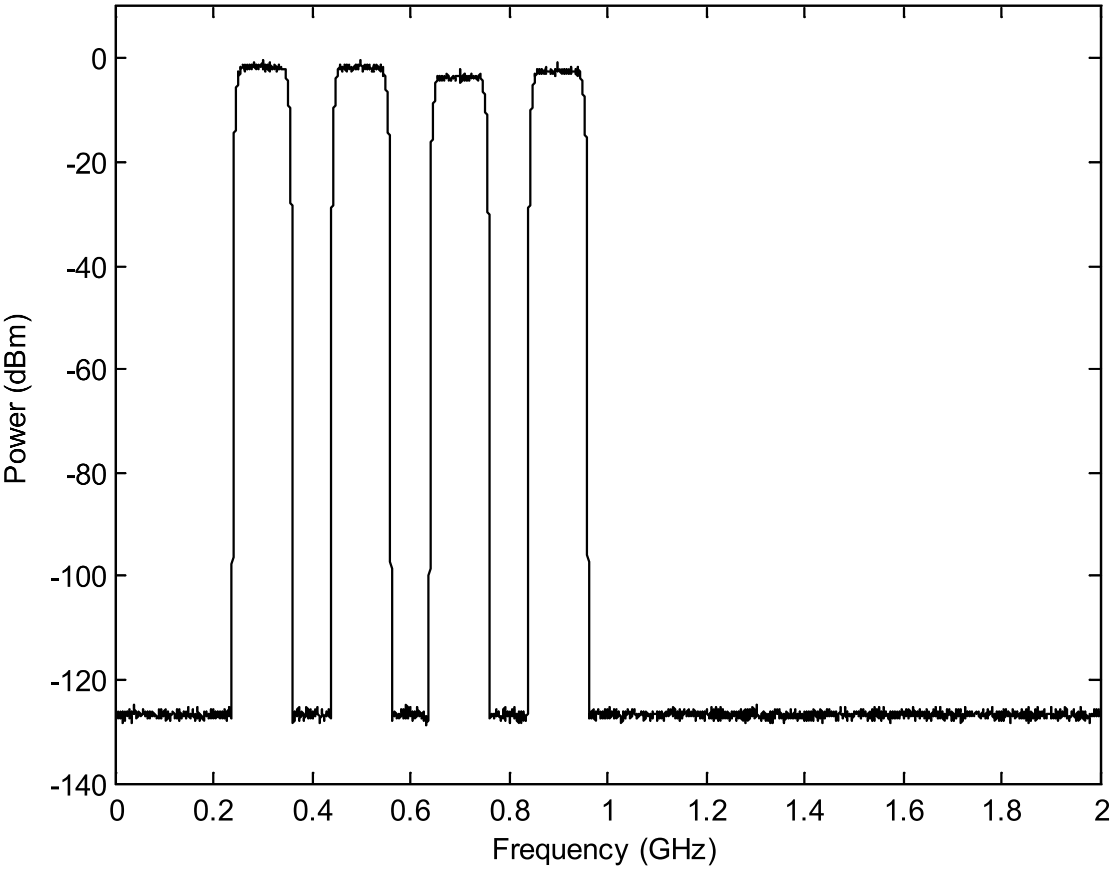

**Figure 5.6: Generated wideband SCM signal for Case IV.**

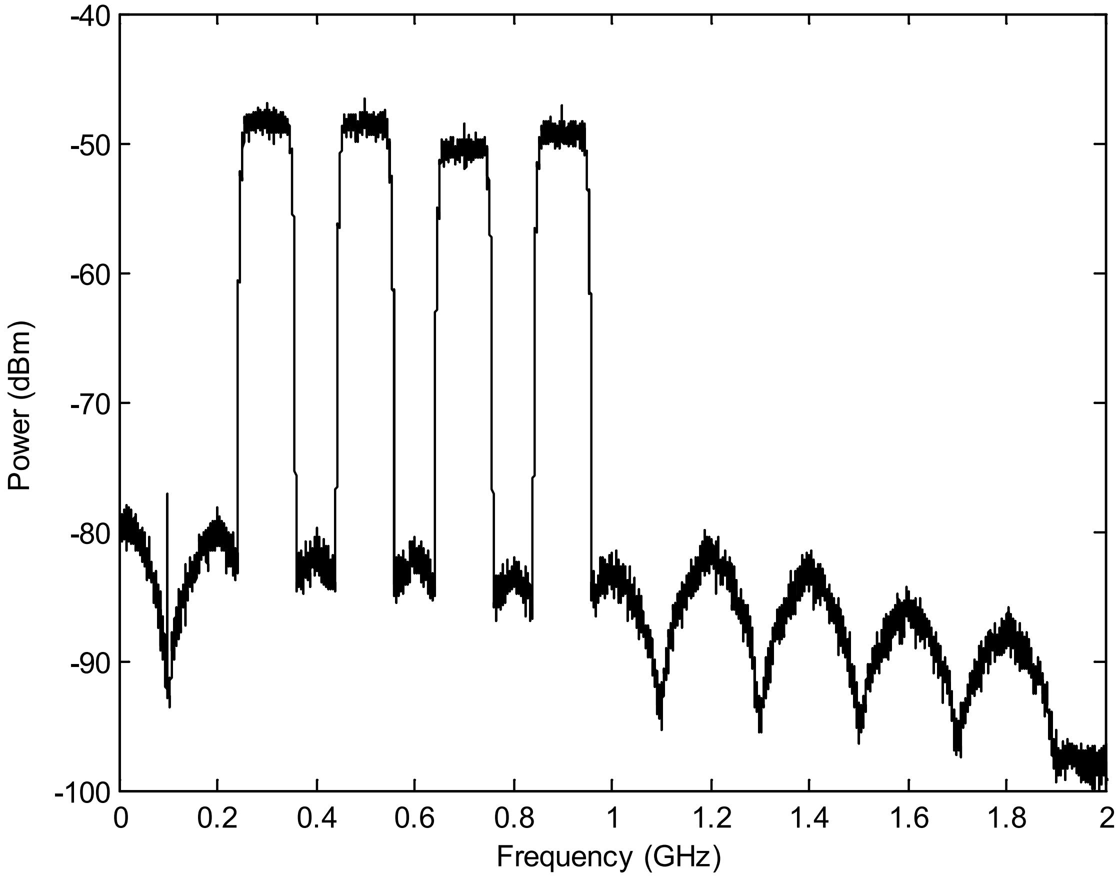

**Figure 5.7: Received wideband SCM signal for Case IV.**

From Fig. 5.8 to Fig. 5.11, the transmission performance of the FUTON system are illustrated for the four cases discussed above, respectively. To be compared, the single channel with the carrier frequency of 900 MHz was also simulated and plotted with dash lines. From these figures, we can clearly see that there are no significant differences between the four channels. The EVMs in all cases start rising more or less at the same point. Some variations are observed between different channels, but these are not consistent. These could be attributed to variations in the simulation due to the statistical nature of the signals and differences in the average powers between different channels. Differences are observed by comparing the single channel cases, especially at high RF input powers, due to the nonlinear distortions generated by the RSOA modulator. The intermodulation distortion products fall into the band of the signals as depicted previously in Fig. 4.1 in chapter 4. It is worth noting that the addition of the three more channels increase the total power of the SCM signals with 6 dB in theory. The main limitation does not come from adding more OFDM subcarriers but from increasing the number of RF carriers. For all of four cases, a large range of RF input powers is above

30 dB when the EVMs below 3% are considered. The constellations for the Case IV under RF input power of -5 dB and 4 dB are shown in Fig. 5.12. The figures also show clearly the effect of nonlinear distortions on the performance of the links.

## 5.5 Experimental Demonstration of Four Channels

Fig. 5.13 illustrates the experimental setup to study the transmission of four SCM multiplexed signals over an optical link using an RSOA as a modulator. For EVM characterization we had available a single channel VSG and a VSA. The VSG channel generated the test RF signal which complies with IEEE 802.11g standard: bit-rate 54 Mbps, 64 QAM OFDM modulations, using 52 active subcarriers. The other channels were generated from a limited bandwidth pseudo random binary sequence (PRBS) generator. A 20 Mbps PRBS baseband signal was split into three equal signals. Each signal had its bandwidth limited by a low pass filter before it was up-converted to the appropriate subcarrier frequency. Bandpass filters selected the desired frequency and removed the unwanted frequencies before the signals were combined again to form the multiplexed RF signal. The three channels and the test signal were then combined to produce the four multiplexed channel signal. The power in each channel was balanced in order to have same RF power in all the channels. An RF amplifier, ZHL-42W (37 dB gain), was used to boost the RF signal and drive the RSOA modulator.

The RF driving input power of the RSOA modulator can be adjusted by using a tunable 30 dB attenuator. Fig. 5.14 represents the four channel multiplexed signals. The signal centered at 900 MHz is the 802.11g test signal. The channel frequency that we want to characterize is set by the VSG and the LO frequencies of mixers are adjusted for the remaining carriers. Each time the test channel frequency varies the VSG output bandpass filter has also to be replaced and the mixers LO frequencies are readjusted. The interferer signals and the test signal have different characteristics but as we drive the modulator into a nonlinear region, we expect to see, the effect in the test signal, resulting from the presence of the other channels.

The measurement results are shown in Fig. 5.15. There is some variation between channels, which might be attributed to the impedance matching between the driving amplifier and RSOA and also to minor differences in bandpass filters response. When compared between the single channel and four channels, Fig. 5.15 shows similar results with simulations in section 5.4, even though the SCM signals are with different bandwidths between measurement and simulation.

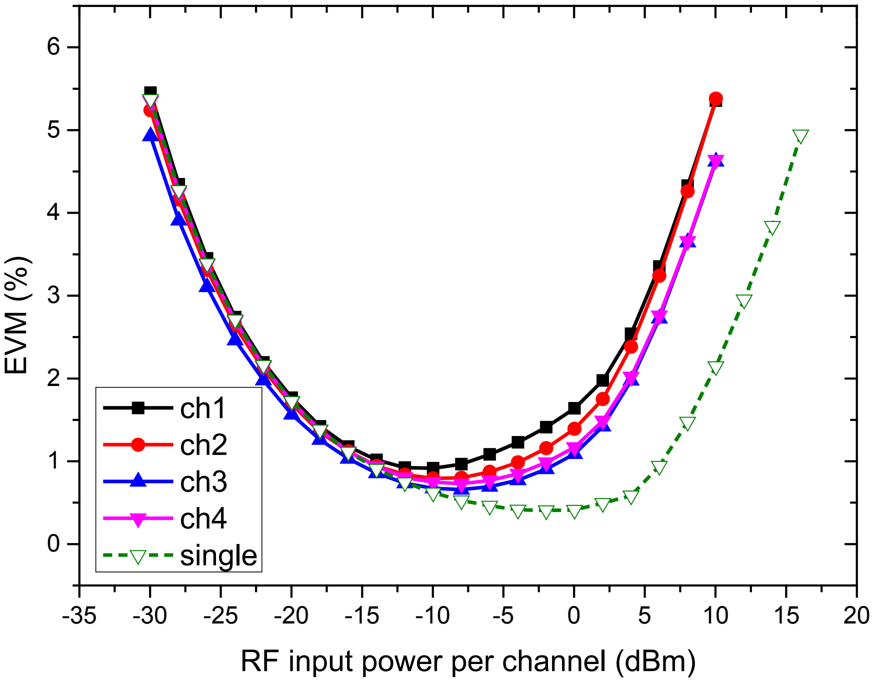

Figure 5.8: Simulation results for IFFT size of 64 and 64QAM. single channel at 900 MHz.

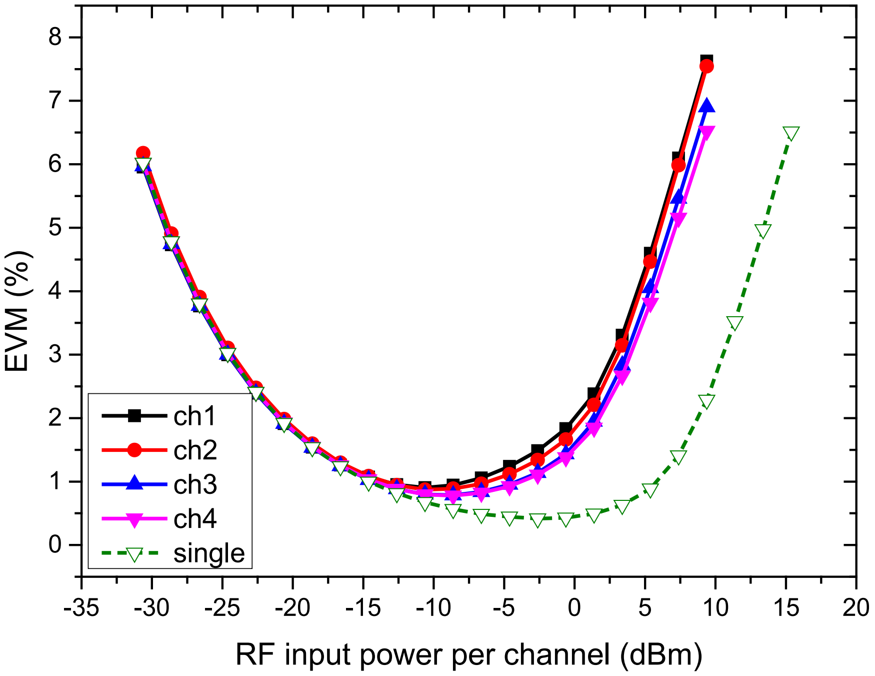

Figure 5.9: Simulation results for IFFT size of 512 and 64QAM. single channel at 900 MHz.

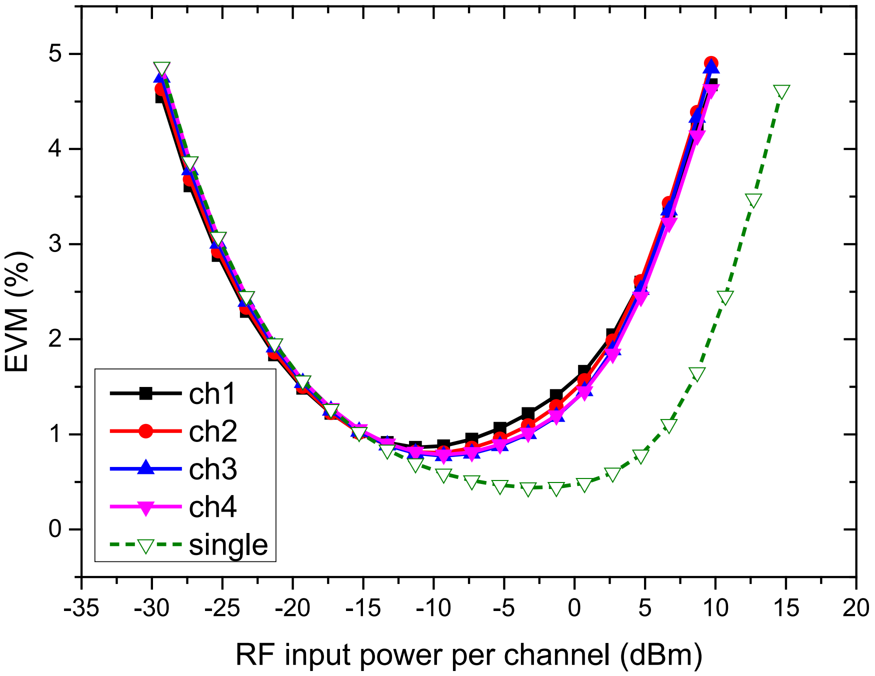

Figure 5.10: Simulation results for IFFT size of 1024 and 256QAM. single channel at 900 MHz.

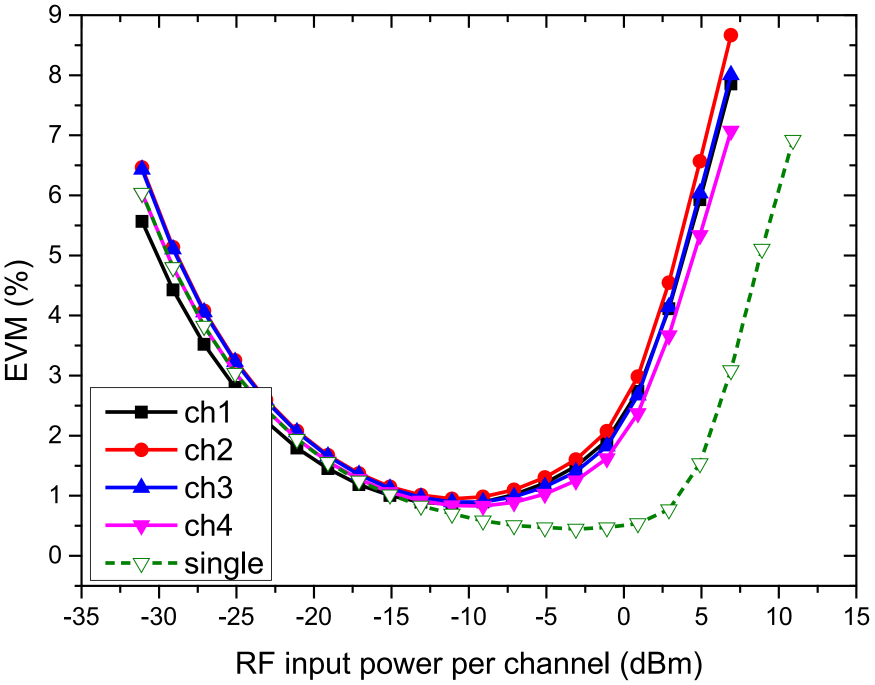

Figure 5.11: Simulation results for IFFT size of 2048 and 256QAM. single channel at 900 MHz.

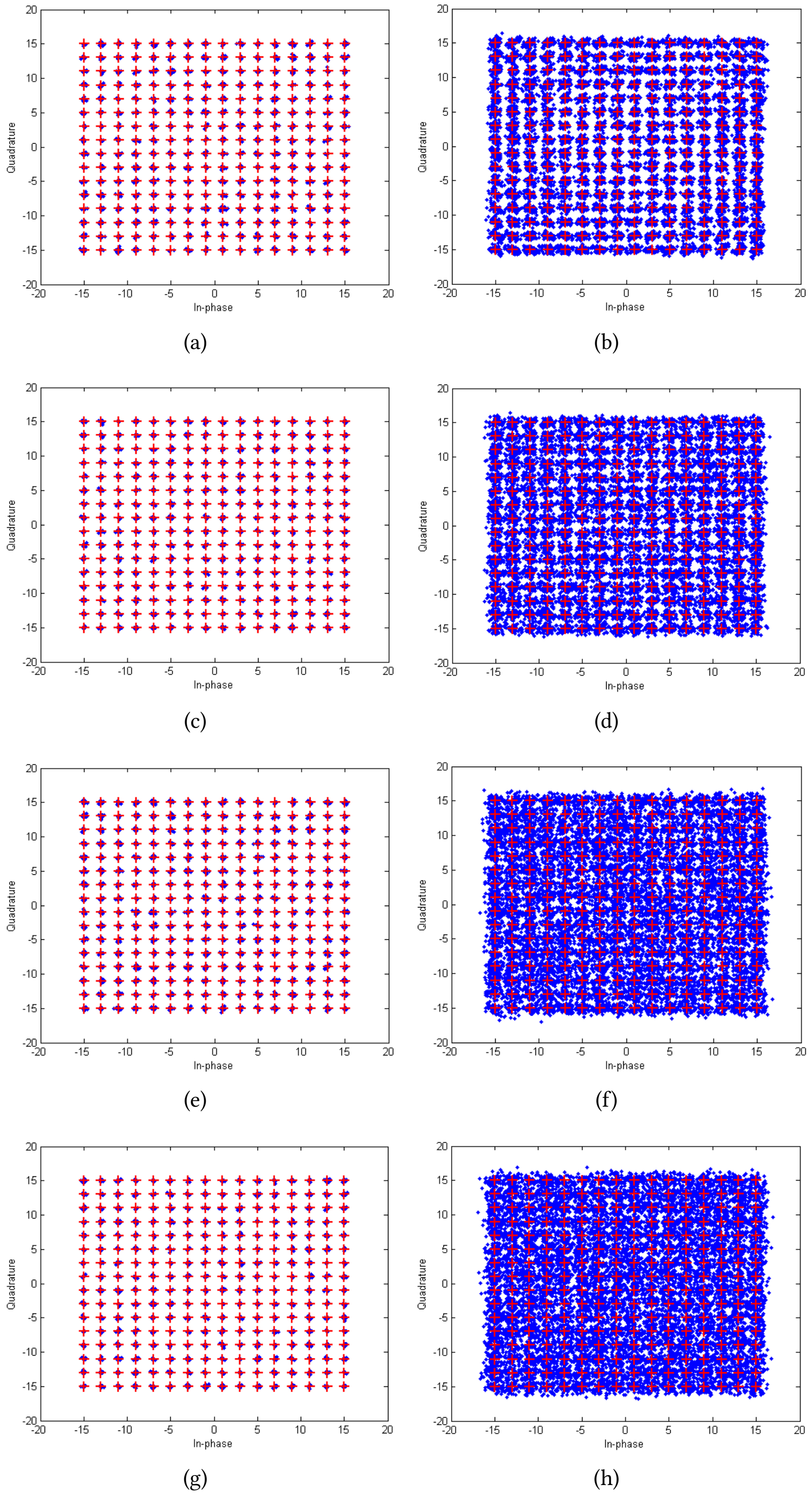

(a) (b)

(c) (d)

(e) (f)

(g) (h)

**Figure 5.12: Constellations of the SCM signal for Case IV at RF input powers of -5 dBm (right) and 4 dBm (left). (a) and (b): channel 1; (c) and (d): channel 2; (e) and (f): channel 3; (g) and (h): channel 4.**

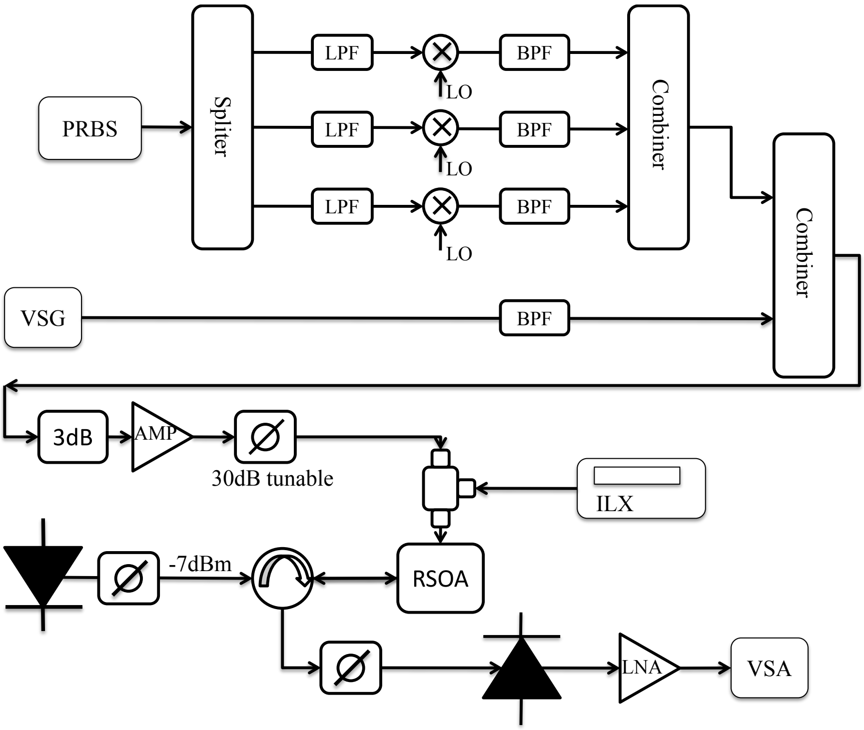

Figure 5.13: Measurement setup.

## 5.6 Summary

Based on the developed model, the performance of the FUTON system was predicted with different modulation schemes and IFFT sizes, and the system was proven to be feasible with the RSOA modulator based RoF link configure.

Comparison between single channel and four-channel cases, the performance of the FUTON system is significantly degraded due to the intermodulation distortions of the RSOA modulator. The limit of the performance comes mainly from the increase in the number of RF carriers which result in the intermodulation products due to the nonlinearity of the RSOA modulator.

Measurement of four-channel signals demonstrated the system performance even though the generated SCM signals have different signal bandwidth when compared to FUTON system.

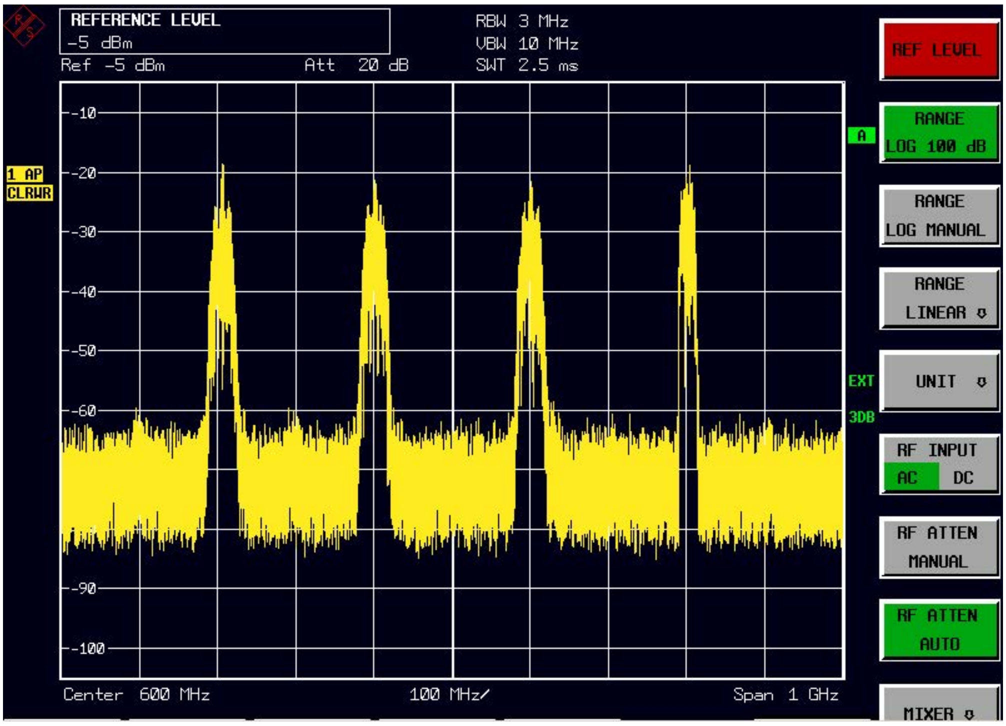

Figure 5.14: Spectrum of the SCM.

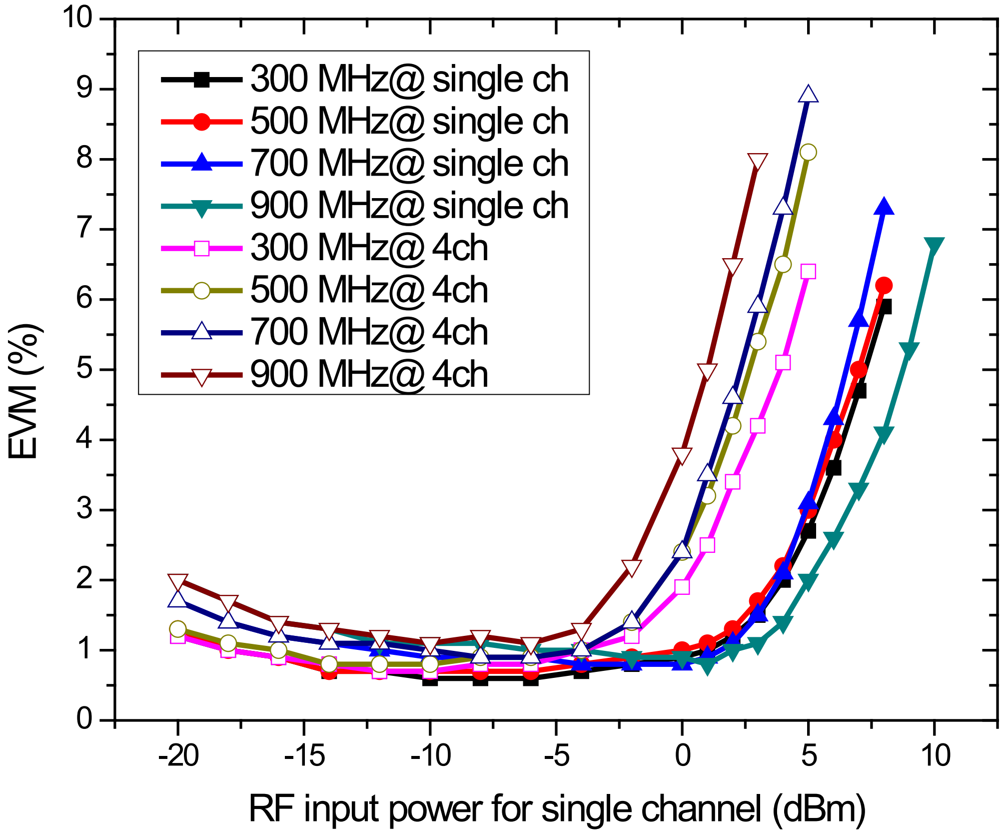

Figure 5.15: Measured EVM for single channel and four-channel signals versus RF input power.

# Chapter 6

# Conclusions & Future Work

## 6.1 Conclusions

In this thesis the modeling and characterization of RSOA modulators in RoF links have been investigated. A simple physical model, which is able to predict the performance of the RSOA and aid to design the device, has been developed under some assumptions. The multi-section model has been implemented successfully with the SDD component in ADS software. With the physical model, we investigated static and dynamic characteristics of the RSOA modulator in the RoF links. all fitting between measurement and model are matched well. It means that the simplification with the assumptions does not degrade the performance of the model for RoF applications.

The distributions of the carrier and photon densities along the active region were depicted, which give insight into the interaction between carriers and photons. Based on the simulation result, the two-electrode configures of the RSOA offer a solution to enhance the link gain. Based on the physical model, the wideband performance of FUTON system was predicted. The VPI software provides a powerful OFDM source which can generate the OFDM signal with the desired bandwidth under different modulation schemes and IFFT sizes. when compared to the single channel, the performance of the four-channel systems does not degrade at low input powers since the noise is dominant. However, the performance of the systems dramatically deteriorates at high input powers due to the intermodulation distortion of the RSOA modulator. The simulation results of the four-channel system show that there is no significant different between channels.

The advantage of the behavioral modeling is no requirement of the knowledge of the device. Several behavioral models such as TDMLP, GMP and X-paramters were addressed and compared in this thesis. They offer a system level simulation platform. Based on the TDMLP and GMP, the dynamic distortion and memory effects of the RSOA modulator were depicted by the AM-AM and the AM-PM conversion characteristics. From the results, we can see that the RSOA modulator does not show strong memory effects. The use of X-parameters enables us to analyze the nonlinearity of the RSOA modulator under the large signal excitation.

The compensation technique for nonlinear distortions of the RSOA modulator has been investigated. The popular and simple predistortion technique based on the memory polynomial model was addressed. With the method, the improvement of the linearity of the RSOA modulator has been experimentally demonstrated in this thesis. The third order intermodulation distortion of the RSOA modulator was reduced up to 17 dB with the DPD method. Therefore, the dynamic range of the RSOA modulator could benefit from the predistortion compensation.

## 6.2 Future Work

Many challenging tasks for future research are still ahead and need to be addressed. There are several research topics that can be extended from this thesis.

As the simulation shows, a new device with a two-electrode configure can be designed in order to improve the link gain of the RSOA with proper biases.

It is interesting to extend the TDMLP and GMP models for multi-channel systems. The dynamic distortion and memory effects of multi-channel systems can be predicted in system level.

The digital predistortion compensation technique presented in this thesis was demonstrated that it is capable of improving the linearity of the RSOA modulator. To make it useful in real applications, an implementation with Field Programmable Gate Arrays (FPGA) is needed.

An enhanced wideband digital predistortion with the bandwidth of 100 MHz, which is suitable for LTE-Advanced systems, is also interesting to be developed and implemented. Compensation techniques for nonlinear distortions of the multi-channel systems are well worth a try.

# References

[1] D. Wake, A. Nkansah, N. J. Gomes, G. de Valicourt, R. Brenot, M. Violas, Z. Liu, F. Ferreira, and S. Pato. A comparison of radio over fiber link types for the support of wideband radio channels. *J. Lightw. Technol.*, 28(16):2416–2422, August 2010.

[2] J. Verspecht and D. E. Root. Polyharmonic distortion modeling. *IEEE Microw. Magazine*, 7(3):44–57, June 2006.

[3] D. E. Root, J. Verspecht, D. Sharrit, J. Wood, and A. Cognata. Broad-band poly-harmonic distortion (PHD) behavioral models from fast automated simulations and large-signal vectorial network measurements. *IEEE Trans. Microw. Theory Tech.*, 53(11):3656–3664, 2005.

[4] European project ICT-FP7-FUTON. `http://www.ict-futon.eu/`.

[5] J. Capmany and D. Novak. Microwave photonics combines two worlds. *Nature Photon.*, 1(6):319–330, June 2007.

[6] A. J. Seeds. Microwave photonics. *IEEE Trans. Microw. Theory Tech.*, 50(3):877–887, March 2002.

[7] N. J. Gomes, M. Morant, A. Alphones, B. Cabon, J. E. Mitchell, C. Lethien, M. Csörnyei, A. Stöhr, and S. Iezekiel. Radio-over-fiber transport for the support of wireless broadband services [Invited]. *J. Optical Networking*, 8(2):156, January 2009.

[8] J. Li, T. Ning, L. Pei, and C. Qi. Millimeter-wave radio-over-fiber system based on two-step heterodyne technique. *Opt. Lett.*, 34(20):3136–3138, October 2009.

[9] J. James, P. Shen, A. Nkansah, X. Liang, and N. J. Gomes. Nonlinearity and noise effects in multi-level signal millimeter-wave over fiber transmission using single and dual wavelength modulation. *IEEE Trans. Microw. Theory Tech.*, 58(11):3189–3198, November 2010.

[10] W. E. Stephens, T. R. Joseph, and B. U. Chen. Analog microwave fiber optic communications links. In *MTT-S International Microwave Symposium Digest*, volume 84, pages 533–534, San Francisco, CA, USA, 1984. MTT005.

[11] C. Cox, E. Ackerman, R. Helkey, and G. E. Betts. Techniques and performance of intensity-modulation direct-detection analog optical links. *IEEE Trans. Microw. Theory Tech.*, 45(8):1375–1383, 1997.

[12] A. A. M. Saleh, A. Rustako, and R. Roman. Distributed antennas for indoor radio communications. *IEEE Trans. Commun.*, 35(12):1245–1251, December 1987.

[13] H. Hu, Y. Zhang, and J. Luo. *Distributed Antenna Systems: Open Architecture for Future Wireless Communications.* Auerbach Publications, 2007.

[14] J. Andrews. Distributed antenna systems with randomness. *IEEE Trans. Wireless Commun.*, 7(9):3636–3646, September 2008.

[15] D. Wake, P. Nkansah, A. Assimakopolous, N. Gomes, M. Violas, Z. Liu, S. Pato, F. Ferreira, G. De Valicourt, R. Brenot, and F. Van Dijk. Design and performance of radio over fibre links for next generation wireless systems using distributed antennas. In *Future Network and Mobile Summit*, pages 1–9, Florence, Italy, 2010.

[16] S. Singh, A. Kumar, Y. Liu, and S. S. Khurmi. Bandwidth extension in LTE-advanced using carrier aggregation. *Int. J. Comput. Sci. Tech.*, 3(1):7–11, 2012.

[17] A. Ghosh, R. Ratasuk, B. Mondal, N. Mangalvedhe, and T. Thomas. LTE-advanced: next-generation wireless broadband technology [Invited Paper]. *IEEE Wireless Commun.*, 17(3):10–22, June 2010.

[18] G. Yuan, X. Zhang, W. Wang, and Y. Yang. Carrier aggregation for LTE-advanced mobile communication systems. *IEEE Commun. Mag.*, 48(2):88–93, February 2010.

[19] M. Sauer, A. Kobyakov, and J. George. Radio over fiber for picocellular network architectures. *J. Lightw. Technol.*, 25(11):3301–3320, November 2007.

[20] D. Wake, A. Nkansah, and N. J. Gomes. Radio over fiber link design for next generation wireless systems. *J. Lightw. Technol.*, 28(16):2456–2464, August 2010.

[21] T. Durhuus, B. Mikkelsen, C. Joergensen, S. Lykke Danielsen, and K. E. Stubkjaer. All-optical wavelength conversion by semiconductor optical amplifiers. *J. Lightw. Technol.*, 14(6):942–954, June 1996.

[22] M. Zhao, G. Morthier, and R. Baets. Analysis and optimization of intensity noise reduction in spectrum-sliced WDM systems using a saturated semiconductor optical amplifier. *IEEE Photon. Technol. Lett.*, 14(3):390–392, March 2002.

[23] M. J. Connelly. Reflective semiconductor optical amplifier pulse propagation model. *IEEE Photon. Technol. Lett.*, 24(2):95–97, January 2012.

[24] N. Nadarajah, K.L. Lee, and A. Nirmalathas. Upstream access and local area networking in passive optical Networks using self-seeded reflective semiconductor optical amplifier. *IEEE Photon. Technol. Lett.*, 19(19):1559–1561, October 2007.

[25] Y.-Y. Won, H.-C. Kwon, and S.-K. Han. 1.25-Gb/s wavelength-division multiplexed single-wavelength colorless radio-on-fiber systems using reflective semiconductor optical amplifier. *J. Lightw. Technol.*, 25(11):3472–3478, November 2007.

[26] H. Kim. 10-Gb/s operation of RSOA using a delay interferometer. *IEEE Photon. Technol. Lett.*, 22(18):1379–1381, September 2010.

[27] J. L. Wei, A. Hamié, R. P. Gidding, E. Hugues-Salas, X. Zheng, S. Mansoor, and J. M. Tang. Adaptively modulated optical OFDM modems utilizing RSOAs as intensity modulators in IMDD SMF transmission systems. *Opt. Express*, 18(8):8556–8573, April 2010.

[28] J. L. Wei, E. Hugues-Salas, R. P. Giddings, X. Q. Jin, X. Zheng, S. Mansoor, and J. M. Tang. Wavelength reused bidirectional transmission of adaptively modulated optical OFDM signals in WDM-PONs incorporating SOA and RSOA intensity modulators. *Opt. Express*, 18(10):9791–9808, April 2010.

[29] M. J. Connelly. Wideband semiconductor optical amplifier steady-state numerical model. *IEEE J. Quantum Electron.*, 37(3):439–447, March 2001.

[30] M. J. Connelly. *Semiconductor Optical Amplifiers.* Kluwer Academic, Boston, MA, 2002.

[31] M. J. Connelly. Wide-band steady-state numerical model and parameter extraction of a tensile-strained bulk semiconductor optical amplifier. *IEEE J. Quantum Electron.*, 43(1):47–56, January 2007.

[32] S. B. Kuntze, A. J. Zilkie, L. Pavel, and J. S. Aitchison. Nonlinear state–space model of semiconductor optical amplifiers with gain compression for system design and analysis. *J. Lightw. Technol.*, 26(14):2274–2281, July 2008.

[33] P. Runge, R. Elschner, and K. Petermann. Time-domain modeling of ultralong semiconductor optical amplifiers. *IEEE J. Quantum Electron.*, 46(4):484–491, April 2010.

[34] P. Runge, C.-A. Bunge, K. Petermann, M. Schlak, W. Brinker, and B. Sartorius. Widely tunable short-pulse generation with ultralong semiconductor optical amplifiers. *J. Lightw. Technol.*, 28(5):754–760, March 2010.

[35] M. L. Nielsen, D. J. Blumenthal, and J. Mork. A transfer function approach to the small-signal response of saturated semiconductor optical amplifiers. *J. Lightw. Technol.*, 18(12):2151–2157, 2000.

[36] P. Morel and A. Sharaiha. Wideband time-domain transfer matrix model equivalent circuit for short pulse propagation in semiconductor optical amplifiers. *IEEE J. Quantum Electron.*, 45(2):103–116, February 2009.

[37] M. Razaghi, V. Ahmadi, and M. J. Connelly. Comprehensive finite-difference time-dependent beam propagation model of counterpropagating picosecond pulses in a semiconductor optical amplifier. *J. Lightw. Technol.*, 27(15):3162–3174, August 2009.

[38] A. Zhu, J. C. Pedro, and T. J. Brazil. Dynamic deviation reduction-based Volterra behavioral modeling of RF power amplifiers. *IEEE Trans. Microw. Theory Tech.*, 54(12):4323–4332, December 2006.

[39] A. Zhu, P. J. Draxler, T. J. Brazil, D. F. Kimball, and P. M. Asbeck. Digital predistortion for envelope-tracking power amplifiers using decomposed piecewise Volterra series. *IEEE Trans. Microw. Theory Tech.*, 56(10):2237–2247, October 2008.

[40] H. Cao, H. M. Nemati, A.S. Tehrani, T. Eriksson, J. Grahn, and C. Fager. Linearization of efficiency-optimized dynamic load modulation transmitter architectures. *IEEE Trans. Microw. Theory Tech.*, 58(4):873–881, April 2010.

[41] H. M. Salgado and J. J. O'Reilly. Experimental validation of Volterra series nonlinear modelling for microwave subcarrier optical systems. *IEE Proc. Optoelectronics*, 143(4):209–213, 1996.

[42] N. Vijayakumar and S. N. George. Design optimization of erbium-doped fiber amplifiers using artificial neural networks. *Opt. Eng.*, 47(8):085008–1–085008–8, 2008.

[43] C. Gallep, A. Rieznik, H. Fragnito, N. Frateschi, and E. Conforti. Black-box model for the complete characterization of the spectral gain and noise in semiconductor optical amplifiers. *Opt. Express*, 14(4):1626–1631, 2006.

[44] J. I. Ababneh and O. Qasaimeh. Simple model for quantum-dot semiconductor optical amplifiers using artificial neural networks. *IEEE Trans. Electron Devices*, 53(7):1543–1550, July 2006.

[45] M. Schetzen. *The Volterra and Wiener Theories of Nonlinear Systems.* Wiley, New York, 1980.

[46] F. M. Ghannouchi and O. Hammi. Behavioral modeling and predistortion. *IEEE Microw. Magazine*, 10(7):52–64, December 2009.

[47] S. A. Maas. *Nonlinear Microwave Circuits.* IEEE Press, Piscataway, NJ, 1997.

[48] A. Zhu, J. C. Pedro, and T. R. Cunha. Pruning the Volterra series for behavioral modeling of power amplifiers using physical knowledge. *IEEE Trans. Microw. Theory Tech.*, 55(5):813–821, May 2007.

[49] H. Ku and J. S. Kenney. Behavioral modeling of nonlinear RF power amplifiers considering memory effects. *IEEE Trans. Microw. Theory Tech.*, 51(12):2495–2504, December 2003.

[50] J. Kim and K. Konstantinou. Digital predistortion of wideband signals based on power amplifier model with memory. *Electron. Lett.*, 37(23):1417–1418, 2001.

[51] L. Ding, G. T. Zhou, D. R. Morgan, Z. Ma, J. S. Kenney, J. Kim, and C. R. Giardina. A robust digital baseband predistorter constructed using memory polynomials. *IEEE Trans. Commun.*, 52(1):159–165, January 2004.

[52] R. Raich, H. Qian, and G. T. Zhou. Orthogonal polynomials for power amplifier modeling and predistorter design. *IEEE Trans. Veh. Technol.*, 53(5):1468–1479, September 2004.

[53] L. C. Vieira, N. J. Gomes, A. Nkansah, and F. van Dijk. Behavioral modeling of radio-over-fiber links using memory polynomials. In *IEEE Int. Topical Mtg. on Microwave Photonics, MWP2010*, pages 85–88, Montreal, Canada, October 2010. IEEE.

[54] C. H. Cox. *Analog Optical Links: Theory and Practice.* Cambridge University Press, Cambridge, UK, 2004.

[55] W. K. Burns. Linearized optical modulator with fifth order correction. *J. Lightw. Technol.*, 13(8):1724–1727, 1995.

[56] H. Skeie and R. V. Johnson. Linearization of electro-optic modulators by a cascade coupling of phase-modulating electrodes. In Ka K. Wong, editor, *Proc. SPIE 1583, Integrated Optical Circuits*, pages 153–164, Boston, USA, December 1991.

[57] S. K. Korotky and R. M. de Ridder. Dual parallel modulation schemes for low-distortion analog optical transmission. *IEEE J. Sel.Areas in Commun.*, 8(7):1377–1381, 1990.

[58] S.-H. Lee, J.-M. Kang, I.-H. Choi, and S.-K. Han. Linearization of DFB laser diode by external light-injected cross-gain modulation for radio-over-fiber link. *IEEE Photon. Technol. Lett.*, 18(14):1545–1547, July 2006.

[59] M.-K. Hong and S.-K. Han. All optical linearization technique of DFB-LD based on optical injection locking for RoF system. *Microw. Opt. Technol. Lett.*, 49(10):2403–2406, October 2007.

[60] F. Tabatabai and H. S. Al-Raweshidy. Feedforward linearization technique for reducing nonlinearity in semiconductor optical amplifier. *J. Lightw. Technol.*, 25(9):2667–2674, September 2007.

[61] D. R. Morgan, Z. Ma, J. Kim, M. G. Zierdt, and J. Pastalan. A generalized memory polynomial model for digital predistortion of RF power amplifiers. *IEEE Trans. Signal Process.*, 54(10):3852–3860, October 2006.

[62] A. Zhu, P. J. Draxler, J. J. Yan, T. J. Brazil, D. F. Kimball, and P. M. Asbeck. Open-loop digital predistorter for RF power amplifiers using dynamic deviation reduction-based Volterra series. *IEEE Trans. Microw. Theory Tech.*, 56(7):1524–1534, July 2008.

[63] L. Roselli, V. Borgioni, F. Zepparelli, F. Ambrosi, M. Comez, P. Faccin, and A. Casini. Analog laser predistortion for multiservice radio-over-fiber systems. *J. Lightw. Technol.*, 21(5):1211–1223, May 2003.

[64] T. Ismail, C. P. Liu, Mitchell J. E., and A. J. Seeds. Feed-forward linearised uncooled DFB laser in a multi-channel broadband wireless over fibre transmission at 5.8 GHz. In *IEEE Int. Top. Meet. Microw. Photon. (MWP2005)*, pages 114–118, Seoul, Korea, 2005.

[65] T. Ismail, C. P. Liu, J. E. Mitchell, and A. J. Seeds. High-dynamic-range wireless-over-fiber link using feedforward linearization. *J. Lightw. Technol.*, 25(11):3274–3282, November 2007.

[66] V. J. Urick, M. S. Rogge, P. F. Knapp, L. Swingen, and F. Bucholtz. Wide-band predistortion linearization for externally modulated long-haul analog fiber-optic links. *IEEE Trans. Microw. Theory Tech.*, 54(4):1458–1463, June 2006.

[67] Y. Shen, B. Hraimel, X. Zhang, G E. R. Cowan, K. Wu, and T. Liu. A novel analog broadband RF predistortion circuit to linearize electro-absorption modulators in multiband OFDM radio-over-fiber systems. *IEEE Trans. Microw. Theory Tech.*, 58(11):3327–3335, November 2010.

[68] G. Toptchiyski, S. Kindt, K. Petermann, E. Hilliger, S. Diez, and H. G. Weber. Time-domain modeling of semiconductor optical amplifiers for OTDM applications. *J. Lightw. Technol.*, 17(12):2577–2583, 1999.

[69] N. Cheng and L. G. Kazovsky. Implications of injection current and optical input power on the performance of reflective semiconductor optical amplifiers. In *Proc. SPIE 6468, Physics and Simulation of Optoelectronic Devices XV*, page 64680V, February 2007.

[70] G. P. Agrawal. *Fiber-Optic Communication Systems.* John Wiley & Sons, inc., 3rd edition, 2002.

[71] R. H. Kingston. *Optical Sources , Detectors, and Systems.* Academic Press, Inc., London, UK, 1995.

[72] R. Olshansky, C. Su, J. Manning, and W. Powazinik. Measurement of radiative and nonradiative recombination rates in InGaAsP and AlGaAs light sources. *IEEE J. Quantum Electron.*, 20(8):838–854, August 1984.

[73] H. Burkhard and S. Hansmann. Transmitters. In *Fibre Optic Communication Devices*, chapter 3, pages 71–85. Springer-Verlag, New York, 2001.

[74] J. C. Pedro and N. B. Carvalho. *Intermodulation Distortion in Microwave and Wireless Circuits.* Artech House, Norwood, 2003.

[75] O. Mahran, M. T. Al Absy, M. S. Helmy, and G. D. Roston. Carrier density and photon rates distributions of the active region of a wideband semiconductor optical amplifiers. *Trends in Applied Sciences Research*, 7(5):370–381, May 2012.

[76] R. Lennox, K. Carney, R. Maldonado-Basilio, S. Philippe, A. L. Bradley, and P. Landais. Impact of bias current distribution on the noise figure and power saturation of a multicontact semiconductor optical amplifier. *Opt. Lett.*, 36(13):2521–2523, 2011.

[77] G. de Valicourt, A. Nkansah, D. Wake, F. Poingt, R. Brenot, and N. J. Gomes. Performance comparison of single- and two-Section RSOAs in radio-over-fiber links. *IEEE Photon. Technol. Lett.*, 25(2):190–193, January 2013.

[78] D. E. Root, J. Xu, J. Horn, M. Iwamoto, and G. Simpson. Device modeling with NVNAs and X-parameters. In *Workshop INMMIC*, pages 12–15, Göteborg, Sweden, 2010. IEEE.

[79] O. Hammi. Enhanced delay alignment method for behavioral modeling of power amplifiers exhibiting memory effects. In *IEEE MELECON Conference*, pages 404–407, Yasmine Hammamet - Tunisia, 2012.

[80] Y. Cao and Q. Zhang. A new training approach for robust recurrent neural-network modeling of nonlinear circuits. *IEEE Trans. Microw. Theory Tech.*, 57(6):1539–1553, June 2009.

[81] F. Mkadem and S. Boumaiza. Physically inspired neural network model for RF power amplifier behavioral modeling and digital predistortion. *IEEE Trans. Microw. Theory Tech.*, 59(4):913–923, April 2011.

[82] K. Hornik, M. Stinchcombe, and H. White. Multilayer feedforward networks are universal approximators. *Neural Netw.*, 2(5):359–366, January 1989.

[83] E. B. Baum and D. Haussler. What size net gives valid generalization? *Neural Comput.*, 1(1):151–160, March 1989.

[84] S. Haykin. *Neural Networks: A Comprehensive Foundation.* Upper Saddle River, NJ: Prentice-Hall, 2nd edition, 1999.

[85] M. T. Hagan and M. B. Menhaj. Training feedforward networks with the Marquardt algorithm. *IEEE Trans. Neural Netw.*, 5(6):989–993, January 1994.

[86] C. Jebali, N. Boulejfen, A. Gharsallah, and F. M. Ghannouchi. Effects of signal PDF on the identification of behavioral polynomial models for multicarrier RF power amplifiers. *Analog Integr Circ Sig Process*, 73(1):217–224, March 2012.

[87] J. Horn, D. E. Root, and G. Simpson. GaN device modeling with X-parameters. In *2010 IEEE Compound Semiconductor Integrated Circuit Symposium (CSICS)*, pages 1–4, Monterey, California, USA, October 2010. IEEE.

[88] E. Udvary and T. Berceli. Improvements in the linearity of semiconductor optical amplifiers as external modulators. *IEEE Trans. Microw. Theory Tech.*, 58(11):3161–3166, November 2010.

[89] Y. Chiu, B. Jalali, S. Garner, and W. Steier. Broad-band electronic linearizer for externally modulated analog fiber-optic links. *IEEE Photon. Technol. Lett.*, 11(1):48–50, January 1999.

[90] L. Guan and A. Zhu. Low-cost FPGA implementation of Volterra series-based digital predistorter for RF power amplifiers. *IEEE Trans. Microw. Theory Tech.*, 58(4):866–872, April 2010.

[91] A. Hekkala, M. Lasanen, I. Harjula, L. C. Vieira, N. J. Gomes, A. Nkan, S. Bittner, F. Diehm, and V. Kotzsch. Analysis of and compensation for non-ideal RoF links in DAS. *IEEE Wireless Commun.*, 17(3):52–59, June 2010.

[92] A. Hekkala, M. Hiivala, M. Lasanen, J. Perttu, L. C. Vieira, N. J. Gomes, and A. Nkansah. Predistortion of radio over fiber links: algorithms, implementation, and measurements. *IEEE Trans. Circuits Syst. I, Reg. Papers*, 59(3):664–672, March 2012.

[93] X. N. Fernando and A. B. Sesay. Adaptive asymmetric linearization of radio over fiber links for wireless access. *IEEE Trans. Veh. Technol.*, 51(6):1576–1586, November 2002.

[94] E. Abd-Elrady, L. Gan, and G. Kubin. Direct and indirect learning methods for adaptive predistortion of IIR Hammerstein systems. *e & i Elektrotechnik und Informationstechnik*, 125(4):126–131, April 2008.

*This page is intentionally left blank.*